CERN-THESIS-2005-099

Low-mass dielectron production in Pb-Au collisions at 158 A GeV using the upgraded CERES spectrometer

Alexander Cherlin

Department of particle physics,
Weizmann Institute of Science.
Rehovot, Israel.

December 2005

Low-mass dielectron production in Pb-Au collisions at 158 A GeV using the upgraded CERES spectrometer

Alexander Cherlin

Supervisor: Prof. Itzhak Tserruya

Department of particle physics,
Weizmann Institute of Science.
Rehovot, Israel.

Thesis presented to the Feinberg Graduate School
of the Weizmann Institute of Science for the degree of Ph.D. in Physics

May 15, 2006

To my wonderful and patient wife and beautiful kids.

Abstract

This thesis deals with the measurements and results of inclusive e^+e^- pair production in ultra-relativistic $Pb-Au$ collisions at 158 $A\,GeV$. The measurements were performed in the framework of the CERES experiment at the CERN SPS.

The main aim for studying ultra-relativistic collisions of heavy ions is to investigate the behavior of nuclear matter under extreme conditions of density and temperature. Lattice QCD calculations predict that under conditions of sufficiently high temperature and/or baryon density the quark and gluon degrees of freedom, usually confined within hadrons, are liberated. This state of matter is called the Quark-Gluon Plasma (QGP). Another phenomenon associated with the QGP phase transition is the restoration of the spontaneously broken chiral symmetry. Lepton pairs are unique probes of the initial fireball. Since they interact only electromagnetically, they have a long mean free path and can leave the interaction region without any additional interactions carrying direct information on the medium. In addition, dileptons allow the study of the leptonic decays of the ρ, ω and ϕ mesons. The ρ meson is of particular interest, since its lifetime is very short and almost all ρ mesons decay inside the fireball. This makes the ρ meson one of the best potential signals of chiral symmetry restoration.

CERES is the only experiment specifically designed and dedicated to the measurement of low mass electron-positron pairs at the CERN SPS. CERES has carried out a systematic programme including the measurement of dilepton pairs with p, S and Pb beams on a Au target.

The essential elements of the original CERES spectrometer are two Ring Imaging Cherenkov (RICH) detectors covering the pseudorapidity region of $2.1 \leq \eta \leq 2.7$ with full azimuthal symmetry. A doublet of Silicon Drift Chambers (SiDC) is located before RICH-1 providing a very precise measurement of the event vertex position and the event multiplicity.

In the year 1998 the CERES detector was upgraded with the addition of a TPC (Time Projection Chamber) in order to achieve a better mass resolution and to improve the rejection of π^0 Dalitz and γ conversion dilepton pairs. The TPC is placed right after the mirror of RICH-2, and it is operated within a magnetic field generated by two coils with opposite currents. The radial component of the field deflects the charged particles in the φ direction, which allows us to calculate the momentum of charged particles.

This thesis deals with the upgrade and the analysis of the 2000 $Pb-Au$ data. The thesis describes a new approach which was developed for the pair analysis and background rejection for the upgraded CERES spectrometer. 17.5 million events with a 7% centrality selection were processed. 3471 ± 126 pairs for masses $m < 0.2\ GeV/c^2$ with S/B ratio of 1/1.8 and 1747 ± 258 pairs for masses $m > 0.2\ GeV/c^2$ with S/B ratio of 1/18.6 were reconstructed. For masses $m < 0.2\ GeV/c^2$, the invariant mass spectrum is in agreement with the expectation from hadron decays. For masses $m > 0.2\ GeV/c^2$, there is a clear enhancement. Most of the enhancement is observed around the mass interval of $0.3 - 0.6\ GeV/c^2$ and in the soft pair p_T region ($p_T^{ee} < 0.5\ GeV/c^2$). The enhancement factor, defined as the measured e^+e^- yield over the calculated yield from the known hadronic sources for masses $0.2 < m < 1.6\ GeV/c^2$, is $2.9 \pm 0.32(stat.) \pm 0.44(syst.) \pm 0.87(decays)$

(where the last term represents the systematic errors in the calculated yield). The data show a non-linear dependence of the enhancement as a function of centrality. The theoretical explanations of the present results are discussed. The enhancement of dilepton pairs is interpreted as direct evidence of thermal radiation dominated by the $\pi^+\pi^-$ annihilation via a modified ρ spectral function. The data favor broadening of the ρ meson shape rather than a drop of its mass.

היווצרות של זוגות אלקטרון-פוזיטרון במסות נמוכות בהתנגשויות זהב-עופרת באנרגיה של 158 A GeV/c^2

תמצית

תיזה זו עוסקת במדידה וניתוח תוצאות של היווצרות זוגות אלקטרון-פוזיטרון במסות נמוכות $m_{ee} < 1.6$ GeV/c^2 בהתנגשויות יוני זהב עם עופרת באנרגיה של 158 A GeV/c^2. העבודה בוצעה במסגרת ניסוי CERES שנערך במאיץ ה-SPS ב-CERN.

המטרה העיקרית בחקר של התנגשויות בין יונים כבדים היא חיפוש תופעות חדשות אשר צפויות להתקיים בתנאים קיצוניים של טמפרטורה וצפיפות אנרגיה. חישובים נומריים במסגרת של QCD מצביעים שבטמפרטורה וצפיפות באריונית מספיק גבוהות קווארקים וגלואונים, הכלואים בתנאים רגילים בתוך הדרונים, משתחררים. מצב זה של החומר נקרא פלסמה של קווארקים וגלואונים (QGP). תופעה נוספת הקשורה במעבר פאזה ל-QGP היא "שיקום" של הסימטריה הקיראלית. זוגות אלקטרון-פוזיטרון הינם כלי מועדף לחקר "כדור האש" הנוצר כתוצאה מהתנגשויות בין יונים כבדים. אלקטרונים ופוזיטרונים נתונים להשפעה של הכוח האלקטרו-מגנטי בלבד, לכן הם עוזבים את איזור ההתנגשות ללא אינטרקציה עם הסביבה ויכולים לספק מידע ישיר על "כדור האש" הראשוני. בנוסף, המדידה של זוגות אלקטרון-פוזיטרון מאפשרת לחקור דעיכת המזונים ρ, ω ו-ϕ. המדידה של ρ מהווה העניין הרב ביותר מכיוון שזמן החיים שלו קצר מאוד ורוב ה-ρ מזונים דועכים בתוך "כדור האש". העובדה הזאת הופכת את ה-ρ לאחד מהסימנים הטובים ביותר לשיקום הסימטריה הקיראלית.

CERES הוא ניסוי ייחודי אשר תוכנן ונבנה במיוחד למדידת זוגות אלקטרון-פוזיטרון בתחום המסות הנמוכות ב-SPS שב-CERN. CERES ביצע תוכנית שיטתית של מדידות עם אלומות של פרוטונים ויונים של גופרית ועופרת על מטרה עשויה זהב.

המרכיבים המרכזיים של הספקטרומטר CERES הם שני גלאי Ring Imaging Cherenkov (RICH) המכסים את תחום ה- pseudorapidity של $2.7 > \eta > 2.1$ עם סימטריה אזימותלית. זוג של Silicon Drift Chambers (SiDC) הממוקם לפני RICH-1 מספק מדידה מדויקת מאוד של נקודת ההתנגשות ומספר החלקיקים שנוצרים כתוצאה ממנה.

בשנת 1998 CERES שודרג ע"י תוספת של גלאי TPC (Time Projection Chamber) על מנת לשפר את הרזולוציה במסה ואת כושר הזיהוי של זוגות אלקטרון-פוזיטרון הנוצרים בדעיכות Dalitz של π^0 (Dalitz decaysπ^0) ובהפיכות של γ בחומר (γ conversions). ה-TPC מותקן מאחורי המראה של RICH-2 ומופעל עם שדה מגנטי המיוצר ע"י שני סלילים עם זרמים מנוגדים. המרכיב הרדיאלי של השדה המגנטי גורם לסטייה של חלקיקים טעונים בכיוון אזימותלי. מדידת הסטיה מאפשרת לחשב את התנע שלהם.

התיזה הזאת עוסקת בשדרוג של גלאי CERES ובעיבוד התוצאות של הניסוי שנערך בשנת 2000. התיזה מתארת שיטה חדשה לאנליזת הזוגות של לפטונים והקטנת הרקע הקומבינטורי. האנליזה מבוססת על עיבוד של 17.5 מיליונים של מאורעות. עבור מסות $m_{ee} < 0.2$ GeV/c^2 נמדדו 3471±126 זוגות עם יחס של אות לרקע (S/B ratio) 1/1.8, ועבור מסות $m_{ee} > 0.2$ GeV/c^2 נמדדו 1747±258 זוגות עם יחס של אות לרקע 1/18.6. הספקטרום במסות נמוכות $m_{ee} < 0.2$ GeV/c^2 תואם את הספקטרום המחושב ממקורות הדרוניים ידועים. עבור מסות $m_{ee} > 0.2$ GeV/c^2 ישנו עודף של זוגות לפטונים ביחס לחזוי על-פי המקורות ההדרוניים הידועים. עיקר העודף של הזוגות נמצא בתחום המסות של $m_{ee} = 0.3 – 0.6$ GeV/c^2 ובתחום של p_T של זוג של $p_T^{ee} < 0.5$ GeV/c. גורם העודף המוגדר כיחס של כמות הנמדדת של זוגות אלקטרון-פוזיטרון לכמותם החזויה בטווח המסות של $m_{ee} = 0.2 – 1.6$ GeV/c^2 הוא 0.87(decays) ± 0.44(syst.) ± 0.32(stat.) ± 2.9 (כאשר גורם השגיאה האחרון מציג את השגיאה הסיסטמטית בחישוב זוגות הלפטונים מכל המקורות הידועים). גורם העודף מראה תלות יותר חזקה מליניארית כפונקציה של מספר החלקיקים שנוצרו בהתנגשות. מספר מודלים תיאורטיים להבנת התוצאות מוצגים בתיזה. ניתן להבין את היווצרות העודפת של זוגות לפטונים כראיה ישירה של הקרינה התרמית הנובעת בעיקר מחיסול הדדי של $\pi^+\pi^-$ המתקיים דרך ρ מזון כאשר המסה שלו או רוחבו משתנים בתוך התווך של "כדור האש". התוצאות הנסיוניות מצביעות על עדיפות מסוימת של מודל המבוסס על התרחבות ה-ρ לעומת מודל המבוסס על הקטנת המסה שלו.

Acknowledgments

I want to express my sincere gratitude to all members of the Weizmann Institute Heavy-Ion Group where I was honored to spend the last 10 years of my life. First of all, my very special and cordial thanks to Prof. Itzhak Tserruya who welcomed me into the group for my diploma work and let me continue the work for the doctoral degree. His excellent professional guidance, infinite patience and permanent encouragements constantly helped me to move through these years.

My special thanks are to Prof. Zeev Fraenkel and Dr. Ilia Ravinovich for their significant help, excellent advices and many discussions. I want to express my gratitude to Alexander Milov, Boris Khachaturov and Alexandre Kozlov for very nice years of joint work and wonderful time spent together. I also wish to thank Kirill Filimonov for his important help with the study of ROOT and C++ programming.

I owe many thanks to all members of the CERES collaboration who helped me along my work in the collaboration. I want to thank especially a few people who helped me with the physics analysis and contributed in other ways: Thomas Wienold, Hejdar Agakichiev, Ana Marin, Sergey Yurevich, Prof. Peter Wurm.

Thank you all.

Contents

List of Figures

List of Tables

Chapter 1

Introduction

1.1 Overview

This thesis is devoted to the study of low-mass ($m \lesssim 1.6\ GeV/c^2$) dielectron production in $Pb-Au$ collisions at 158 $A\ GeV$ using the CERES spectrometer upgraded with a TPC (Time Projection Chamber). This chapter describes the physics background and the motivation for the experiment. Previous results of CERES are reviewed and current theoretical interpretations are discussed.

The chapters devoted to the upgrade of the CERES spectrometer and to the data analysis reflect my contribution to the CERES experiment. I took part in the construction and testing of the TPC read-out chambers (see section 2.5.1) in our clean room laboratory at the Weizmann Institute. I participated in the assembly, commissioning and test run of the TPC at the CERN SPS. During the two physics runs at the CERN SPS I upgraded and was responsible of the software managing the high voltage and temperature of the RICH detectors. I developed new features needed to cope with the specific problems of these runs, as described in section 2.4.2. I developed a new automatic RICH gain calibration procedure (section 2.4.3) which was necessary for the correct reconstruction of the RICH hit position and amplitude. In the off-line physics analysis, I developed, implemented and managed step two and three in the data analysis chain (see section 3.1) which are basically the new electron tracking strategy (section 3.3) and electron pair analysis (sections 3.4 - 3.6). The output of step two was also used by other members of the CERES collaboration who performed the independent electron analysis. The final results of the physics analysis are given in Chapter 5.

I presented preliminary results of the analysis on behalf of the CERES collaboration at the Quark Matter conference [1] which took place in January 2004. The final results will be also published in the dedicated paper.

1.2 The interest in relativistic heavy-ion collisions

Relativistic heavy-ion collisions are the only available tool to study in the laboratory the critical behavior of strongly interacting matter and the predicted phase transition to a

quark-gluon plasma (QGP). This is a topic of major interest in recent QCD research in the non-perturbative regime. Lattice QCD calculations predict that under conditions of sufficiently high temperature and/or baryon density the quark and gluon degrees of freedom, usually confined within hadrons, are liberated [2, 3]. This state of matter is called the Quark-Gluon Plasma (QGP). Another phenomenon associated with the QGP phase transition is the restoration of the spontaneously broken chiral symmetry, when the quark condensate [4]

$$< q\bar{q} >=< \bar{q_R} q_L + \bar{q_L} q_R > \simeq -240\ [MeV]^3 \tag{1.1}$$

vanishes.

The quarks within a hadron are confined by a confining potential of the form:

$$V(r) \sim \sigma \cdot r \tag{1.2}$$

where $\sigma \simeq 0.8\ GeV/fm$ is the string tension and r is the interquark distance. As σ does not decrease with distance, an infinite amount of energy would be needed to dissociate a quark bound state. In fact the string breaks into two when it is energetically favorable to create a new pair of quarks, and consequently single color charges are not directly observed. The corresponding distance r defines the "hadron bag" or the binding radius of quarks inside a hadron. On the other side, in a dense medium the color potential is screened:

$$V(r) \sim \sigma r \left[\frac{1 - e^{-\mu r}}{\mu r} \right] \tag{1.3}$$

where $1/\mu$ is the screening radius, reducing the range of the binding force between the color charges. When the screening radius becomes smaller than the binding radius, the deconfinement phase transition occurs.

The effective or constituent mass of quarks m_q^* decreases in the presence of color screening as the temperature increases. At some point m_q^* approaches the current quark mass m_q and in the limit of vanishing quark masses chiral symmetry restoration takes place. The chirally symmetric QCD Lagrangian is invariant under the exchange of left-handed and right-handed quark fields. According to the Noether theorem, this generates two conserved currents for each quark field, which can be associated, *e.g.* with the scalar and pseudo-scalar (f_0 and π) or the vector and pseudo-vector (ρ and a_1) mesons. In the regime of spontaneously broken chiral symmetry, the degeneracy between the chiral partners no longer exists and a mass splitting between the mesons appears. In the case of mesons given in the last example, the mass splitting is: $m_\pi \simeq 140\ MeV/c^2$ and $m_{f_0} \sim\ 400 - 1200\ MeV/c^2$, $m_\rho = 770\ MeV/c^2$ and $m_{a_1} = 1260\ MeV/c^2$.

The understanding of this phase transition evolved in time along with the better results achieved in the lattice calculations. The present picture of the phase transition is as follows. Both the deconfinement and chiral symmetry restoration phase transitions happen at the same (or very close) values of the critical temperature $T_c \approx 170\ MeV$, and energy density of the order of $1.0\ GeV/fm^3$. Fig. 1.1 shows a schematic phase diagram of the transition from hadronic to quark matter in terms of temperature T versus baryon chemical potential μ_B. The calculations predict the existence of a critical point. In the

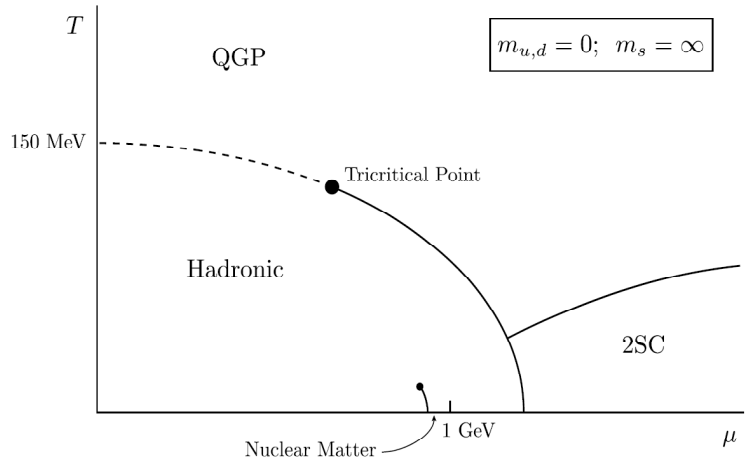

Figure 1.1: Schematic phase diagram for QGP to hadron gas phase transition for two massless flavors. "2SC" is a color-superconducting phase [5].

region to the left of this point the phase transition is of second order (phase boundary shown by the dashed line) and to the right the transition is of first order (solid line). At high baryon number density and small temperature there is a transition to a color-superconducting phase [5, 6, 7].

The implications of the study of the confinement phase transition go beyond the field of high-energy physics. In the early universe, some ten microseconds after the Big Bang, such a phase transition happened at high temperature and zero baryon density. The other extreme situation of low temperature and high baryon number density, could exist in the interior of neutron stars.

1.3 Motivation for studying dileptons

Lepton pairs were proposed as a powerful probe of the initial fireball almost 3 decades ago [8]. Since they interact only electromagnetically, they have a long mean free path compared to the size of the system. Thus, once formed they can leave the interaction region without any additional interactions carrying direct information on the medium where they were produced. The main interest is to identify the thermal radiation emitted by the system [9, 10]. Because of the strong temperature dependence of the Stephan-Boltzmann law, the largest fraction of the thermal radiation is expected to be emitted during the hottest, *i.e.* the earliest part of the collision. Thermal radiation can be emitted through $q\bar{q}$ annihilation in the QGP phase or through $\pi^+\pi^-$ annihilation in the dense hadron gas. The shapes are expected to be very different. Dileptons originating from the $\pi^+\pi^-$ annihilation have a sharp threshold at $2m_\pi$ and a broad peak around the mass of the ρ meson due to the annihilation of the $\pi^+\pi^-$ pair via a ρ meson into a lepton pair:

$$\pi^+\pi^- \rightarrow \rho \rightarrow \gamma^* \rightarrow e^+e^- \tag{1.4}$$

In contrast, the $q\bar{q}$ annihilation has an exponential shape with inverse slope parameter (or temperature) reflecting the temperature of the system.

In addition, dileptons allow the study of the light vector mesons ρ, ω and ϕ through their leptonic decays. The ρ meson is of particular interest since it is considered as the best potential signal of chiral symmetry restoration. Its lifetime is very short (1.3 fm/c) compared to the typical lifetime of the fireball of 10 fm/c, so almost all ρ mesons decay inside the fireball. Dileptons from the ρ meson decay can therefore provide information about the in-medium mass and width of the ρ meson [11], which are expected to be modified if chiral symmetry is restored. The ω and ϕ mesons have larger lifetimes of 23 and 44 fm/c respectively, most of them decay outside the fireball after regaining their vacuum properties.

1.4 Previous CERES results and their interpretation

CERES is the only experiment specifically designed and dedicated to the measurement of low mass electron-positron pairs at the CERN SPS. Di-muons have being measured at the SPS by the experiments HELIOS-3 [12], NA38/50 [13]. Very recently, a second generation experiment, NA60, has reported first results on di-muons emitted in $In-In$ collisions at 158 $A\ GeV$.

CERES has carried out a systematic programme including the measurement of dilepton pairs with p, S and Pb beams:

- $p-Be$ and $p-Au$ collisions at a beam energy of 450 $A\ GeV$ (1993);
- $S-Au$ collisions at 200 $A\ GeV$ (1992);
- $Pb-Au$ collisions at 158 $A\ GeV$ (1995, 1996, 2000);
- $Pb-Au$ collisions at 40 $A\ GeV$ (1999).

This systematic approach is essential to identify and characterize any new physics in nucleus-nucleus collisions. In this section I review the highlights of the previous CERES results and their theoretical interpretation.

1.4.1 Summary of previous results

$p-Be$ and $p-Au$ collisions at 450 $A\ GeV$

The $p-Be$ measurement, which is a very good approximation to $p-p$ collisions, together with the $p-Au$ measurement provide the necessary reference information for the nucleus-nucleus case. The $p-Be$ and $p-Au$ invariant mass spectra [14] are shown in the top panel of Fig. 1.2. They are normalized to represent the pair density per charged particle rapidity density within the CERES acceptance. The basic assumption in such a normalization is that the ratios of particle production cross sections remain constant as one goes from $p-p$ collisions to $p-A$ or $A-A$ collisions. $A-A$ collisions are treated as a simple superposition of nucleon-nucleon collisions and in this scenario the dilepton production is expected to scale with the event multiplicity.

The solid black line in the plots represents the sum of e^+e^- pairs originating from the known sources of the Dalitz decays: $\pi^0, \eta, \eta' \rightarrow e^+e^-\gamma$, $\omega \rightarrow e^+e^-\pi^0$ and the res-

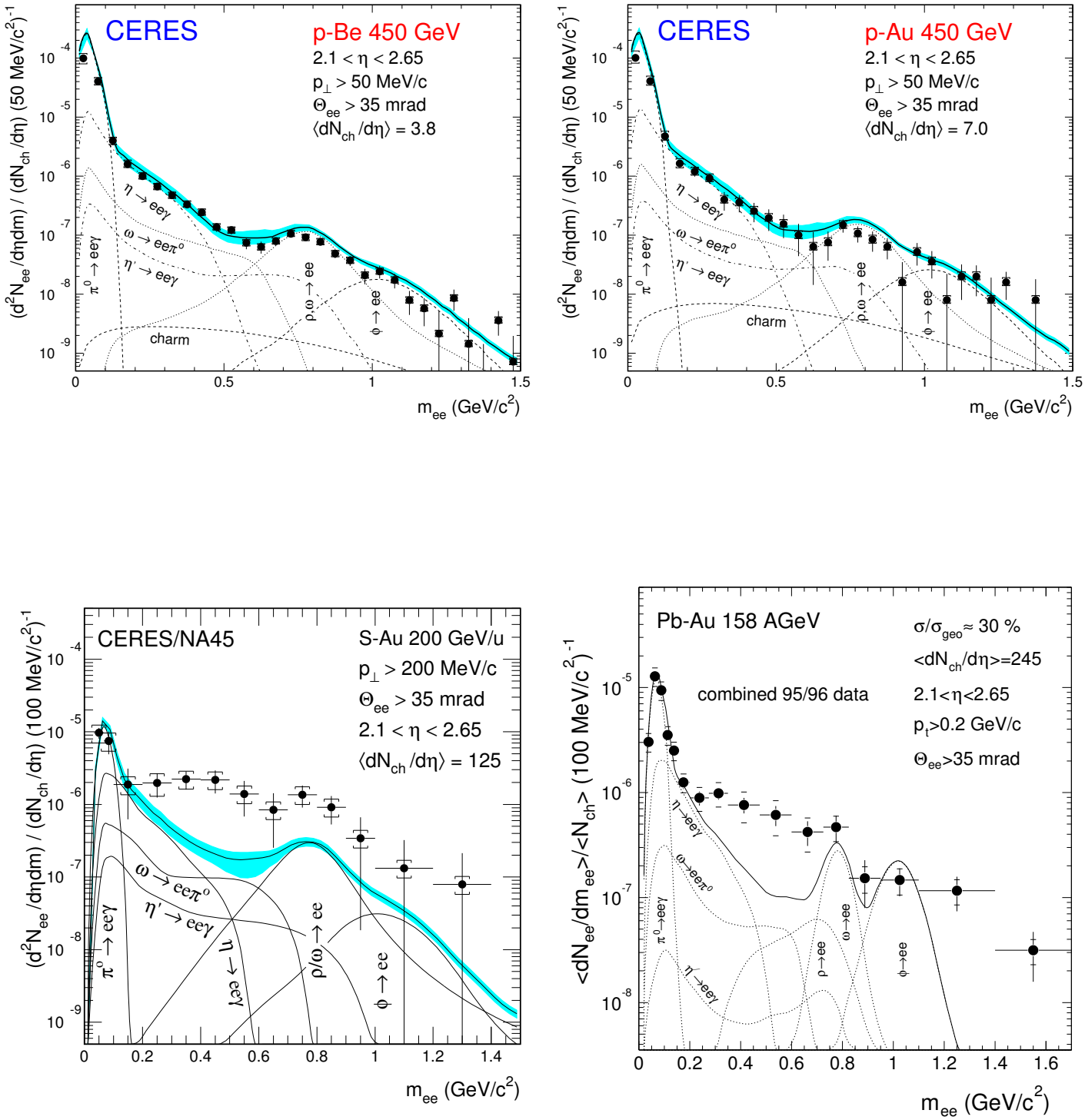

Figure 1.2: Inclusive invariant mass spectra of e^+e^- pairs in 450 *A GeV* collisions of $p-Be$ (top left) and $p-Au$ (top right), 200 *A GeV* $S-Au$ collisions (bottom left) and 158 *A GeV* $Pb-Au$ collisions (bottom right). Systematic errors are represented by brackets and statistical errors are represented by vertical bars plotted independently. The horizontal bars represent the bin size. The total yield expected from the known hadron decays is shown by the solid line taking into account the experimental mass resolution in each measurement, with $\pm 1\sigma$ uncertainty represented by the shadowed band. The individual contributions are also shown.

onance decays of $\omega, \rho, \phi \rightarrow e^+e^-$. The cocktail is calculated with an event generator based on available data (the event generator is discussed in Chapter 4). The individual contributions are also shown in the figure. The lowest mass region $m < 0.2\ GeV/c^2$ is dominated by the π^0 Dalitz decay with a distinct peak. In the intermediate region of $0.2 < m < 0.6\ GeV/c^2$ the strongest contribution is from the η Dalitz decay, and the highest mass region of $m > 0.6\ GeV/c^2$ contains mostly the contributions from the resonance decays. The shaded region represents the $\pm 1\sigma$ uncertainty as a result of experimental uncertainties in the branching ratios, form factors and cross sections used in the generator. The data points are shown together with vertical bars representing the statistical errors, whereas the brackets correspond to the systematic errors plotted independently. There is a very good agreement between the data and the hadronic cocktail, the dilepton production in $p-A$ scales with the event multiplicity and no unconventional source needs to be invoked in order to explain both spectra.

$S - Au$ collisions at 200 $A\ GeV$

The situation is quite different in $A - A$ collisions. In the bottom left panel of Fig. 1.2 the invariant mass spectrum measured in $S - Au$ at 200 $A\ GeV$ interactions [15] is shown. The π^0 Dalitz peak is well reproduced, however at higher masses there is a strong enhancement of electron pair production over the expectations from the hadronic cocktail. The enhancement factor (defined as the ratio of the measured over the calculated yield from the hadronic cocktail, integrated over the mass range $m = 0.2 - 1.5\ GeV/c^2$) is $5.0 \pm 0.7(stat.) \pm 2.0(syst.)$. The spectral shape also seems to be quite different from those of the conventional sources. The enhancement starts around twice the π mass and is most pronounced in the mass range $m = 200 - 600\ MeV/c^2$.

$Pb - Au$ collisions at 158 $A\ GeV$

A similar situation was observed in the measurements with $Pb-Au$ collisions in years 1995 [16] and 1996 [17]. The invariant mass spectrum obtained from the combined analysis of the 1995 and 1996 data [18] is shown in the bottom right panel of Fig. 1.2. The enhancement factor in the region $m > 200\ MeV/c^2$ is $2.4 \pm 0.2(stat.) \pm 0.6(syst.)$ consistent with the $S - Au$ result within errors. The spectral shape is also very similar.

The multiplicity (dN_{ch}/dy) dependence of the yield is an important tool for characterizing the source of dilepton emission. Fig. 1.3 shows the enhancement factor F versus multiplicity in 3 mass regions, obtained in the combined 1995/96 analysis of the $Pb - Au$ data. The horizontal solid line at 1 shows the expectation in the case of linear dN_{ch}/dy scaling of the enhancement factor. In the mass region $m < 0.2\ GeV/c^2$, dominated by Dalitz decays, F follows the horizontal line within errors. In contrast, the enhancement factor F in the higher mass region shows a very distinct non-linear dependence on dN_{ch}/dy. The functional form of the rise can be approximated by a linear function, suggesting a quadratic increase of the electronic yield with dN_{ch}/dy.

Fig. 1.4 shows the pair p_T spectra in three invariant mass regions. The generator curves shown are folded with the momentum resolution and normalized in the same way as the mass spectra. For masses below 200 MeV/c^2 (left panel) the p_T spectrum agrees well

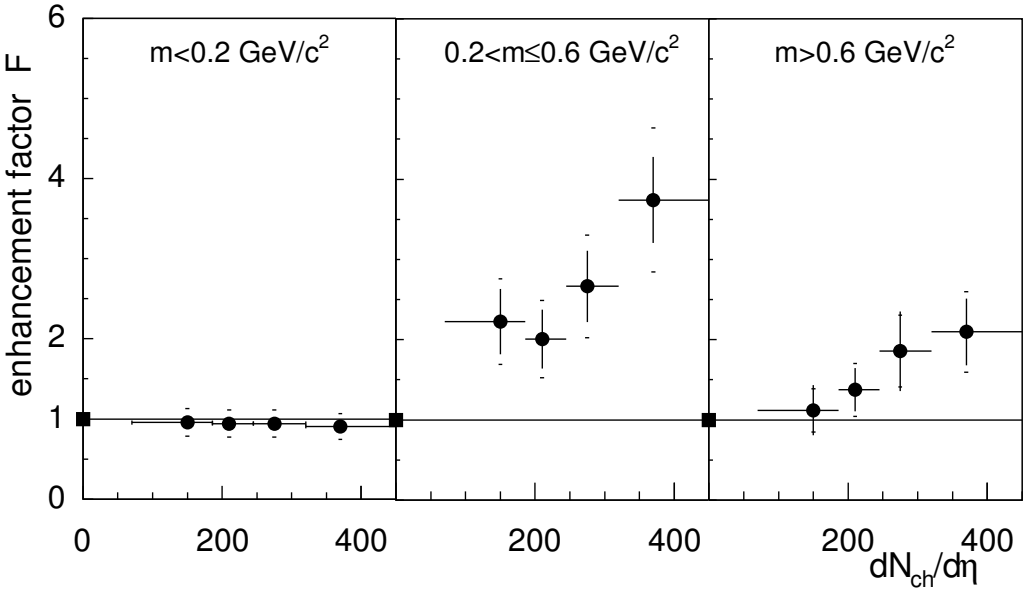

Figure 1.3: Multiplicity dependence of the e^+e^- pair enhancement factor (see text) as a function of charged particle density measured by CERES in the combined 1995/96 data analysis of $Pb-Au$ collisions at 158 $A\,GeV$.

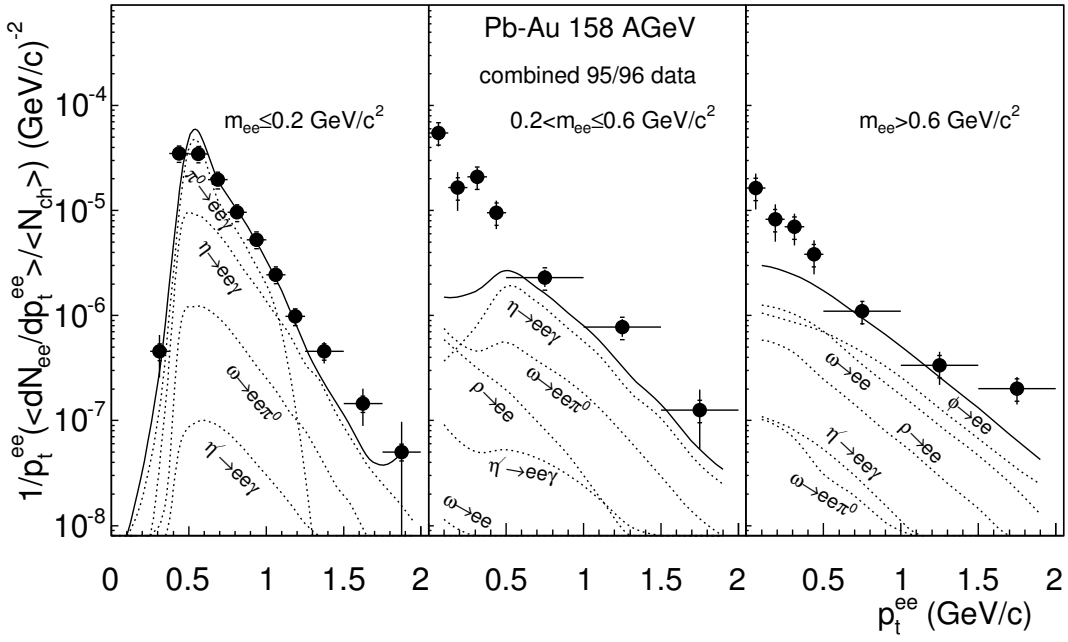

Figure 1.4: Invariant pair p_T spectra in three mass bins obtained in the combined analysis of the 1995/96 year $Pb-Au$ data The thin solid lines show the expectations from the hadron cocktail, the individual contributions are also shown.

with the prediction from the hadron cocktail, while for higher masses, the enhancement is visible over the entire p_T range but it is significantly more pronounced at low pair p_T values.

Pb − Au **collisions at** 40 *A GeV*

A strong enhancement of low-mass e^+e^- pairs has also been observed in $Pb-Au$ collisions at 40 $A\,GeV$ [19]. The motivation for this low-energy run in 1999 was to explore the effect of lower temperature and higher baryon density on the dilepton emission. The baryon-to-meson ratio at midrapidity increases almost by a factor of ∼2 as one goes down from 160 $A\,GeV$ to 40 $A\,GeV$. As shown in the next section, the baryon density plays a key role in explaining the excess of low-mass pairs. Therefore, one expected an even stronger enhancement in the production of e^+e^- pairs at 40 $A\,GeV$. Indeed, the enhancement factor for masses $m > 0.2\ GeV/c^2$, $F = 5.61 \pm 1.4(stat.) \pm 1.1(syst.)$, observed in this run is about 2 times higher than the one measured at the full SPS energy of 160 $A\,GeV$.

1.4.2 Theoretical interpretations

The CERES results have triggered considerable interest and theoretical activity in particular because of their possible link to chiral symmetry restoration [20]. The enhancement can not be reproduced with a modified cocktail of conventional dilepton sources since the particle production ratios are constrained by measurements from other experiments.

The explanation of the low-mass excess requires therefore an additional source, not present in the $p-p$ case. Most of the theoretical interpretations include the $\pi^+\pi^-$ annihilation channel, since pions are abundantly produced in heavy ion collisions. According to the Vector Meson Dominance model (VDM) [21, 22], photon-hadron interactions proceed through the photon turning into one of the vector mesons with the same quantum numbers as photons, namely $J^{PC} = 1^{--}$, Q=B=S=0. The lowest mass states with such quantum numbers are the ρ, ω and ϕ. The ρ meson dominates due to its very large width. Looking at the reverse reaction, the $\pi^+\pi^-$ annihilation proceeds as shown by equation (1.4).

The vacuum ρ spectral function (or imaginary part of the ρ propagator) is shown in Fig. 1.5 by the full solid line. Adding the π annihilation channel to the hadronic cocktail accounts for a sizable fraction of the observed excess in $Pb-Au$ collisions, particularly near the ρ mass, but fails to reproduce the data in the mass region $0.2 < m_{ee} < 0.6\ GeV/c^2$, as shown in Fig. 1.6 by the green dashed line. The same holds true in the $S-Au$ case, as shown in Fig. 1.7. In order to quantitatively reproduce the data in the mass range $0.2 - 0.6\ GeV/c^2$ one has to invoke in-medium modifications of the ρ meson.

Two major scenarios of in-medium effects on the ρ spectral function have been proposed:

a) Dropping of the ρ meson mass using the Brown-Rho scaling

The first calculations in the framework of Brown-Rho scaling [29] were first performed by Li, Ko and Brown [30], and later by Cassing *et al.* [24, 25]. In this approach, the

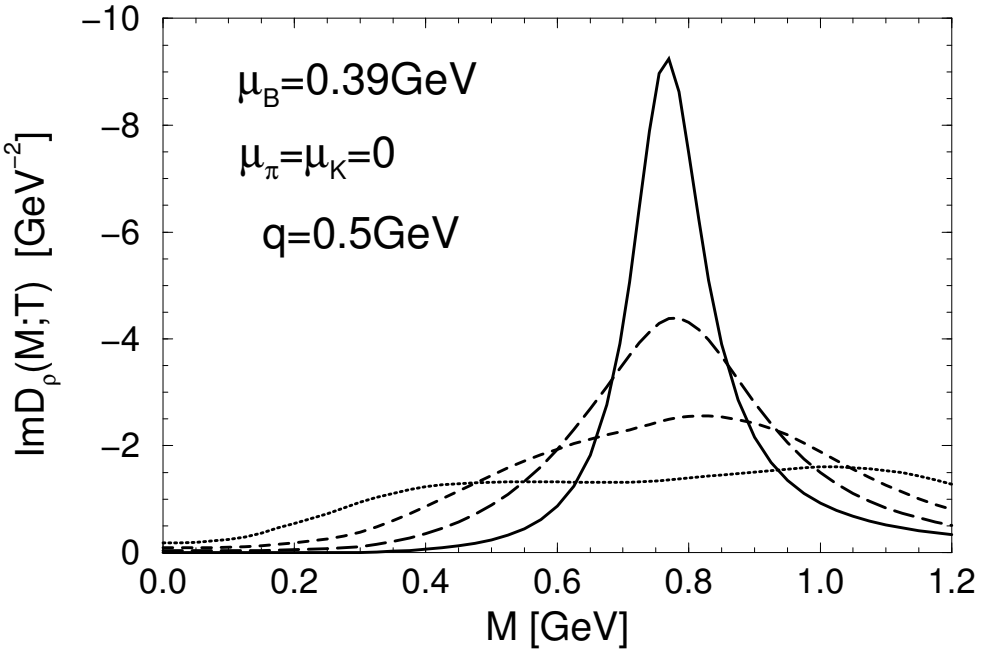

Figure 1.5: The ρ meson spectral function in a medium characterized by a baryon chemical potential $\mu_B = 0.39\ GeV$ and temperature of $T = 127\ MeV$ (long-dashed), $T = 149\ MeV$ (short-dashed), $T = 170\ MeV$ (dotted). The full line is the free spectral function [23].

in-medium masses of the light vector mesons scale as the in-medium quark condensate $< q\bar{q} >$:

$$\frac{< q\bar{q} >^*}{< q\bar{q} >^0} = \frac{m^*_\rho}{m^0_\rho} = \frac{m^*_\omega}{m^0_\omega} = \frac{m^*_\phi}{m^0_\phi} \tag{1.5}$$

The values with "0" refer to normal nuclear matter density whereas the values with a "$*$" symbol refer to the in-medium quantities. The Brown-Rho scaling mechanism uses an effective quark mean-field theory in the regime of high temperature and/or density where the quarks are the relevant degrees of freedom. Lattice QCD calculations, such as [31, 33], show that at high temperature the main change in the quark condensate happens at temperatures higher than $0.9 \cdot T_c$, where T_c is the critical temperature for the chiral symmetry restoration. At SPS energies, the main change in the quark condensate is due to the high baryon density and the decrease of the ρ meson mass in the medium is approximately equal to [32]

$$\frac{m^*_\rho}{m^0_\rho} \approx 1 - 0.28 \cdot \frac{\rho^B}{\rho^B_0} \tag{1.6}$$

where m^*_ρ is the mass of the ρ meson at a baryon density ρ^B, m^0_ρ is the mass of the ρ meson in vacuum, and ρ^B_0 denotes the normal nuclear density. Calculations using the

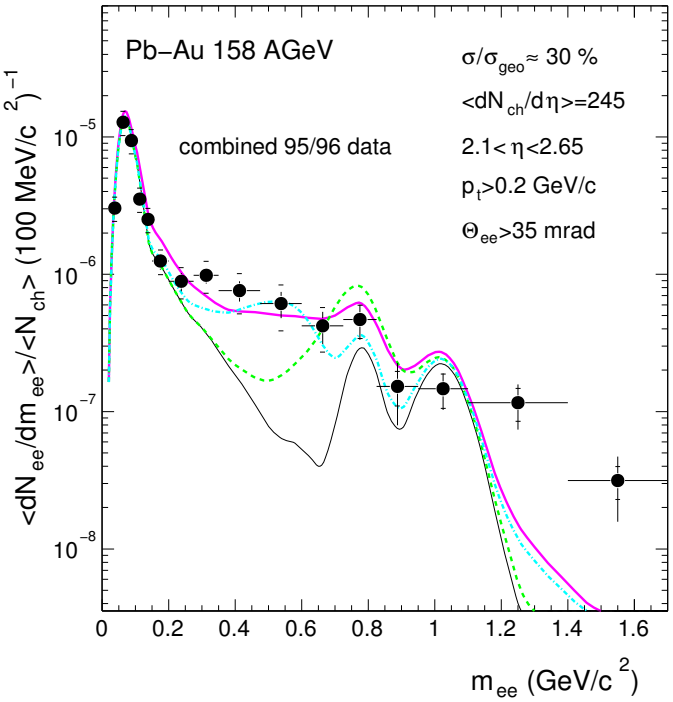

Figure 1.6: Inclusive invariant mass spectrum of 158 *A GeV* $Pb-Au$ collisions (combined 1995/96 data). The hadronic cocktail is shown by the black solid line. The green dashed line - represents the total yield including hadron decays and the contribution from $\pi^+\pi^-$ annihilation with vacuum ρ meson spectral function; the purple full line and the blue dashed-dotted line represent the same but with in-medium broadening of the ρ meson and dropping ρ mass scenarios, respectively.

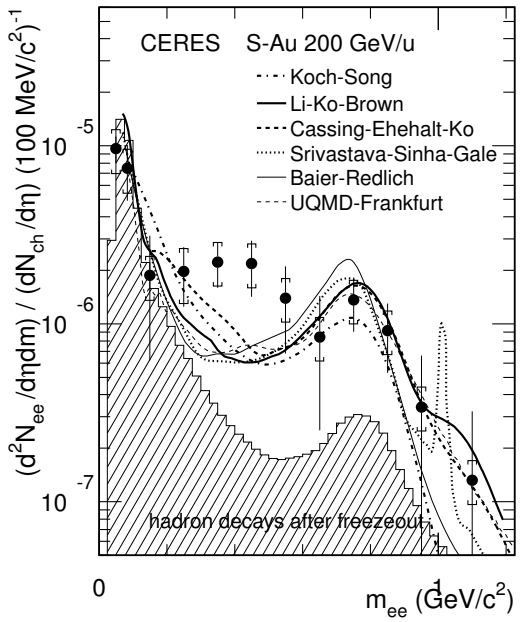

Figure 1.7: The CERES $S-Au$ results with calculations of Li, Ko and Brown [30], Cassing *et al.* [24, 25], and the models of [26, 27, 28]). All models include the pion annihilation channel using the free ρ meson spectral function.

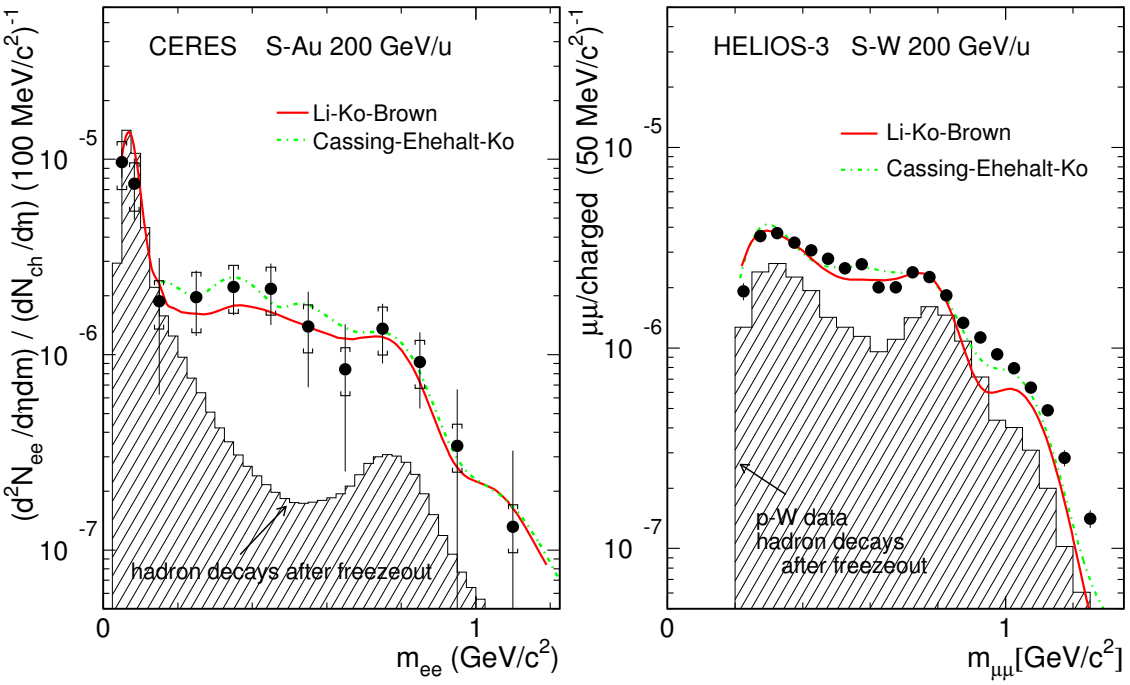

Figure 1.8: Comparison of CERES and HELIOS-3 results with the calculations [30, 24, 25] using dropping ρ mass.

dropping ρ mass are compared in Fig. 1.6 with the 1995/96 $Pb-Au$ data and in Fig. 1.8 with the S data of CERES (left panel) and HELIOS-3 (right panel).

b) Broadening of the ρ spectral shape within the dense hadronic matter

This approach was followed by Rapp and Wambach [34, 35]. The dilepton production rate is determined by the electromagnetic current-current correlator, the imaginary part of which is basically the ρ spectral function. The latter one is calculated using the in-medium self-energy Σ_ρ of the ρ. The main contributions to Σ_ρ, leading to the broadening of the ρ spectral function, are from the ρ scattering off baryons, mainly nucleons and Δ's, whereas the ρ-meson scattering ($\rho\pi$ and ρK) give a very small contribution to the broadening of the spectral function [23]. Fig. 1.5 shows the modified ρ spectral functions for a baryon chemical potential $\mu_B = 0.39\ GeV$ and different values of temperature. With such a model, one is able to reproduce both, the HELIOS-3 and the CERES low-mass dilepton enhancement measured with the S and Pb beams, as shown for example in Fig. 1.6.

To summarize, π annihilation incorporating in-medium modifications of the ρ meson is able to reproduce the observed dilepton enhancement. Both approaches, the dropping ρ-meson mass as a precursor of chiral symmetry restoration in the high baryon density, and the more conventional ρ meson broadening due to rescattering off baryons, reproduce equally well the CERES results. The precision of data did not allow to discriminate between these two scenarios. The experimental results could not provide insight into the

question whether the approach to chiral symmetry restoration proceeds broadening or dropping mass.

1.5 Run 2000 Motivation

Since CERES was the only experiment which measured low-mass e^+e^- pairs, it was of great importance to confirm the low-mass pair enhancement with a new improved measurement. The upgrade of the CERES spectrometer (which is discussed in the next chapter) with a TPC completely changed the electron tracking strategy through the CERES spectrometer. In addition to two RICH counters, the electrons are identified also by their dE/dx signal in the TPC. Another major change is the way the momenta of charged particles are determined. Before the upgrade, the momentum was calculated using the deflection in the magnetic field between the two RICH counters. In this scheme the reconstruction of electron tracks with p_T below 200 MeV/c was nearly impossible and the momentum resolution around the ω and ϕ masses was $6-7\%$. After the upgrade, the magnetic field between the RICH detectors was switched off, and the momentum is now calculated using the deflection of the charged particles in the magnetic field of the TPC. Since the TPC provides us with up to 20 spatial points per track, the momentum measurement is more precise. As a consequence, the mass resolution at the ϕ mass is improved to the level of 4%, derived from the position resolution and confirmed by the line shape of the Λ and K_s [36, 37]. Furthermore, the reconstruction of electron tracks with p_T as low as 100 MeV/c is now possible. Another benefit is the improved π^0 Dalitz decay rejection. Since their momentum spectrum is soft the reconstruction of low p_T tracks helps reducing the combinatorial background coming from unrecognized π^0 Dalitz decays.

Using these new features and improvements in the upgraded CERES spectrometer, the year 2000 run provided us with an independent measurement of e^+e^- pair production in $Pb-Au$ collisions and with quite different systematic errors in the analysis procedure. The improved measurement of the vector meson decays should allow a more precise comparison with the theoretical models.

Chapter 2

Upgraded CERES spectrometer and experimental setup

2.1 Experimental setup - overview

The layout of the CERES spectrometer used in the 2000 $Pb - Au$ run is shown in Fig. 2.1. The left side shows the essential elements of the original design, two Ring Imaging Cherenkov (RICH) detectors separated by a superconducting double solenoid, covering the pseudorapidity region of about $2.1 \leq \eta \leq 2.7$ with full azimuthal symmetry. The Cherenkov photons emitted by fast particles are reflected back by the spherical mirrors in each RICH and registered in two UV detectors located at the focal plane of the mirrors, forming a ring image. The radiators are operated at the high threshold $\gamma_{th} = 32$ of CH_4 in order to reject most of the hadrons. Since a RICH measures only the direction of the particle, the spectrometer is supplemented by additional charged-particle tracking detectors located both before and after the double RICH system.

A closely-spaced doublet of Silicon Drift Chambers (SiDC) [38] is located before RICH-1 at a distance of about 10 cm downstream of the target. With their excellent position resolution they provide us with a very precise measurement of the event vertex position and of the charged particle multiplicity $dN_{ch}/d\eta$. In addition, the SiDC detectors are used for the identification of close electron pairs originating from γ conversions and π^0 Dalitz decays.

The Time Projection Chamber (TPC) is the key element of the CERES upgrade. The TPC [39, 40] replaced the Pad Chamber used in the 1995/96 runs. It is placed right after the mirror of RICH-2, at a distance of 3.5 m downstream of the target. The track reconstruction in the magnetic field of the TPC provides the momentum and charge of the particle. The dE/dx signal in the TPC provides also additional electron identification in addition to the main identification by the RICH detectors. In this upgraded configuration, the magnetic field between the two RICH detectors is switched off.

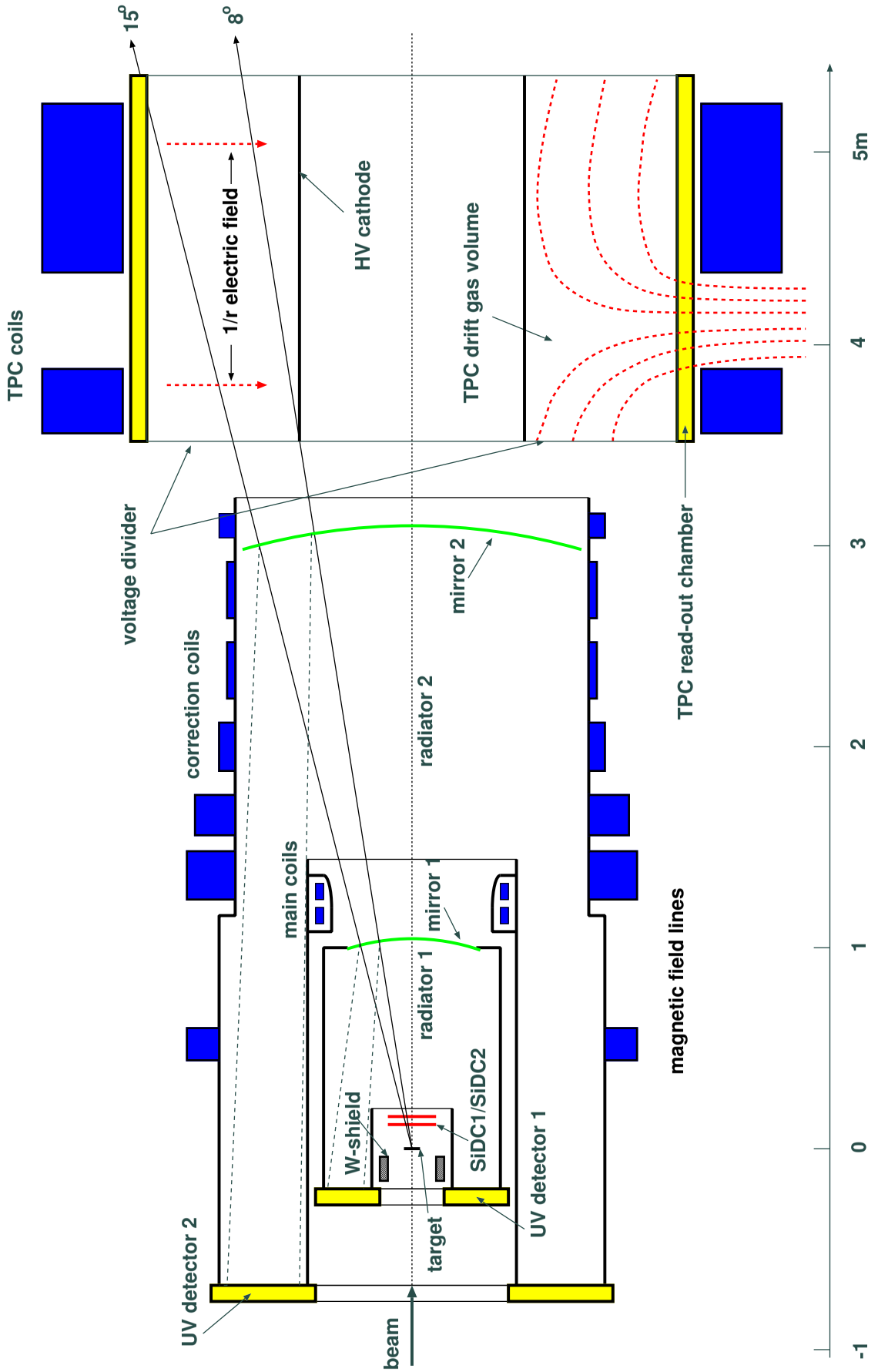

Figure 2.1: Schematic view of the upgraded CERES spectrometer.

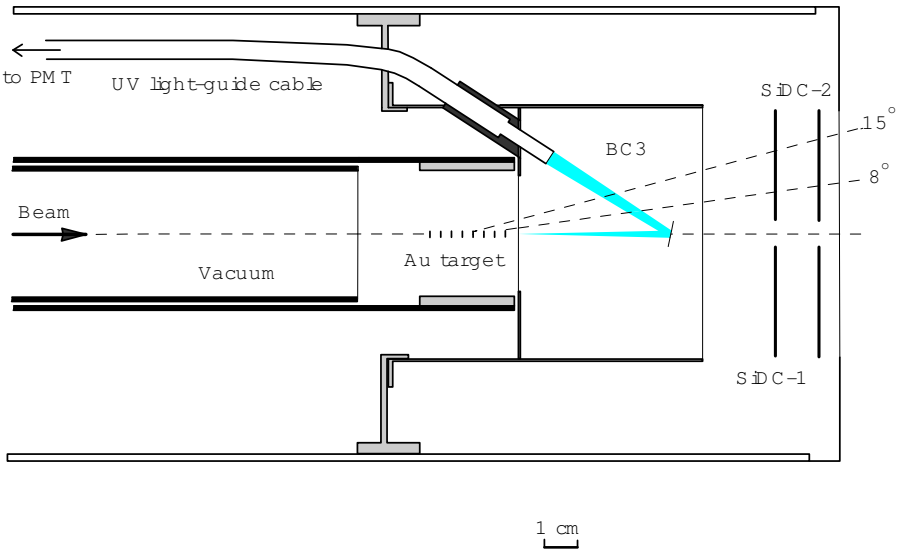

Figure 2.2: Schematic view of the target area.

2.2 Target area

A schematic view of the target region is shown in Fig. 2.2. It contains the target, the doublet of SiDC detectors and one of the Cherenkov beam counters ($BC3$), used in the interaction trigger setup (see section 2.6). The target consists of 13 Au disks of 25 μm thickness and 600 μm diameter, spaced by 2.8 mm between them. Such a structure provides a large interaction rate while minimizing the amount of gamma conversions and secondary interactions. The total target thickness is 325 μm, corresponding to an interaction length of 1.35%. The spacing between the target discs prevents from particles produced within the CERES acceptance to interact in the following discs, limiting the radiation length to half the thickness of one disk, or 0.37%. The tube containing the target region is thermally insulated in order to stabilize the drift velocity in the SiDC detectors.

2.3 SiDC detectors

The doublet of Silicon Drift Chambers (SiDC) covers the pseudo-rapidity acceptance of $1.95 < \eta < 3.21$ with full azimuthal symmetry. The chambers were constructed using the novel AZTEC design [41]. Each chamber is made of a silicon wafer and has a disc shape of $4''$ diameter and $280 \pm 20 \mu m$ thickness. A charged particle traversing the detector creates a cloud of electron-hole pairs. The electrons drift radially in the electric field towards the outer edge of the chamber where they are collected by an array of 360 anodes. The drift field is generated by voltage dividers with concentric rings implanted in the silicon wafer.

	RICH-1	**RICH-2**
η range	1.88-2.81	2.03-2.65
$\Delta\eta$	0.93	0.62
$<\eta>$	2.34	2.43
radiator length (cm)	90	175
radiator gas	CH_4	CH_4
$\gamma_{th}(measured)$	31.4	32.6
windows	CaF_2	quartz
RICH bandwidth (eV)	6.1-8.5	6.1-7.4

Table 2.1: Specifications of the RICH detectors.

The nominal value of the field is 500 V/cm resulting in a drift velocity of about 10 $\mu m/ns$. The position resolution is a function of radius. The larger the drift distance, the larger the charge diffusion, and thus the electron cloud is collected in several anodes allowing center-of-gravity determination leading to a better position resolution in the azimuthal direction. Each anode is subdivided into 5 segments, two of which are interlaced to the closest of the neighboring anodes to enforce charge sharing even when the drift distance is short. Such a sophisticated structure provides an accurate azimuthal position resolution of 2 $mrad$ for hits shared between 2 or more anode. In the case of single anode hits the position resolution depends on the anode size, which in our case lead to a position resolution of about 5 $mrad$. The radial position r (or the polar angle θ) is calculated knowing the drift velocity and measuring the drift time with the sampling frequency of 50 MHz. The position resolution in r direction is 30 μm. An example of a SiDC-1 event is given in Fig. 2.3.

2.4 RICH detectors

2.4.1 Specifications

The specifications of the two RICH detectors are summarized in Table 2.1. The spectrometer acceptance is limited by RICH-2, while RICH-1 has a larger acceptance allowing to veto the π^0 Dalitz decays where only one of the tracks is inside the fiducial acceptance.

In order to minimize the γ conversions and to reduce the multiple scattering, the mirror of RICH-1 is made of only 1.1 mm (0.41% X/X_0) thick carbon fiber. It is built in one piece held only at the outer circumference. The original design of the CERES spectrometer didn't include any detector downstream of the RICH-2 vessel, therefore the RICH-2 mirror was built of standard glass, 6 mm thick, segmented azimuthally into 10 pieces.

The radiators and the UV detectors are separated by the UV transparent windows. RICH-2 has a quartz window with a cut-off at 7.4 eV. RICH-1 window is made of CaF_2 which has a higher cut-off at 8.5 eV compensating for its shorter radiator length, keeping

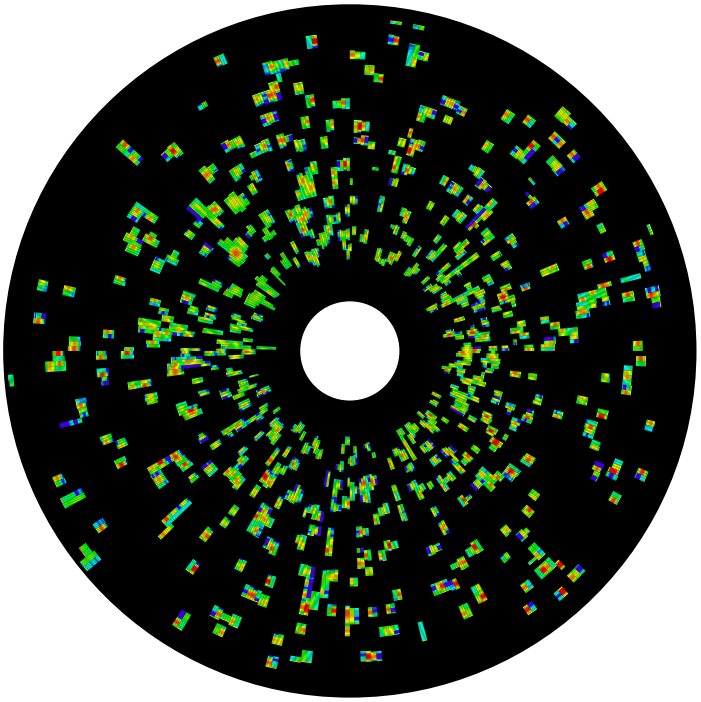

Figure 2.3: A central $Pb - Au$ event in the SiDC-1 detector. The hits are shown by clusters of colored pads. The color of a pad depends on the pad amplitude, so that the blue corresponds to the lowest amplitudes and the red to the highest amplitudes.

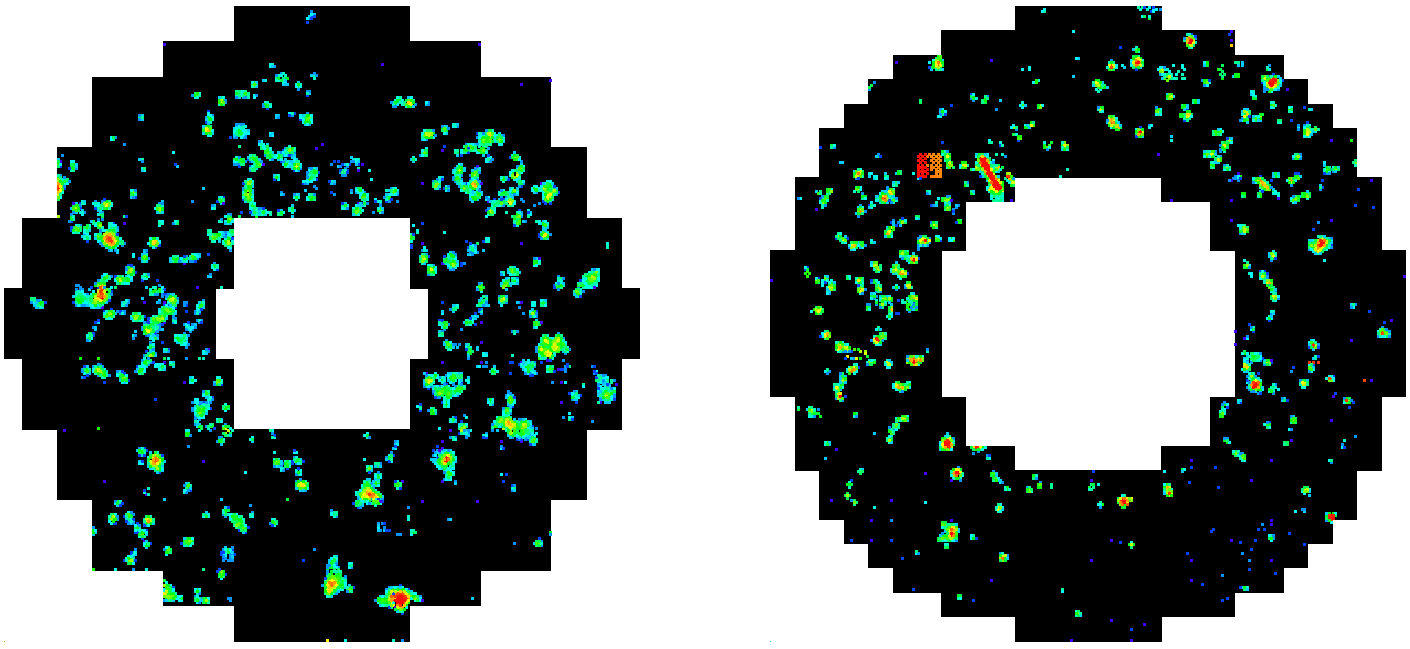

Figure 2.4: A central $Pb - Au$ event in RICH-1 (left) and RICH-2 (right). The convention about the hit drawing and pad colors is the same as for SiDC detectors.

the performance of the two RICH detectors similar in terms of photons per ring (about 10 resolved hits per ring).

An important feature of the RICH detectors is the location of the UV detectors. They are placed upstream of the target, thus they are not traversed by the intense flux of forward particles produced in the interaction. Furthermore, the tungsten shields mounted upstream of the target (see Fig. 2.1) protect the UV detectors from the backward flux of slow particles. The high γ_{th} ensures that only electrons and pions with a momentum larger than 4.5 GeV/c emit Cherenkov photons. These two properties make the double RICH set-up almost "blind" to hadrons.

The UV detectors are gas chambers consisting of 3 amplification stages, two Parallel-Plate Avalanche Chambers (PPAC) and a Multi-Wire Proportional Detector (MWPC) operated with 94% He/6% CH_4, and saturated vapor pressure of TMAE (Tetrakis(dimethylamine)ethylene) as the photo-sensitive agent. In order to achieve a sufficient partial pressure, the TMAE is heated to 40°. In order to prevent gas condensation and to avoid temperature gradients the whole spectrometer is operated at 50°. The read-out of the UV detectors is provided by two-dimensional arrays of square pads (2.74×2.74 mm^2 in UV-1 and 7.62×7.62 mm^2 in UV-2), about 50000 pads in each, allowing the reconstruction of single-photon hits. Fig. 2.4 shows a central $Pb-Au$ event in RICH-1 and RICH-2.

2.4.2 RICH performance in the 2000 run

The UV detectors were assembled in 1991. During the 1995 run, UV-1 showed a degraded performance and therefore it was refurbished before the 1996 run. The UV-2 detector was never opened since it was assembled. Such a long operation of the detectors, UV-2 in particular, resulted in a number of specific problems during the 2000 run:

- The high beam intensity caused an excessive rate of "overcurrent" conditions (or sparks) and continuous discharges in the multiwire anodes of the UV detectors. UV-1 suffered from discharges and multiple sparks almost every burst, and UV-2 usually had a spark every few bursts. When a spark occurs the UV detector usually recovers by itself. However, when a continuous discharge occurs, it has to be halted and for that the detector has to be taken out of amplification mode. An on-line monitoring software identified the discharges and stopped them by lowering the high voltage (HV) in the detectors by several hundred volts. The voltage was restored after a short break of a few seconds.
- Any event taken during either discharge or spark has no signals in the corresponding UV detector. These events are identified and rejected during the off-line analysis. The fraction of such events is about 25%.
- A few read-out modules were malfunctioning, and only part of them were replaced due to limited number of spare modules. The remaining bad modules are identified during the off-line analysis and the pads belonging to these modules are disabled.
- To keep the spectrometer efficiency at the designed level, the total gain of the UV detectors must be constant within ± 20%. This was achieved by on-line gain monitoring and manual adjustment of the HV.

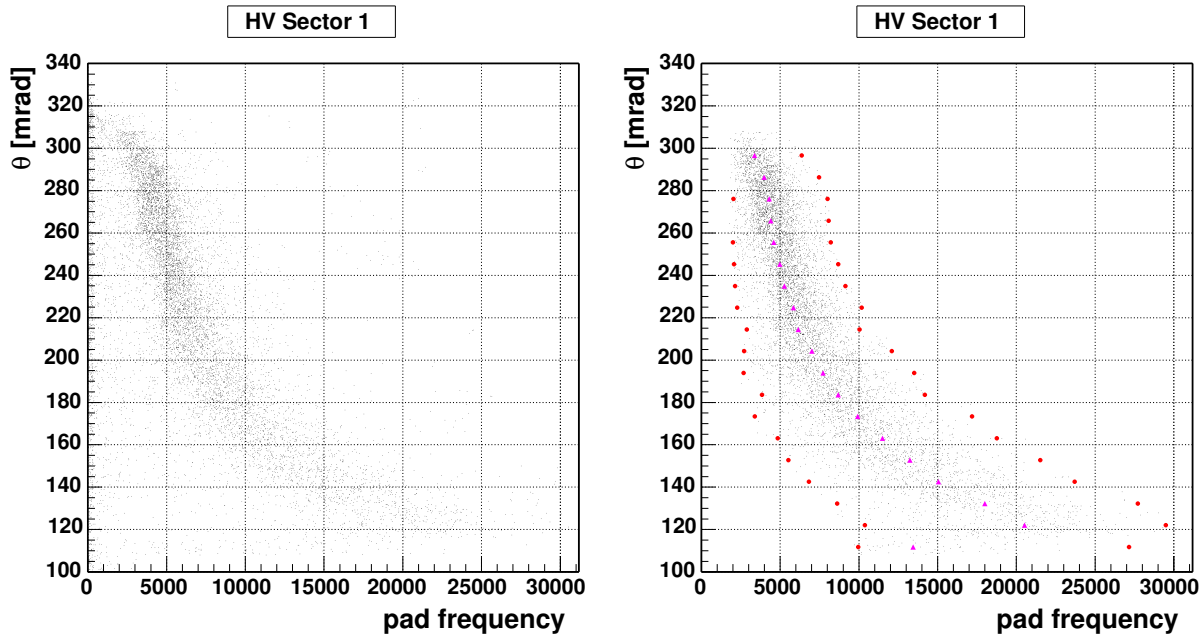

Figure 2.5: Left - example of pad θ as a function of pad frequency distribution in one HV sector. Right - same distribution for the good pads. The magenta triangles are the mean of gaussian fits to 20 slices in θ; the red points are the $\pm 3\sigma$ boundaries of the gaussian fit.

- The gain of the UV detectors is non-uniform over the different areas of the detectors. This results in a non-uniform hit reconstruction efficiency and mean hit amplitude, which are important in the physics analysis. Therefore, a gain calibration within each UV detector is performed in the off-line analysis. The procedure is described in the next section.

2.4.3 RICH gain calibration

There are two effects resulting from the non-uniform gain in the UV detectors: variations of the mean hit size and of the mean pad amplitude. The hit size cannot be corrected, therefore the only purpose of the gain calibration procedure is to bring the mean pad amplitude in the RICH detectors to the same level. The procedure is identical in both RICH detectors. I shall illustrate it using RICH-1.

The RICH-1 MWPC is divided azimuthally into 10 sectors by radial spokes. Each 2 adjacent sectors are operated by a separate HV power supply, and they are called a HV sector. In a given data sample each pad is characterized by its angular coordinates θ_i and ϕ_i, a mean amplitude $< a_i >$ and a pad frequency f_i. f_i is the number of times that pad i fired and its amplitude exceeded a given threshold in a given data sample. Fig. 2.5 (left panel) shows an example of two-dimensional distribution of θ versus pad frequency in one HV sector. The behavior is very similar for all HV sectors. Using those distributions we

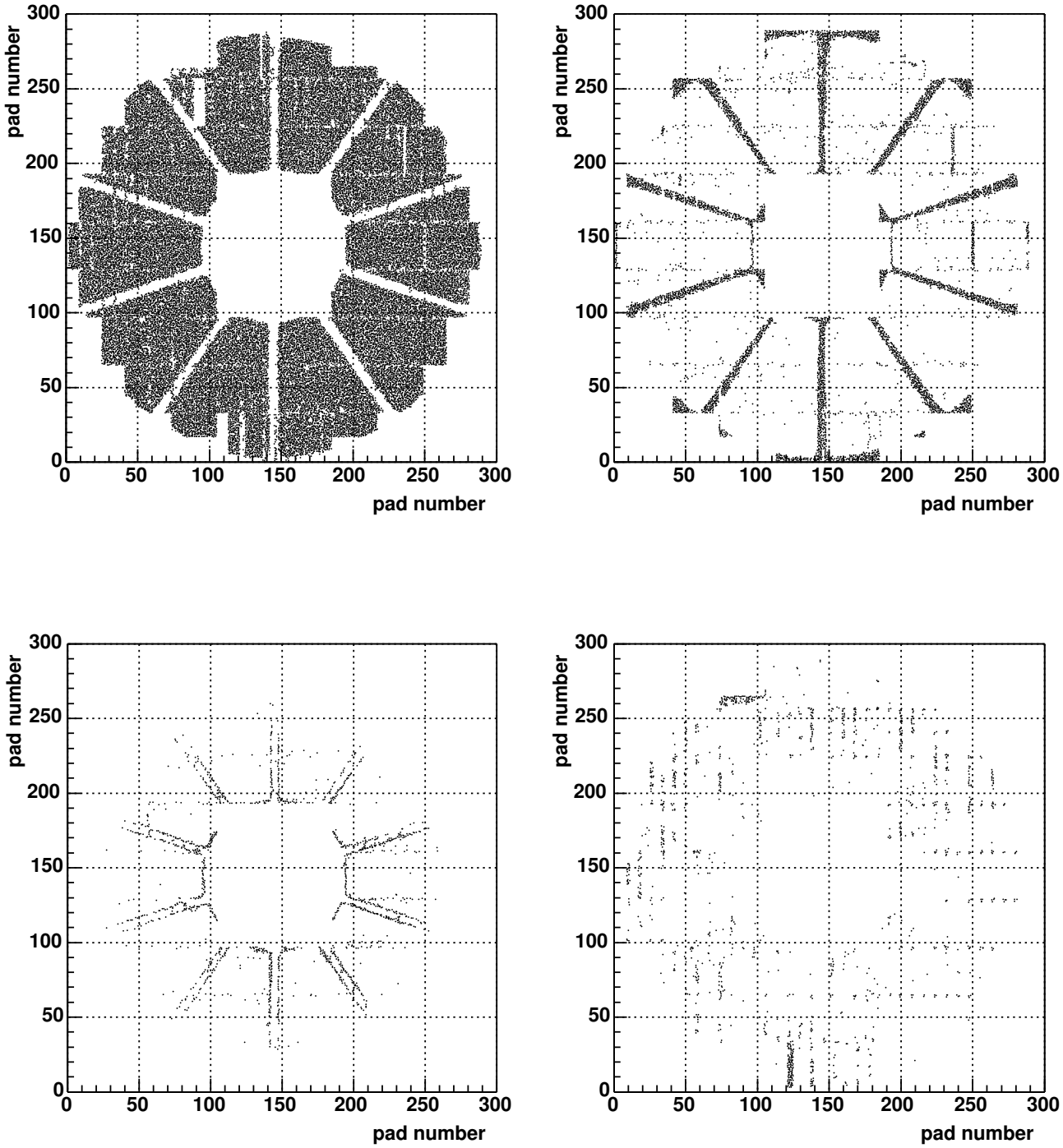

Figure 2.6: Top left - good pads; top right - pads with almost zero frequency; bottom left - low frequency pads; bottom right - high frequency or noisy pads. The coordinates on the axes are given in pad units.

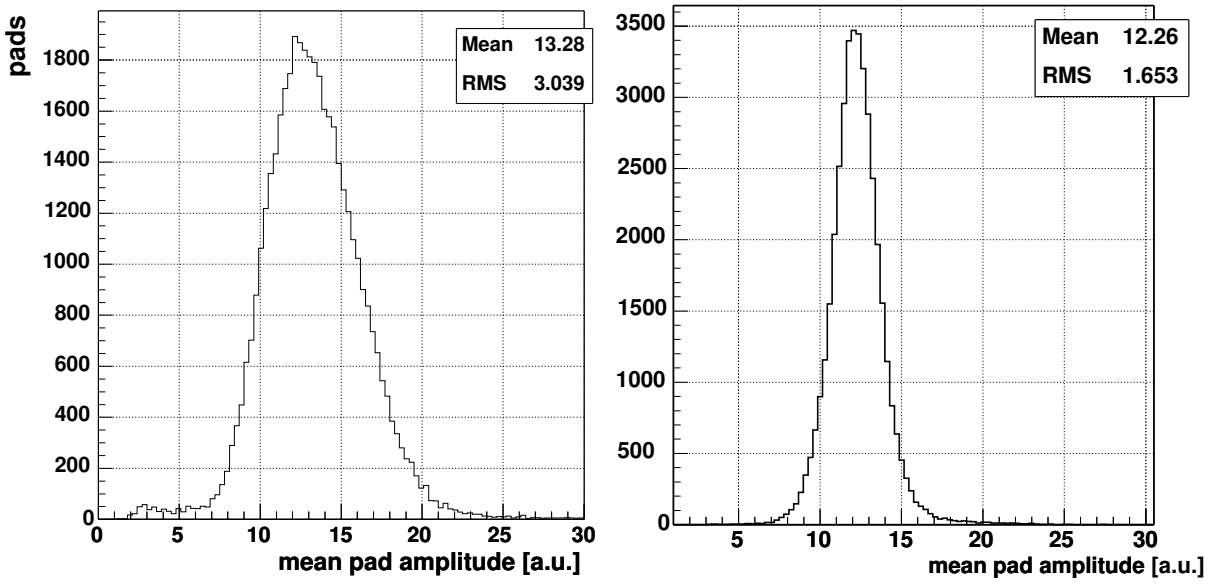

Figure 2.7: Distribution of mean pad amplitude for one calibration unit before (left) and after (right) gain calibration.

define pads with regular behavior. The distribution is divided into 20 θ bins and each slice is fitted with a gaussian. All pads which are within a distance of $\pm 3\sigma$ from the fitted mean are considered as good pads. The right panel of Fig. 2.5 shows the good pads obtained from the plot in the left panel.

The pads with non-regular behavior can be divided into 3 classes:

- Pads which have almost zero frequency. In Fig. 2.5 they are identified as the pads with a frequency below a few hundreds. These pads lay under the spokes or out of the acceptance, as shown in Fig. 2.6 top right panel.
- Pads which have a frequency lower than the -3σ threshold, but higher than the previously defined class. Most of those pads lay close to the boundaries of the spokes and to the edges of the acceptance (see Fig. 2.6 bottom left panel).
- Pads which have a frequency higher than the $+3\sigma$ threshold, mostly due to noise in the read-out modules (see Fig. 2.6 bottom right panel). These pads are rejected during the off-line analysis since they can produce fake hits or rings.

The distribution of good pads is shown in the top left panel of Fig. 2.6.

The pad amplitude correction factors are calculated in the following way. The entire data sample is divided into 415 sub-samples with a typical size of about 60K - 70K events per sub-sample. One such sub-sample is called a calibration unit. Approximately 10% of the data in each calibration unit is used for the calculation of the correction factors for the whole unit. The gain calibration proceeds in two steps:

1. Gain calibration within a given HV sector s: the average amplitude of each pad $< a_i^s >$ along with the global average pad amplitude within the entire sector $< a^s >$ are determined. Only the good pads are used for the $< a^s >$ evaluation. The first

Figure 2.8: General view of the TPC.

stage gain correction factor is defined as $F_i'^s =< a^s > / < a_i^s >$. It takes into account the gain variation from point to point due to geometrical or electronic gain variation along the HV sector area.

2. Gain calibration between HV sectors: the correction factors $F_i'^s$ are applied to the raw data, and the new average amplitude in each HV sector A^s is calculated. This mean pad amplitude is fixed to 12 ADC counts, which corresponds to a nominal gain of about $2.5 \cdot 10^5$. The total pad gain correction factor is then $F_i^s = 12/A^s \cdot F_i'^s$. It is calculated for all good and low frequency pads. The noisy pads are marked and not used neither in the analysis, nor in the Monte-Carlo simulations. The pads laying under the spokes and out of the acceptance pads are not corrected since due to their very low frequency f_i the calculation of mean pad amplitude $< a_i^s >$ is impossible. However, these pads are used in the analysis. Fig. 2.7 shows an example of the mean pad amplitude distribution for one calibration unit before and after gain calibration.

As mentioned above, the gain calibration procedure is identical in both RICH detectors, except for two details: RICH-2 has 18 hardware and 9 HV sectors, and the mean pad amplitude of all sectors is fixed to 15 ADC counts which corresponds approximately to the same gain of about $2.5 \cdot 10^5$.

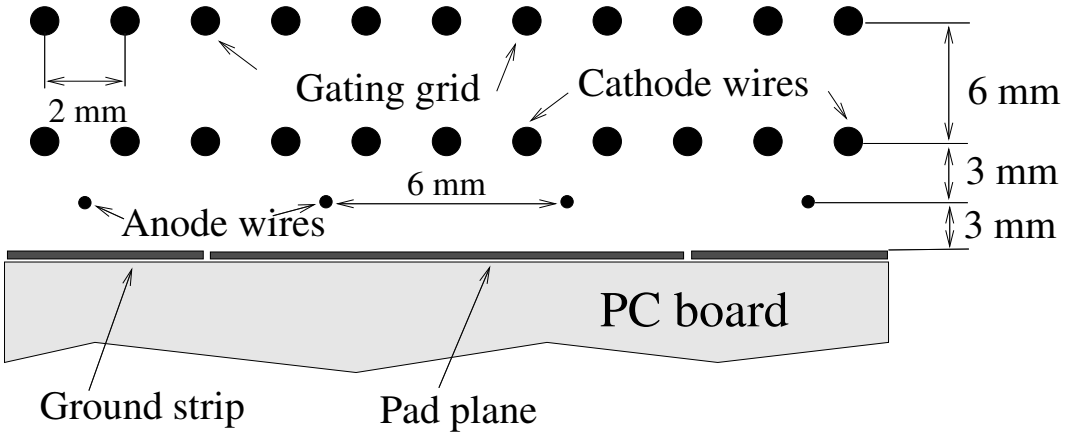

Figure 2.9: Layout of the wire plane of the TPC.

2.5 TPC

The layout of the TPC is given in Fig. 2.8. The shape of the TPC is cylindrical, in order to preserve the axial symmetry. The acceptance of the TPC is the same as for the RICH detectors which corresponds to the polar angles between 8° and 14.5°. The outer radius of the TPC is $R_{out} = 1.31\ m$ and the inner radius, is $R_{in} = 0.5\ m$.

The TPC is operated within a magnetic field, which is generated by two warm coils with opposite currents (up to 4000 A). The resulting radial magnetic field component has a maximum strength in the region between the two coils (see the field lines, indicated by the red dashed lines in Fig. 2.1). The azimuthal kick caused by the radial component of the field allows us to calculate the particle momentum.

A charged particle traversing the gas volume of the TPC produces electron-ion pairs along its trajectory. The electron cloud drifts in the electric field in the radial direction towards 16 read-out chambers that are mounted in a cage-like aluminum structure and define the outer surface of the TPC. The drift field is provided by a cylindrical cathode with a diameter of 97.2 cm, which is kept at a potential of $-30\ kV$ and by the cathode wire planes of the read-out chambers at a potential of about $-150\ V$. In order to cancel edge effects of the electric field, two voltage dividers enclose the drift volume at the endcaps of the TPC.

The TPC is operated with a 90% Ne/10% CO_2 gas mixture. This mixture was chosen as an optimum compromise between small diffusion, high primary ionization, long radiation length and reasonably fast drift velocity. The position resolution is a function of the polar angle θ. It varies between 300 and 400 μm in the azimuthal direction and between 600 and 800 μm in the radial direction [42, 36]. The mean values are $r\Delta\phi = 340\ \mu m$ in azimuthal direction and $\Delta r = 637\ \mu m$ in radial direction.

2.5.1 Read-out chambers

The barrel of read-out chambers consists of 16 identical chambers of $200 \times 50\ cm$ (see Fig. 2.8). Each chamber has 3 wire planes and a pad electrode plane (see Fig. 2.9):

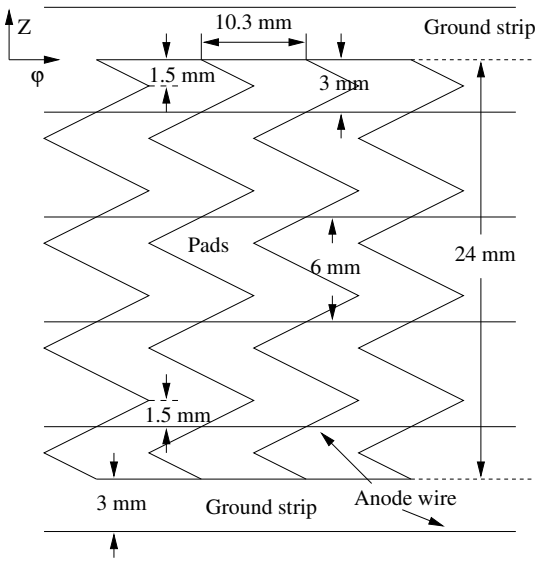

Figure 2.10: Layout of the read-out pads and anode wire orientation in the TPC.

(i) the upper wire plane is a gate electrode made of 1000 $Cu-Be$ wires with a diameter of 75 μm separated by 2 mm. The wire tension is 120 g;
(ii) the next wire plane is the cathode electrode. It is identical to the gate electrode and located 6 mm below the gate electrode;
(iii) the next plane is the anode wire electrode. It contains 300 Au plated tungsten wires of 20 μm diameter with 6 mm spacing and a tension of 45 g. The anode is divided into 6 independent HV sectors in order to allow gain equilibration along the chambers.

The main purpose of the upgrade is to improve the momentum resolution, therefore accurate spatial resolution is needed. It was decided to use the displaced single chevron pad configuration (see Fig. 2.10). This geometry guarantees that the charge arriving to the pad plane is spread over two or three pads allowing a good centroid determination. The detailed description and expected performance of the cathode pad design of the read-out chambers is given in [43, 44]. Fig. 2.11 shows the pad side-layout of the read-out chamber. There are 40 pad rows in the beam direction, separated from each other by ground strips. Each pad row contains 48 pads. Only 20 pad rows are equipped with read-out electronics, providing us with 20 space points per the track.

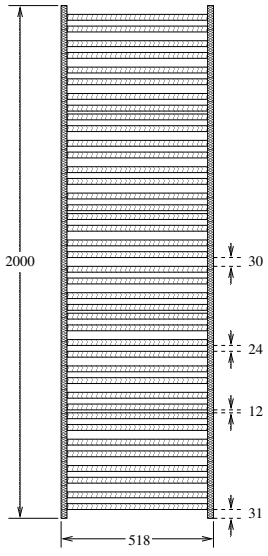

Figure 2.11: Pad side-layout of the readout chambers.

The chamber design and construction were done by our group at the Weizmann Institute. The winding of

wire planes required the development of unique tooling and procedures. A dedicated computer controlled winding machine was designed and built for very precise winding and a dedicated optical system was setup for precise positioning and alignment of the wires with respect to the chevron pad structure. After winding and positioning, the wires were glued to the supporting frames of the chamber. The width of these frames is only 6 mm in order to minimize the dead area of the chambers. The achieved precision of the anode wire position was of the order of 50 μm.

2.6 Trigger and DAQ

Events were selected with a centrality trigger based on three Cherenkov beam counters (BC) and the SiDC-1 detector. The first counter ($BC1$) is placed 60 m upstream of the target. The two another counters are placed before ($BC2$) and after ($BC3$) the target area. The Cherenkov counters provide the interaction trigger defined by $BC1 \cdot BC2 \cdot \overline{BC3}$, *i.e.* a beam particle that enters the target area (signal in $BC1$ and $BC2$) but does not leave it (no signal in $BC3$), while the signal from the SiDC-1 detector is used to select the high multiplicity events. The total sample consists of 32 million events. The main part was recorded with a centrality threshold corresponding to the most central 7% of the geometrical cross section. A few millions events with lower centrality of $10 - 20\%$ were also recorded. As already mentioned, about 25% of the data sample cannot be analyzed due to sparks and discharges in the RICH detectors. This work is based on the analysis of 17.4 million of events with 7% centrality trigger.

Together with the upgrade of the CERES apparatus, a new Data Acquisition System (DAQ) was constructed to cope with high rate of ion collisions as well as with the significant size of central events. To achieve the optimal data recording rate of 350-400 central events/spill (typical raw event size is about 0.5 Mb), the beam intensity was about 10^6 particles/spill (the length of the spill plateau is 4 sec). In the time interval between two spills (15 sec) the recorded data was sent to an event-builder PC in the CERN Central Data Recording facility and the completed events were then copied from disk to tape.

Chapter 3

Data Analysis

3.1 Overview

The experimental challenge of the CERES experiment is to detect a very weak source of e^+e^- pairs in the presence of hundreds of charged particles in central Pb-Au collisions. The strength of the known physics signal from Dalitz decays and resonance decays of the ρ, ω, ϕ is of the order of $4 \cdot 10^{-6}$ per π^0 for m $> 200\ MeV/c^2$ and $p_T > 200\ MeV/c$. In addition, one has a few electron pairs per event from π^0 Dalitz decays and γ conversions. Due to limited reconstruction efficiency of tracks with $p_T < 100\ MeV/c$, the pairing of tracks originating from partially reconstructed π^0 Dalitz decays or γ conversions gives rise to a huge combinatorial background, which depends quadratically on the event multiplicity. Several handles are used in the data analysis to reduce the combinatorial background by more than one order of magnitude.

The analysis of the CERES data proceeds in three steps. In the first step, the hits and then track segments (or rings in the RICH counters) in each detector are reconstructed. This is the most CPU-time consuming part. Using 200 double CPU computers at the CERN computer farm, this step took almost 3 months. In the second step, charged particle tracks through the CERES spectrometer are reconstructed and electron tracks are identified. The cuts applied at this step are loose. Tighter cuts are applied in the last step dealing with the reduction of the combinatorial background by excluding electron tracks originating from γ conversions and π^0 Dalitz decays. The remaining electron tracks are paired together and the physical signal is obtained by subtracting from the total unlike-sign pair yield the combinatorial background (CB):

$$S = N_{e^+e^-} - CB \tag{3.1}$$

Under the assumption that the number of electrons or positrons per event follows a Poisson distribution, one can easily prove that the combinatorial background is given by the geometrical mean of the like-sign electron pairs:

$$CB = 2\sqrt{N_{e^+e^+} \cdot N_{e^-e^-}} \tag{3.2}$$

In order to reduce the statistical uncertainty in the signal, a smooth background is generated (see Section 3.5 for further details) and its integral is normalized to the measured

like-sign yield given by equation (3.2).

3.2 Individual detector response

3.2.1 SiDC segment

Hit reconstruction

The SiDC raw data is a collection of cells (360 *anodes* $\times$ 256 *time bins*) with their amplitudes. Adjacent cells are joined into clusters used for the hit reconstruction. The hit and track reconstruction algorithms are described in details in [45]. Briefly, the procedure is as follows:

- Active cells with the amplitude above a certain threshold are grouped into clusters. The dead areas are included into the clusters in order to prevent artificial hits;
- A cluster is divided into subclusters (a slice in the time direction) and all local maxima are calculated. If there is more than one local maximum, the local minima are also determined. If the amplitude of the minimum is less than 10% of that of maximum, the two pulses are separated and treated as if they were two single ones and fitted with a Gaussian. If not, the pulses are fitted with a double Gaussian.
- The obtained time positions of the pulses are combined in the anode direction within a certain time window and form a hit candidate. If more than one pulse belongs to the hit candidate, a local minimum in the anode direction is searched. If a minimum exists, the hit candidate is split in the anode direction and the hit position is given by the center of gravity.

If a hit is reconstructed from one anode pulse only, its φ position is always in the middle of the anode and has a resolution of ~ 5 *mrad*, while for multi-anode hits the position resolution is ~ 2 *mrad*. As a consequence, the position resolution of SiDC hits and the matching of SiDC tracks to other detectors are functions of the number of hit anodes (examples are shown later, in section 3.3). The top panel of Fig. 3.1 shows the hit distribution as a function of radius r. Smaller radius corresponds to longer drift distance, therefore to larger diffusion and larger probability for multi-anode hits. The bottom panel of Fig. 3.1 shows the relative probabilities as function of radius for the different types of hits in SiDC-1. One sees that the fraction of 3 and more anode hits indeed increases with the drift time. In contrast, the number of single anode hits, as expected, decreases as the drift time increases. The ratios between the numbers of hits with different topologies are the same in both SiDC detectors.

Vertex determination

The vertex of the event is reconstructed in two steps: first, the hits in both SiDC are matched to form tracks; second, all tracks are matched to one point in the target space. This point is defined as the vertex of the event. A detailed description of the algorithm can be found in [46]. It is based on minimization of the distance from all tracks to a point in the target area, which is actually the vertex of the event. Fig. 3.2 shows the

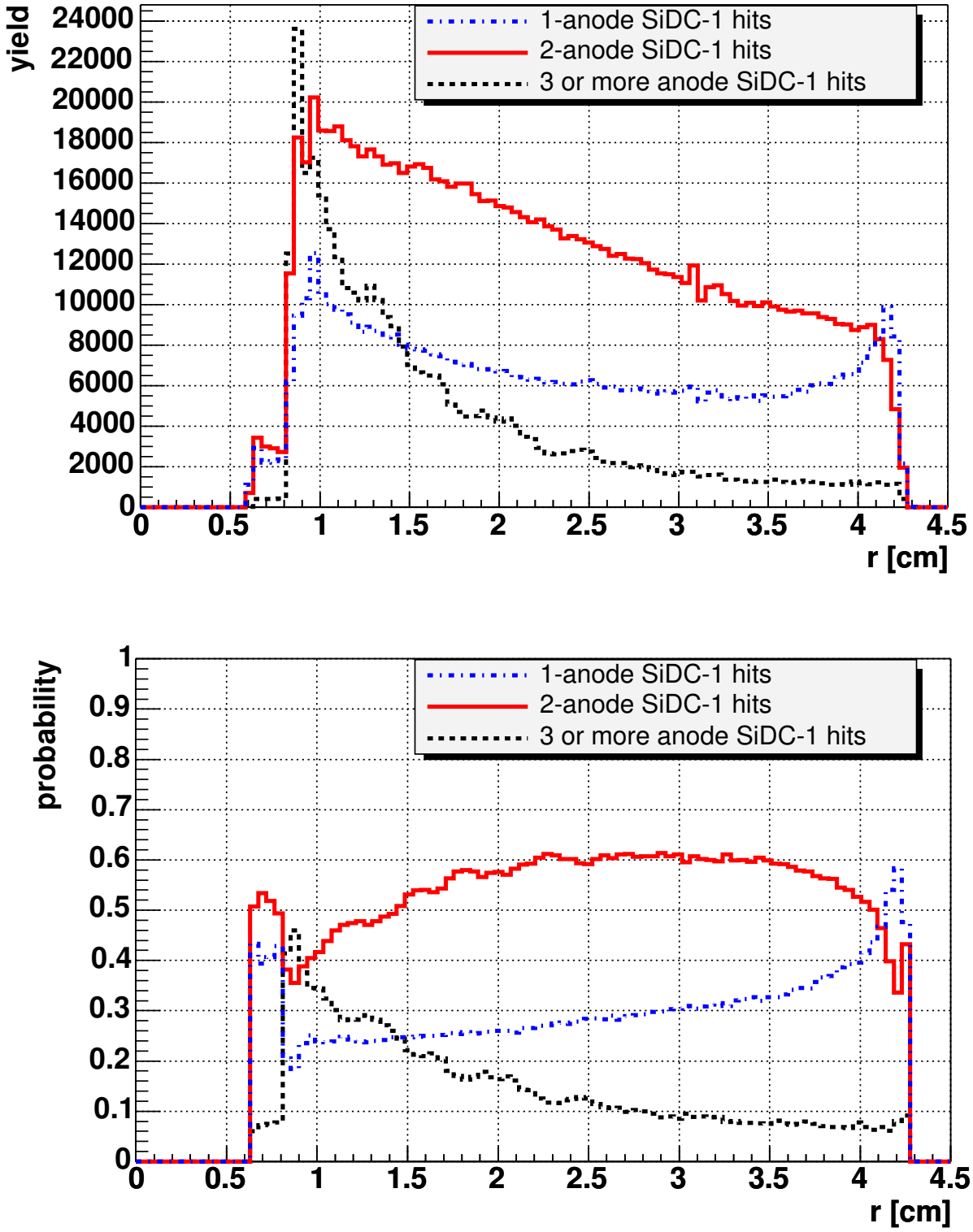

Figure 3.1: Top - hit distribution with different number of anodes as a function of radius. Bottom - relative probability of SiDC-1 hits with different number of anodes as a function of radius.

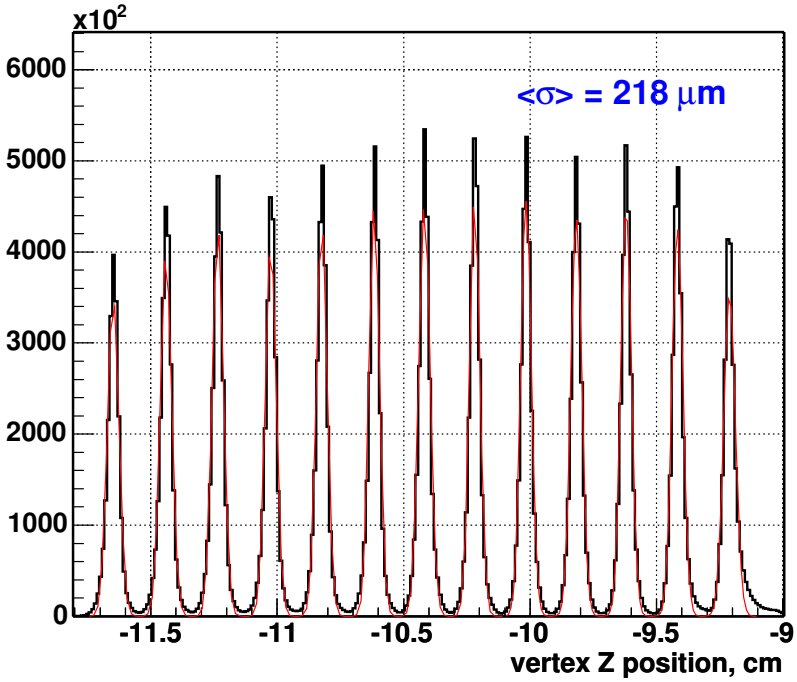

Figure 3.2: Reconstructed vertex position along the beam axis. Each peak corresponds to one target disk. The peaks are fitted with gaussian functions.

distribution of fitted vertex positions along the beam axis. 13 peaks corresponding to the 13 target disks can be perfectly identified.

Track reconstruction

The track candidates are reconstructed using the vertex position and each one of the SiDC-2 hits. A track candidate is defined as the straight line going through a SiDC-2 hit and the event vertex. The point of intersection of the candidate and the SiDC-1 plane is the predictor position. A matching window of 9 *mrad* in radial direction and 50 *mrad* in φ direction is established around the predictor position, and the best matching SiDC-1 hit is determined. The final coordinates of the SiDC track are calculated as an average of the corresponding SiDC-1 and SiDC-2 hit coordinates, requiring that the track goes exactly through the event vertex. If one of the SiDC hits is single-anode and the other is a multi-anode hit, the φ coordinate of the multi-anode hit is used as the track φ coordinate.

3.2.2 RICH segment

Event clean-up

A raw RICH event consists of the location (x, y) and pulse height of each of the pads. The analysis of RICH data begins with the event clean-up. This step is necessary be-

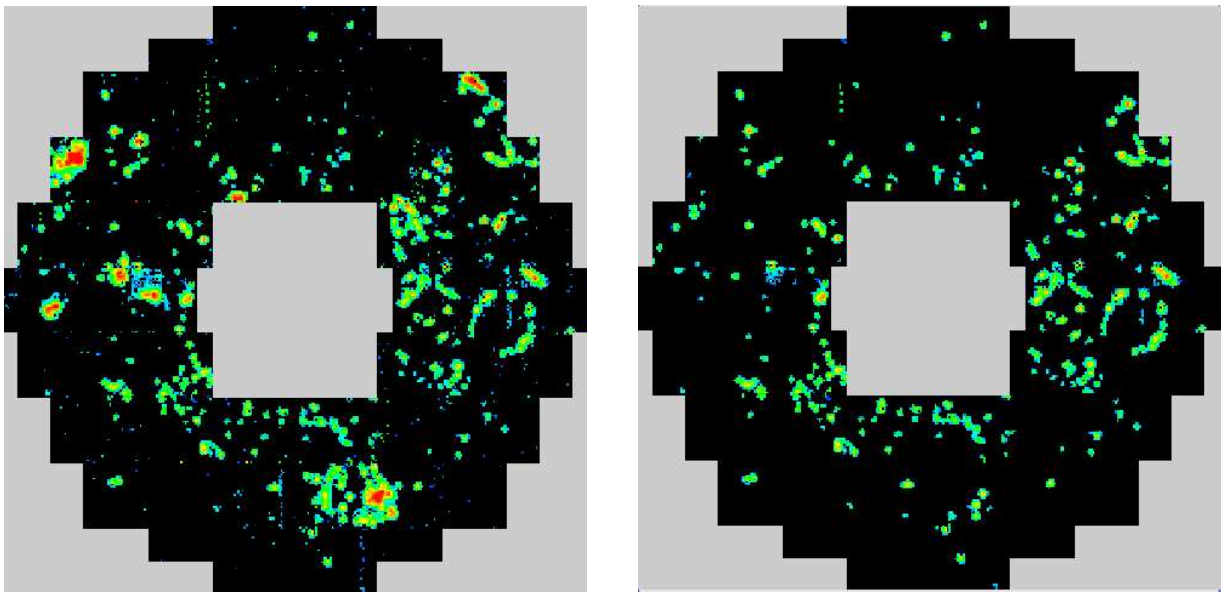

Figure 3.3: Event display of the same event in RICH-1 before (left panel) and after (right panel) the clean-up procedure.

cause on top of the hits from charged particles, there are occasionally large clusters of pads originating either from a highly ionizing particle traversing the detector plane at a small angle (with respect to the plane itself), or from the electronic noise from defective electronic modules. These clusters have to be removed in order to minimize the number of fake hits. There are also isolated one and two pad clusters (mainly due to pedestal fluctuations) which have to be removed as well. To illustrate the clean-up procedure, we show in Fig. 3.3 a typical event in RICH-1 before and after the clean-up.

Hit reconstruction

RICH hits are reconstructed from the pad clusters surviving the clean-up procedure. A hit in the RICH detector is defined as the center of gravity of a cluster of active pads. A cluster may contain more than one hit due to the pile-up of hits if they fall close to each other. A hit splitting procedure is applied if more than one local maximum is found in the pad cluster. The procedure is performed by iterative increase of the amplitude threshold from the minimum value of 1 count up to the point when the cluster breaks up into two or more subclusters, defined as single hits.

Ring reconstruction

The RICH counters are the primary tool of electron identification in the CERES spectrometer. Electrons and positrons emitting Cherenkov photons are ultra-relativistic, *i.e.*

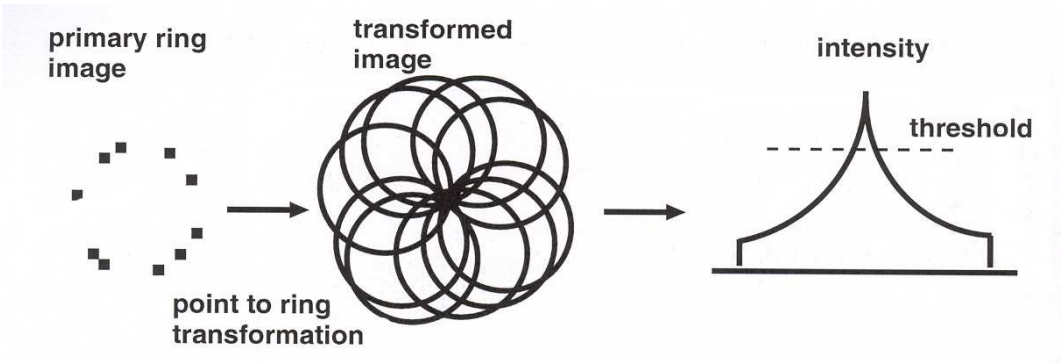

Figure 3.4: Illustration of the RICH center finding by a Hough transform.

they have $\beta \to 1$, and the angle of Cherenkov photon emission is constant:

$$cos(\theta) = \frac{1}{n\ \beta} \to \frac{1}{n} \tag{3.3}$$

where n is the medium refractive index. In other words, electrons and positrons produce rings with fixed, or asymptotic radius $R_\infty = f/\gamma_{th}$.

The ring reconstruction procedure is divided into two parts. First, the ring center candidates are determined, and second, a robust ring fitting procedure is applied.

As mentioned before, the magnetic field between the two RICHes was switched off, and both RICHes are treated in the same way. After resizing RICH-2, the patterns of fired pads in the two detectors are merged and a point-to-ring Hough transformation [47] is applied to the combined pattern to reconstruct the ring centers. The procedure is schematically illustrated in Fig. 3.4. Around each fired pad a ring with asymptotic radius is assigned. The resulting pattern covering the whole RICH pad plane has peaks at the places of the real ring centers. The peaks with amplitudes above a certain Hough threshold are assumed to be ring center candidates. For each candidate a robust ring fitting procedure [14] is applied in order to determine the precise position of the ring center and the corresponding number of hits per ring. Fig. 3.5 shows an example of RICH-1 event with fitted rings.

The mean Hough amplitude varies with the polar angle of the RICH segment, as illustrated in Fig. 3.6. Within the full ring acceptance, shown by the 2 vertical red lines, the mean Hough amplitude is almost flat. The small slope is caused by UV photon absorption in the spokes of the RICH window support. Outside the full ring acceptance, the mean Hough amplitude decreases rapidly since part of the UV photons are outside the RICH acceptance.

This algorithm provides a higher RICH track reconstruction efficiency, compared to the same treatment independently applied to each RICH detector. For example, in the case of π^0 Dalitz decays and with a Hough threshold of 150 the overlay Monte-Carlo simulations give a track reconstruction efficiency of about 86% instead of 70% achieved when each RICH is treated separately.

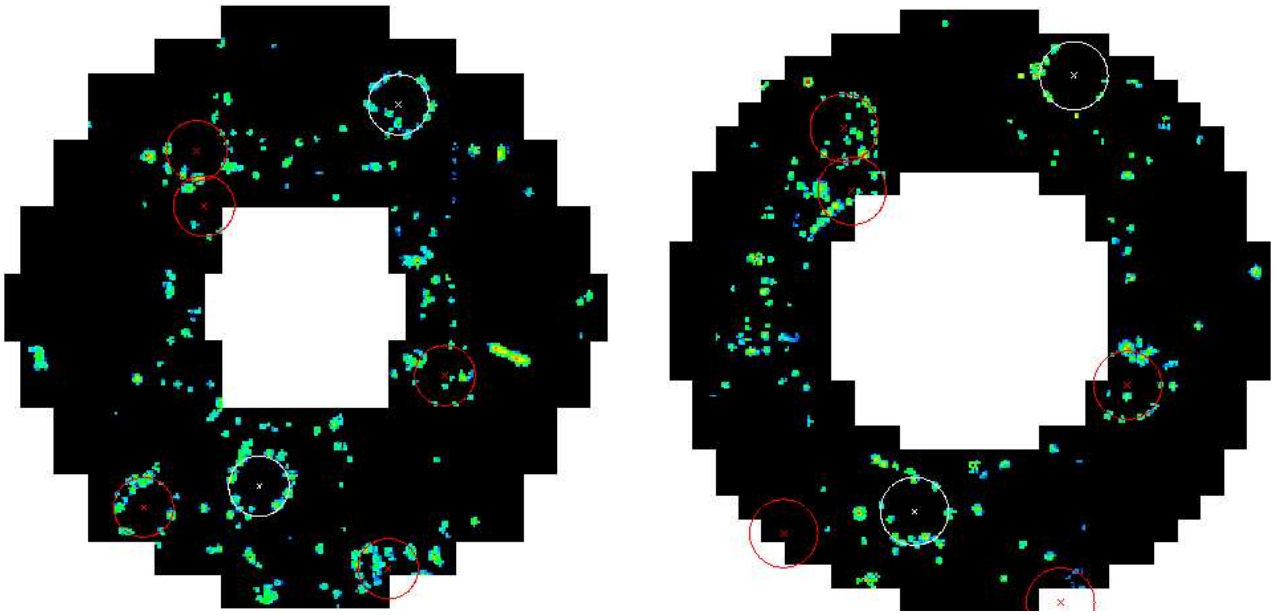

Figure 3.5: Event display of the same event with fitted rings in RICH-1 (left panel) and RICH-2 (right panel).

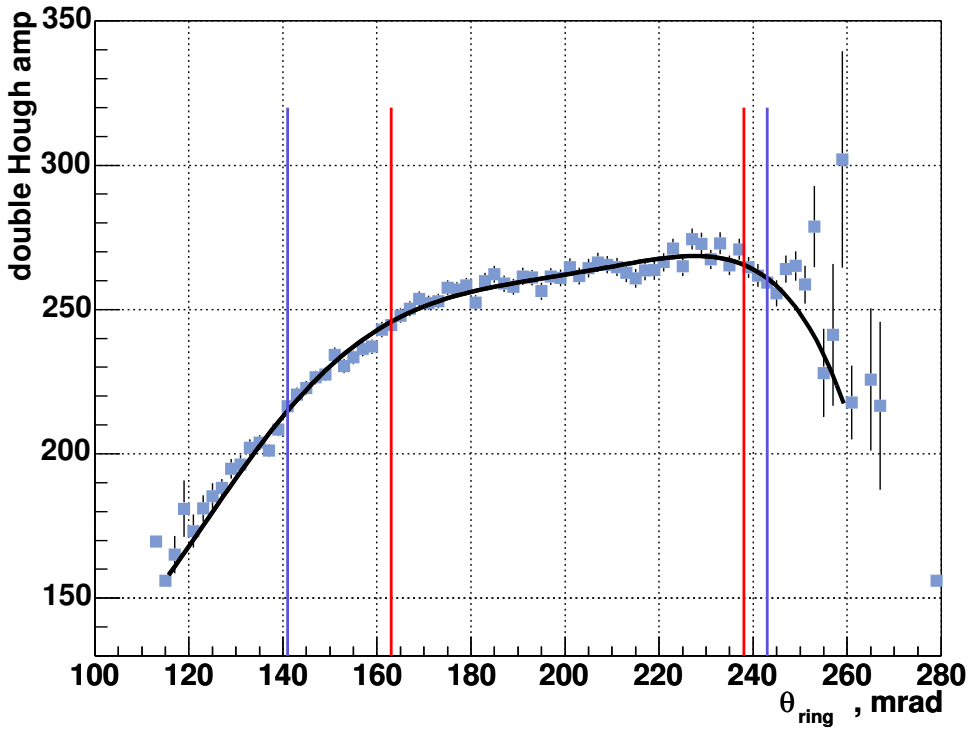

Figure 3.6: Mean value of the Hough amplitude of RICH rings. Black solid line - results of an empirical fit with a polynomial function, red vertical lines - full ring acceptance, blue vertical lines - analysis acceptance $2.1 < \eta < 2.65$

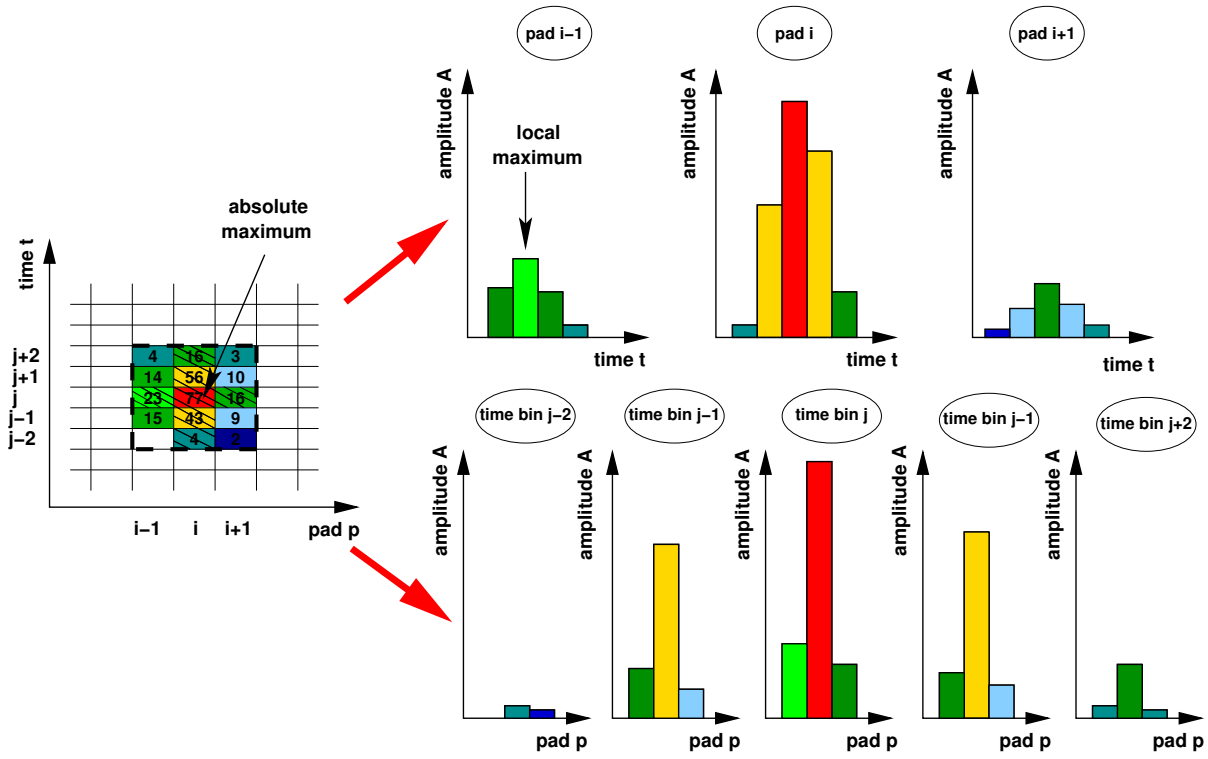

Figure 3.7: Illustration of the TPC hit finding algorithm.

Ring selection

The high multiplicity of the central collision events causes a high occupancy in the RICH counters (more than 10%), and consequently the ring reconstruction algorithm produces many fake rings. For a robust electron track identification, the Hough threshold is increased. Initially, the ring reconstruction is performed with a low Hough threshold of 90, and a higher θ dependent Hough threshold is applied during the electron track reconstruction. The threshold is defined in the following way: the fitted function in Fig. 3.6 is re-scaled so that its maximum is at 150 and the re-scaled function is used as a definition of the new Hough threshold. In addition to this cut, I exploit the fact that the electron track has to cross both RICH counters, and require to see a ring in each one of them. Since the ring reconstruction uses the merged pattern of fired pads, the reconstructed rings have no information about RICH-1 or RICH-2 separately. To obtain it, an additional ring fitting is performed in each RICH independently. The coordinates of the reconstructed RICH tracks are used as predictors for the separate ring center positions. A cut of at least 5 hits per ring in each RICH counter is applied.

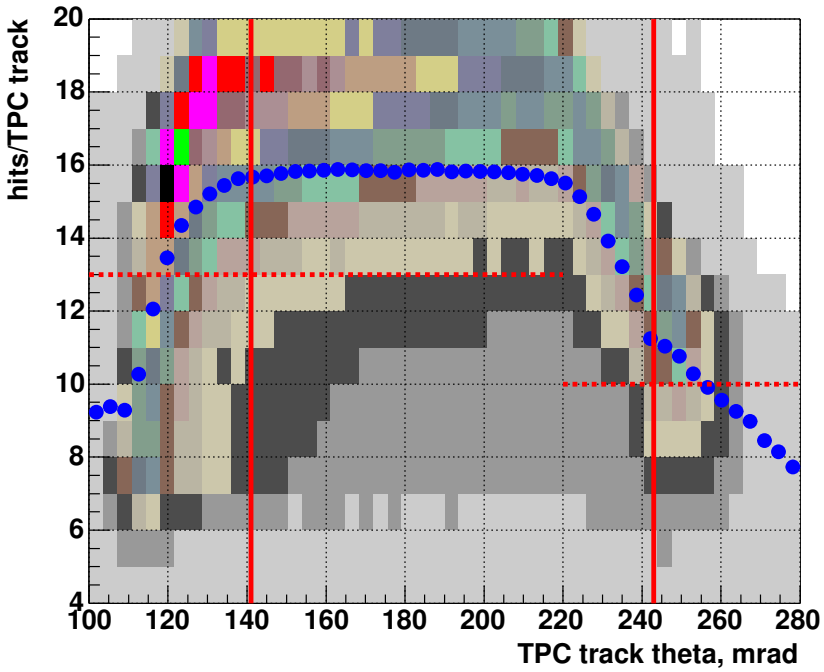

Figure 3.8: Distribution of hits per TPC track as a function of track θ. Blue dotted line - mean value of hits per TPC track. Red vertical lines - θ acceptance used in the analysis. Dotted horizontal lines - the cut applied before matching.

3.2.3 TPC segment

Hit reconstruction

A TPC hit is characterized by a local maximum in the amplitude of adjacent pads and time bins. The amplitudes are stored in a two-dimensional array of pad versus time coordinates. In a first loop, local maxima in the time direction are searched for each pad, followed by a search for local maxima in the pad array for each time bin. Only if the local maxima in time and pad direction are at the same location, this is considered as a local maximum which corresponds to a hit. The procedure is schematically shown in Fig. 3.7. The requirement of a local maximum suppresses the reconstruction of low amplitude hits originating from noise fluctuations. After all maxima are found, the positions of the hits are determined by calculating their center of gravity.

Track reconstruction and selection

The first task of the track reconstruction is the combination of hits to tracks. After that the track is fitted in order to determine the momentum of the particle.

Track finding starts from a candidate hit taken from the plane close to the center of the TPC. Two closest neighbors in z direction are used to predict the sign of the track curvature and the ϕ window in ϕ direction. Within this window, the hits in upstream

and downstream directions are searched. The ϕ position of these hits is predicted with a linear extrapolation using the two previous hits. If no hit is found, the tracking software tries to find the missing hit by fitting a polynomial of second order to already found hits. If the hit is still not found, the tracking in that direction stops.

The magnetic field in the TPC is very inhomogeneous, therefore an analytical description of the particle trajectory is not possible. The momentum of the particle is calculated using two-dimensional fits based on reference tables. The tables contain the hit coordinates of particles with a fixed momentum of 1 GeV/c for different θ angles. The result of the momentum fit is the p_x, p_y and p_z components of the particle momentum.

The mean number of hits per TPC track as a function of θ is shown in Fig. 3.8. The analysis acceptance is denoted by vertical red lines, and the minimum number of hits to define a track is given by the dashed lines. In the full track acceptance, namely up to $\theta = 220$ $mrad$, the tracks are required to have at least 13 hits. For $\theta > 220$ $mrad$ only part of the track is inside the acceptance and the hits per track cut is reduced to 10 hits. This cut rejects about 17% of the TPC tracks within the analysis acceptance. However, about 50% of those tracks start inside the TPC and cannot be used in the global track construction.

The TPC dE/dx signal provides another tool for electron identification in the CERES spectrometer. The separation between pions and electrons in the TPC was studied using a sample of reconstructed tracks enriched with electrons selected with the RICH detectors. The separation is very clear, as illustrated in Fig. 3.9. The distribution of TPC dE/dx signal integrated over momentum is shown in the top panel of Fig. 3.10. The red line represents the dE/dx signal of pion tracks, normalized to fit the measured pion peak. The electron signal, in the bottom panel of Fig. 3.10, is obtained after subtracting the pion contribution from the measured dE/dx signal. A conservative cut in the TPC dE/dx signal dE/dx > 250 is initially applied for a preliminary pion track rejection in the TPC.

3.3 Electron track reconstruction

The main task of the global track reconstruction is to obtain the electron tracks with minimum contamination of fake and hadron tracks while keeping the electron detection efficiency as high as possible. First, the hits in each detector are reconstructed and these hits are used for the reconstruction of local tracks, or track segments, in each detector, as described in the previous section. After a series of selection cuts, the segments are matched in order to reconstruct the global tracks. The TPC segments are matched to the closest SiDC segment and then to the closest RICH ring. Each segment or RICH ring can be used only in one global track.

The matching between track segments from TPC to SiDC or any other pair of detectors is described here. The goal is to find the pair of segments which have the shortest matching distance among all possible combinations. Each segment can be used only once. The matching distance, or just matching, is characterized by $\Delta\theta$ and $\Delta\varphi$ displacements between the segments. Usually the distributions of $\Delta\theta$ and $\Delta\varphi$ can be well described by a Gaussian function. Assuming that, I use 3 σ matching cuts for the track reconstruction.

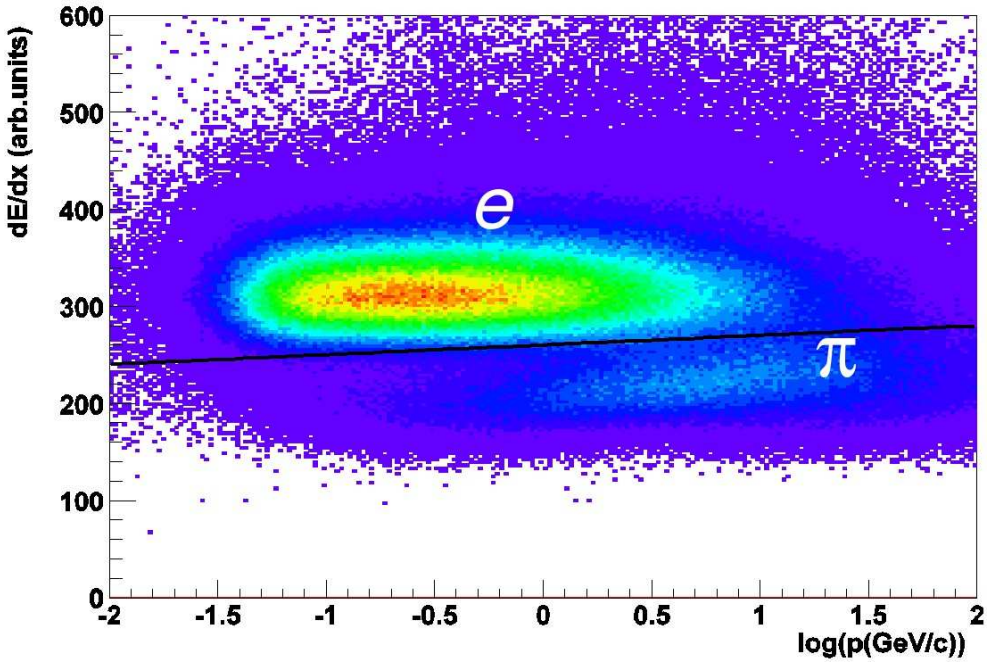

Figure 3.9: TPC dE/dx signal as a function of momentum for the sample of electron tracks enriched by pions.

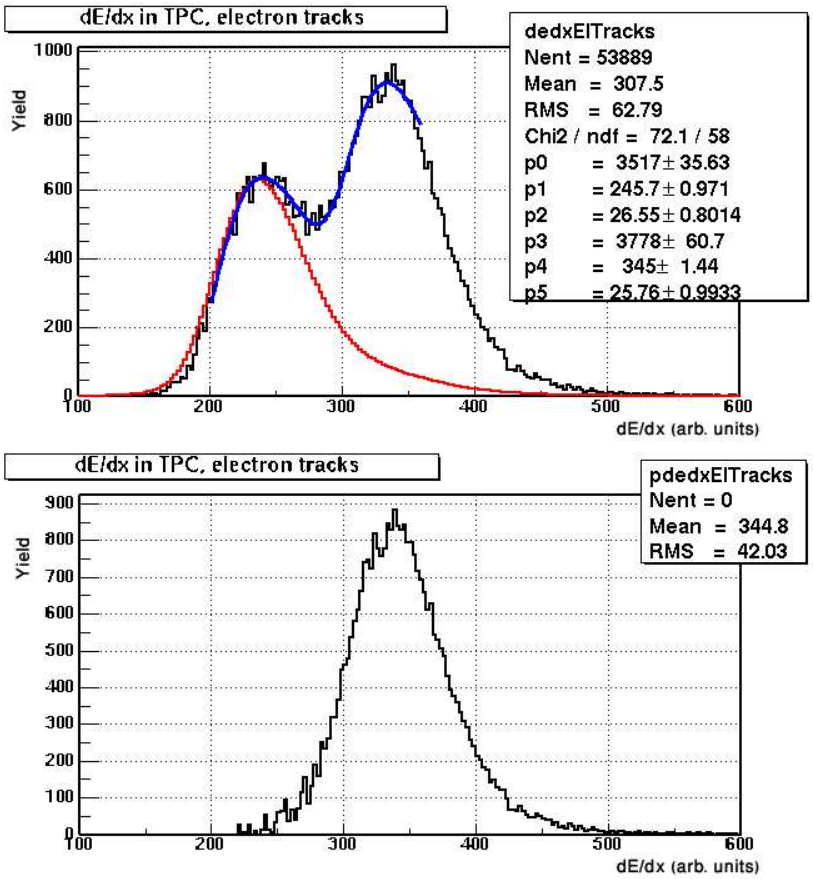

Figure 3.10: Top figure: black line - measured TPC dE/dx signal for a sample of tracks enriched with electrons tracks by selection from the RICH counter, red line - the contribution of clean sample of pion tracks; bottom figure: TPC dE/dx signal of electrons tracks after subtracting the pion contribution.

The matching condition is then the following one:

$$\sqrt{\left(\frac{\Delta\theta}{\sigma_{\Delta\theta}}\right)^2 + \left(\frac{\Delta\varphi}{\sigma_{\Delta\varphi}}\right)^2} < 3 \tag{3.4}$$

There are two main factors determining the resolutions $\sigma_{\Delta\theta}$ and $\sigma_{\Delta\varphi}$. The first one is the multiple scattering contribution which depends on $1/p$. The second one is the intrinsic resolution of the detectors which is momentum independent:

$$\sigma \sim \sqrt{\frac{{p_0}^2}{p^2} + {p_1}^2} \tag{3.5}$$

where p_0 and p_1 are fitting parameters. In addition, $\sigma_{\Delta\theta}$ and $\sigma_{\Delta\varphi}$ depend on the polar angle θ due to the higher detector occupancy at small θ values. $\sigma_{\Delta\theta}$ and $\sigma_{\Delta\varphi}$ are parametrized as functions of both θ and momentum in the following manner:

(i) $\Delta\theta$ and $\Delta\varphi$ distributions are determined for a certain number of momentum and θ bins;

(ii) The background contribution in the $\Delta\theta$ and $\Delta\varphi$ distributions is determined using a random matching procedure: one of the two detectors is "rotated" by a random angle and the matching procedure is repeated.

(iii) After subtraction of the background contribution the $\Delta\theta$ and $\Delta\varphi$ distributions are fitted with a Gaussian function and $\sigma_{\Delta\theta}$ and $\sigma_{\Delta\varphi}$ are extracted;

(iv) $\sigma_{\Delta\theta}$ and $\sigma_{\Delta\varphi}$ are plotted as function of momentum and the distributions are fitted with a function of the form (3.5). The parameters p_0 and p_1 are extracted;

(v) Both p_0 and p_1 are plotted as function of θ and the distributions are fitted with some smooth function;

In addition, the matching involving a SiDC segment depends on the topology of the SiDC hits belonging to the segment. There are 3 different cases: both hits are single anode, both hits are multi-anode, and one hit is single anode and the second one is multi-anode. The differences between all cases are significant and therefore they are treated separately.

I shall illustrate the procedure described above by the detailed description of the parametrization of the SiDC - TPC matching with SiDC segments which have one single anode hit in one of the SiDC and one multi-anode hit in the other. I divide the phase space into 11 *momentum bins* $\times$ 7 θ *bins*.

Now, the parametrization scheme consists of the following 6 steps:

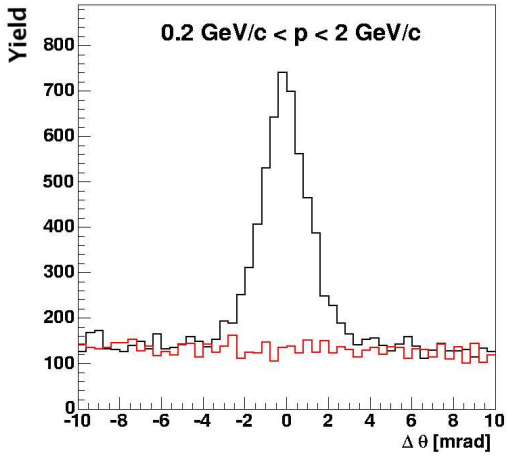

Figure 3.11: Example of real SiDC-TPC matching (black line) and corresponding random background (red line), 160 $mrad < \theta <$ 180 $mrad$.

(i) 77 $\Delta\theta$ and 77 $\Delta\varphi$ distributions with corresponding random background are plotted;
(ii) The background contributions are subtracted using the random matching procedure. As an illustration, Fig. 3.11 shows one $\Delta\theta$ distribution together with its random background;
(iii) The background subtracted distributions are fitted with a Gaussian function. An example is shown in Fig. 3.12 where one sees fitted $\Delta\theta$ distributions in 11 momentum bins for 160 $mrad < \theta <$ 180 $mrad$;
(iv) $\sigma_{\Delta\theta}$ and $\sigma_{\Delta\varphi}$ are plotted as a function of momentum and fitted by a function of the form (3.5), as shown in Fig. 3.13. The variation of the fitted functions in the 7 θ bins is shown in Fig. 3.14. As one sees, the matching width increases as θ decreases. This happens due to the higher occupancy at lower polar angle, which worsens the hit position resolution;
(v) Fig. 3.15 shows the p_0 and p_1 parameters as functions of θ together with an empirical fit providing a smooth behavior. The error bars show the total uncertainty of the fit and the systematic errors (obtained by variation of the fitting range of $\Delta\theta$ ($\Delta\varphi$) and of $\sigma_{\Delta\theta}$ ($\sigma_{\Delta\varphi}$)), added in quadrature.

$\sigma_{\Delta\theta}(\theta, p)$ and $\sigma_{\Delta\varphi}(\theta, p)$ obtained by this procedure are used to reconstruct the SiDC - TPC tracks. Next, the matching between TPC segments of those tracks and the RICH segments is performed following a similar procedure. The SiDC - RICH matching at this stage is redundant and therefore it is not done. SiDC - TPC tracks which have no RICH matching are assumed to be hadrons and are not used in the pair analysis.

3.4 Pair analysis

As already mentioned above, the events with physics signal are very rare. On the other hand, almost every event has a π^0 Dalitz decay or a γ conversion. Furthermore, the TPC track reconstruction efficiency is very low for tracks with $p_T < 100\ MeV/c$. Therefore many of such pairs are only partially reconstructed, *i.e.* one leg is lost. In addition to that, some of the pion tracks are misidentified as electron tracks. All these sources of single electron tracks give raise to a huge combinatorial background which just after the electron track reconstruction gives a signal (S) to background (B) ratio at the level of $\sim 1/200$ for signal pairs with $m > 200\ GeV/c^2$ and $p_T > 200\ MeV/c$. The challenge of the pair analysis is to reduce the amount of this combinatorial background from these 3 sources and to extract the physics signal. One has to remember, that due to the limited statistics of open pairs the rejection cuts cannot be optimized by maximizing the S/B ratio. Such an approach could create a "signal" out of statistical fluctuations. In the present analysis I use the following objective criteria for the cut selection:

1. Fully reconstructed π^0 Dalitz pairs defined as unlike sign pairs with $m < 200\ MeV/c^2$ and $p_T > 200\ MeV/c$ have a good S/B ratio of $\sim 1/1$ already after the electron track reconstruction. The cuts are optimized to improve the S/B ratio of these Dalitz pairs and to keep their reconstruction efficiency as high as possible. In addition, those pairs with opening angle above 35 $mrad$ are assumed to behave similarly to the physics signal. They are used to measure the absolute reconstruction efficiency

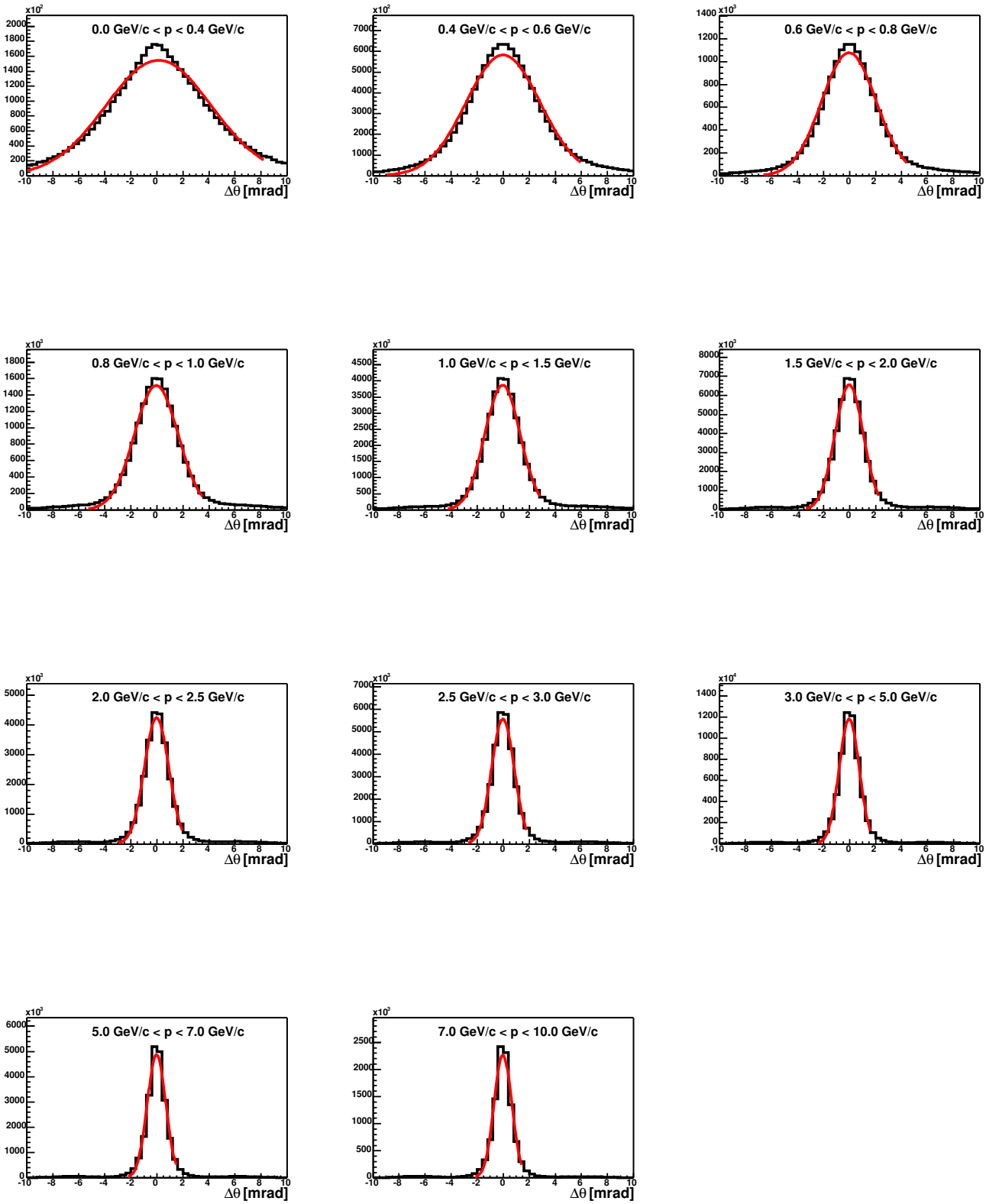

Figure 3.12: $\Delta\theta$ distribution with corresponding gaussian fits in 11 momentum bins, 160 $mrad < \theta <$ 180 $mrad$

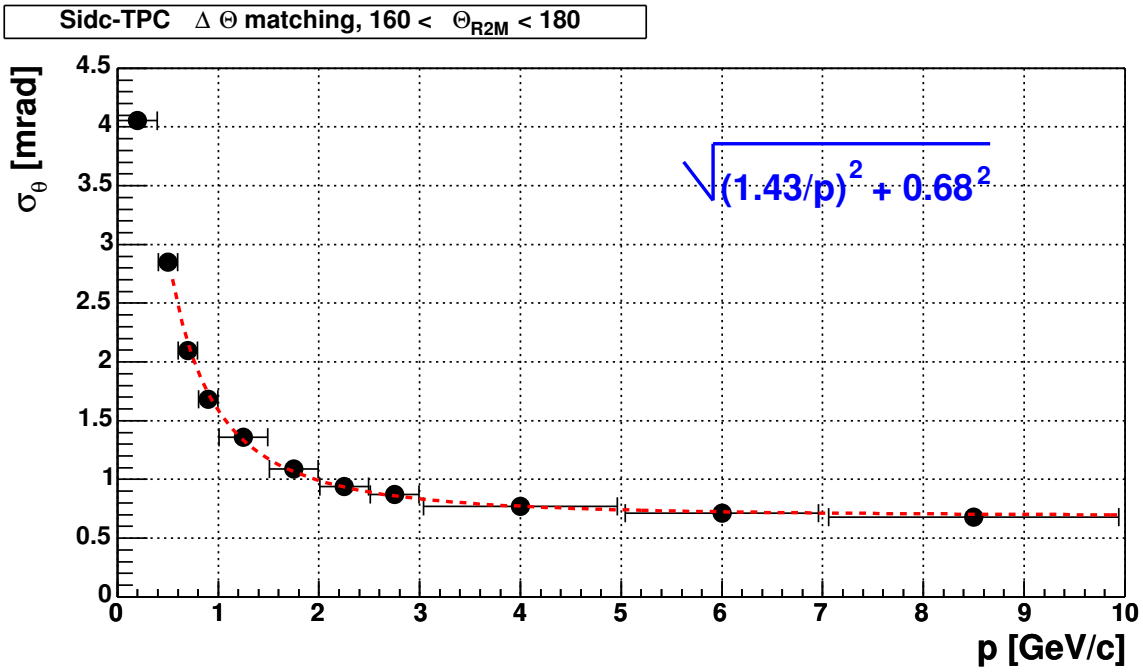

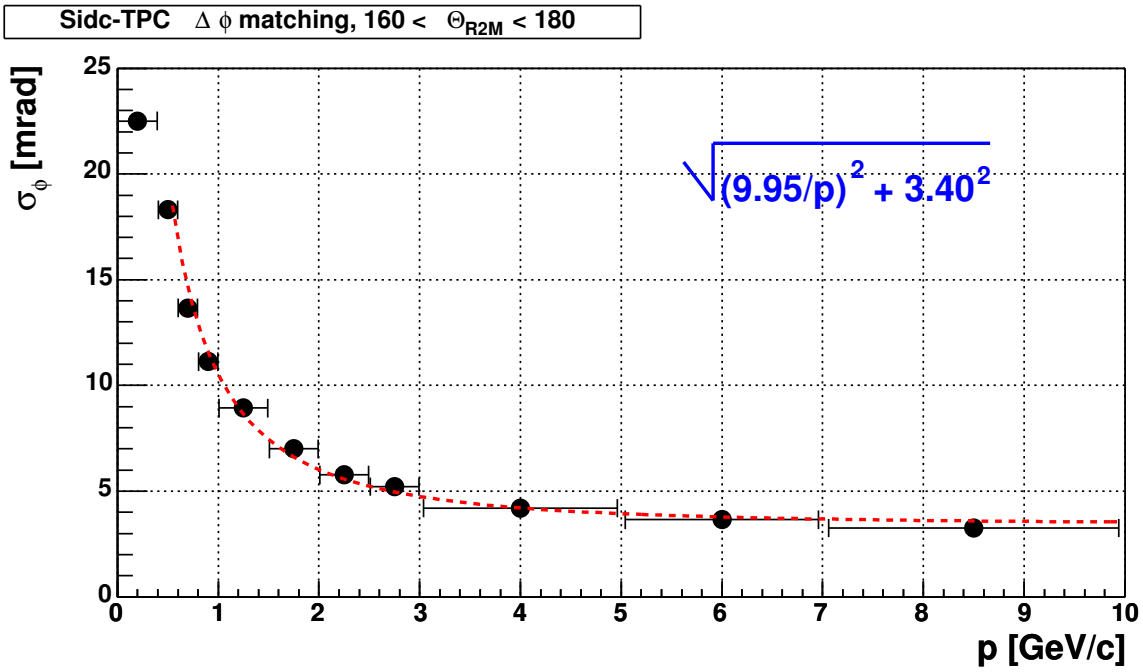

Figure 3.13: $\sigma_{\Delta\theta}$ (top) and $\sigma_{\Delta\varphi}$ (bottom) as functions of momentum for tracks in the polar angle range 160 $mrad < \theta <$ 180 $mrad$. The dashed lines represent the results of the fit with a function of the form (3.5). The fitted parameters are given in the top right corners of each figure.

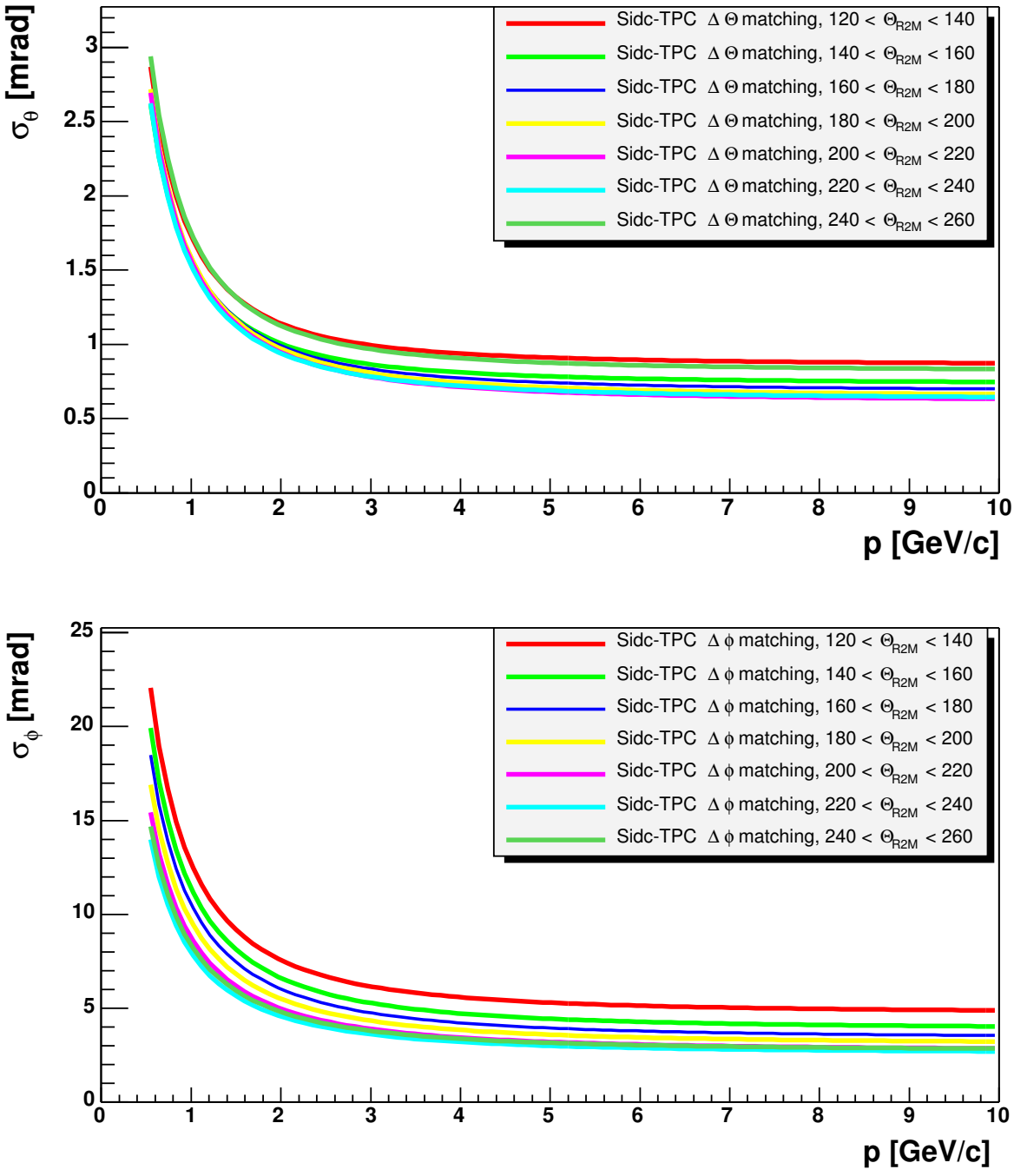

Figure 3.14: Fitted functions of $\sigma_{\Delta\theta}$ and $\sigma_{\Delta\varphi}$ versus momentum in 7 θ bins.

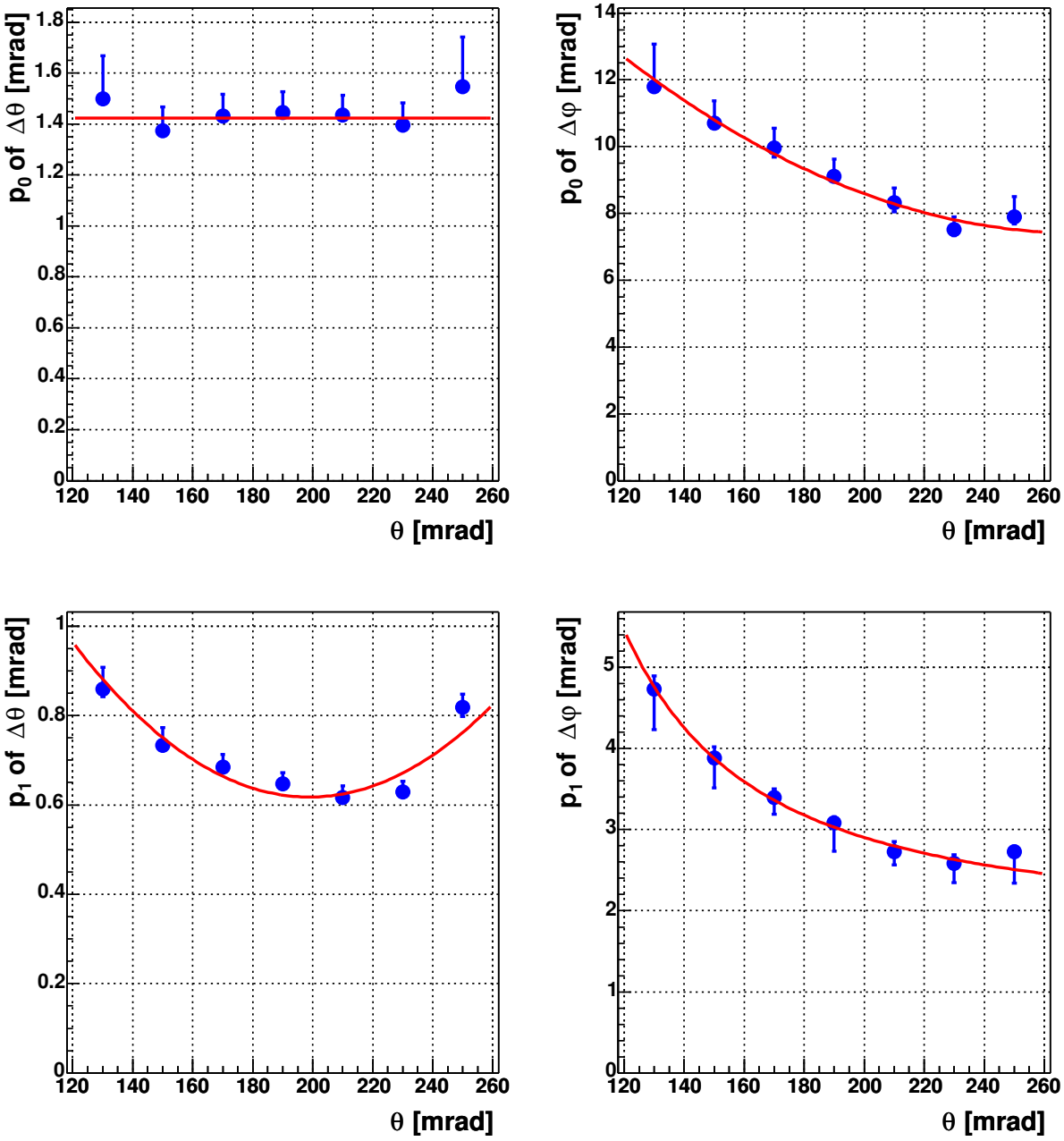

Figure 3.15: p_0 and p_1 fit parameters as functions of θ, fitted with smooth functions. Error bars represent the fit and systematic errors, added quadratically.

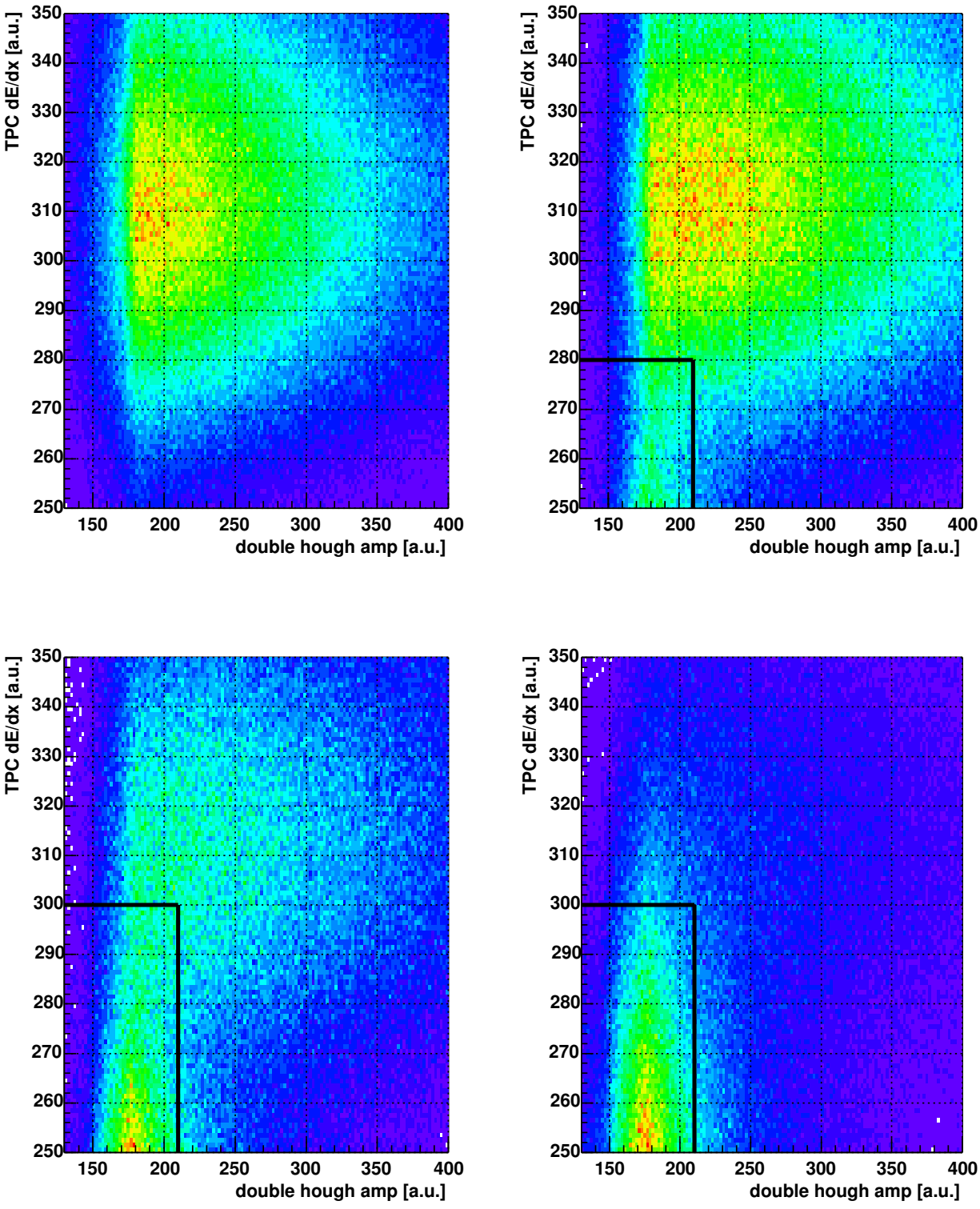

Figure 3.16: Distributions used to identify fake electron tracks or hadron tracks: TPC dE/dx signal versus Hough amplitude in 4 momentum bins. Top left - $p < 1$ GeV/c, top right - $1 < p < 2$ GeV/c, bottom left - $2 < p < 3$ GeV/c, bottom left - $p > 3$ GeV/c. The rejection cut is shown by the solid line.

of the electron tracks.

2. The like sign pairs N_{++} and N_{--} are used to monitor the amount of combinatorial background which survives the cuts.

3.4.1 Pion track rejection

Electron identification is based on the properties of rings in the RICH counters, mainly the Hough amplitude and the number of hits per ring, and the TPC dE/dx signal. Initially, during the electron track reconstruction only loose cuts were applied. Additional pion rejection is achieved using a 2D cut in the TPC dE/dx signal versus the ring Hough amplitude in 4 momentum bins, as shown in Fig. 3.16. A two-dimensional cut is applied since it allows to keep a higher reconstruction efficiency compared to the two independent one-dimensional cuts. The pion peak can be easily identified. Pion tracks are concentrated around low values of both the dE/dx and the Hough amplitude, except for the bin corresponding to the lowest momentum. The reason for the low Hough amplitude is that pion tracks either form a fake ring, or can produce their own ring if their momentum is above 4 GeV/c. In any case, the number of hits per such a ring is lower than in the case of a genuine electron ring. This leads to a lower Hough amplitude as well. This cut also removes fake electron tracks. The fake electron tracks are similar to misidentified pion tracks, since they are produced by a fake ring with low Hough amplitude and low number of hits, matched to a TPC track which most probably was produced by a hadron.

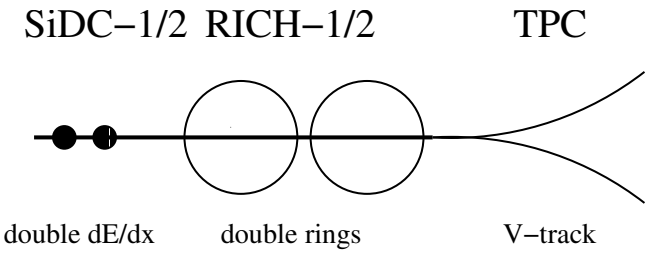

Figure 3.17: Fully reconstructed conversion pattern

3.4.2 Conversion rejection

The rejection of conversions is based on the characteristic pattern which they leave in every detector. Fully reconstructed target conversions are recognized by a double dE/dx signal in the two SiDC detectors, double rings in RICH-1 and RICH-2 and a V-track in the TPC, as shown schematically in Fig. 3.17. π^0 Dalitz decays with very small opening angle produce exactly the same pattern and we therefore refer to those also as conversion pairs. We divide the conversions into 3 categories according to their origin: target conversions, SiDC-1 conversions and late conversions. Each of them is treated separately.

Target conversions

Target conversions have an opening angle which is usually smaller than the double hit resolution in the SiDC. These target conversions can be easily identified by the double dE/dx signal in the SiDC detectors. The definition of single and double dE/dx signal

depends on the topology of the SiDC hits. Fig. 3.18 shows the distribution of SiDC-1 and SiDC-2 hit amplitudes when both hits are multi-anode ones. This distribution was obtained using all electron tracks after fake and hadron track rejection. The double dE/dx peak is clearly visible. The black solid line shows the cut applied to reject the conversions. This is a very powerful cut to reject the target conversions.

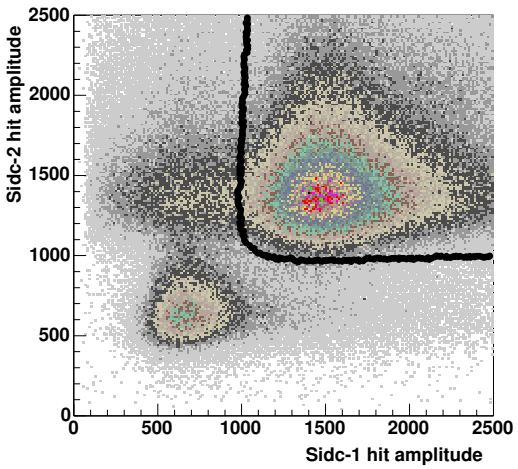

Figure 3.18: SiDC-1 versus SiDC-2 multi-anode hit amplitude. The black line is the cut applied to reject the tracks with double dE/dx signal.

In some cases the SiDC hit reconstruction algorithm leads to an artificial splitting of the hit usually producing 2 single anode hits. Fig. 3.19 shows the distribution of the distance from a 1 anode hit to the closest single anode hit or 2 anode hit. A peak around 3 *mrad* is clearly seen between 2 single anode hits. If the second hit has 2 anodes, the peak almost disappears. The conversions with split hits are identified by a re-summation procedure (see below) and rejected by the double dE/dx cut.

If the opening angle of a conversion or π^0 Dalitz is above the double hit resolution in the SiDC, one has 2 separated hits instead of one double hit. An example is given in Fig. 3.20, showing the distance from the SiDC hit belonging to the electron track to all other SiDC hits within a window of 10 *mrad*. A clear peak is observed which is attributed to conversions. The red line is the same distribution obtained from a sample of pion tracks. Such conversions are identified by a re-summation procedure. In the re-summation procedure the amplitudes of the hit which belongs to the electron track and the closest SiDC hit within a given distance are added. The typical re-summation distance is about $6 - 8$ *mrad* depending on the specific topologies of the hits.

SiDC-1 conversions

Conversions in the SiDC-1 are characterized by a double dE/dx signal in SiDC-2 and a less than double dE/dx signal in SiDC-1 since the conversion happens within the silicon wafer. Here we reject only those conversions which produce a low signal in the SiDC-1. Most of these conversions produce a single anode hit in SiDC-1 and a multi-anode hit in SiDC-2. The corresponding dE/dx distribution is shown in Fig. 3.21. The peak of SiDC-1 conversions is indicated by the black solid line. These tracks are rejected.

Late conversions

Conversions which happen after SiDC-1 do not have hits in the SiDC and therefore should be suppressed by the tracking algorithm. However, due to the high track multiplicity, part of them survive. Also conversions inside SiDC-1 which were not rejected by the last cut are still in the sample. The tools to identify such conversions is the characteristic V-track

pattern in the TPC and the RICH analog response: total amplitude or total number of hits.

The opening angle distribution of the V-tracks is shown by the black line in the left panel of Fig. 3.22. The background, shown by the red line, is obtained using the opening angle distribution of V-tracks where both TPC tracks have the same sign. The amount of background does not allow us to make a simple cut on the opening angle. To make a better selection of the conversions, I study 2 correlations:

1. TPC dE/dx of the additional TPC segment versus opening angle of the V-track, shown in the top of Fig. 3.23;
2. TPC dE/dx of the additional TPC segment versus its momentum, shown in the bottom of Fig. 3.23.

In both figures the background obtained by like-sign V-tracks has been already subtracted. The black lines in both panels of Fig. 3.23 show the cuts applied to reject the V-tracks. The V-track is rejected only if the additional TPC segment fulfills both cuts simultaneously. The opening angle distribution after those cuts is shown in the right panel of Fig. 3.22. The conversions peak is dramatically reduced. The small peak below 2 $mrad$ is rejected by a simple cut on the opening angle.

The last tool to reject the conversions is to identify double rings in the RICH counters. The TPC has a poor reconstruction efficiency for tracks with $p_T < 100\ MeV/c$, therefore many γ conversions do not produce a V-track in the TPC. The double rings are rejected by a cut on the number of hits per ring and the sum analog defined as the total amplitude of the hits which belong to a given ring. The left panel of Fig. 3.24 shows the distribution of sum analog versus number of hits per ring for single rings. The right panel shows the overlay of the same distribution for the double rings and the contours of the single ring distribution taken from the left panel. The cut applied is shown by the red dotted line.

3.4.3 Dalitz rejection

The last step is to identify the π^0 Dalitz decays. Fully and partially reconstructed π^0 Dalitz pairs are shown schematically in Fig. 3.25. After the conversion rejection, all pairs with invariant mass below 150 MeV/c^2 and opening angle less than 50 mrad are marked as fully reconstructed Dalitz decays and their tracks are not used in further pairing. This is justified since the S/B ratio of this sample is $\sim 5/1$ and one can assume that all these pairs indeed originate from π^0 Dalitz decays. In that case, there is no reason to allow the pairing of their tracks to other electron tracks. Partially reconstructed π^0 Dalitz decays, shown in the bottom of Fig. 3.25, have a SiDC-RICH segment close to the fully reconstructed electron track, which was missed by the TPC probably due to its low momentum. To avoid fake segments a narrow SiDC - RICH matching window of $\Delta\theta = 3\ mrad$ and $\Delta\varphi = 15\ mrad$ is applied to identify these segments. The distribution of the opening angle between the electron tracks and the closest SiDC-RICH segments is given in Fig. 3.26. It is compared to the opening angle distribution of fully reconstructed π^0 Dalitz decays and of the π^0 Dalitz decays generated by the GENESIS pair generator. Electron tracks with SiDC-RICH segments within 40 $mrad$ are rejected. The peak at opening angle of $\sim 60\ mrad$ is the result of a specific case when 2 rings touch one another, creating a

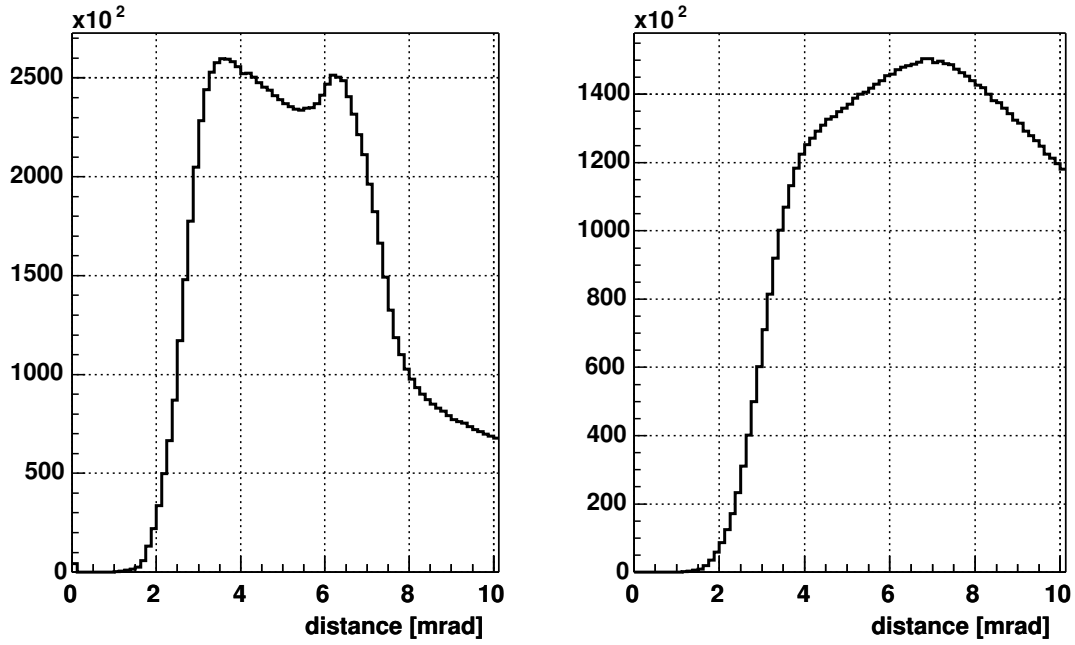

Figure 3.19: Top left - distance from 1 anode SiDC-1 hit to the closest 1 anode hit; top right - distance from 1 anode SiDC-1 hit to the closest 2 anode hit. 2 figures in bottom shows the same for SiDC-2.

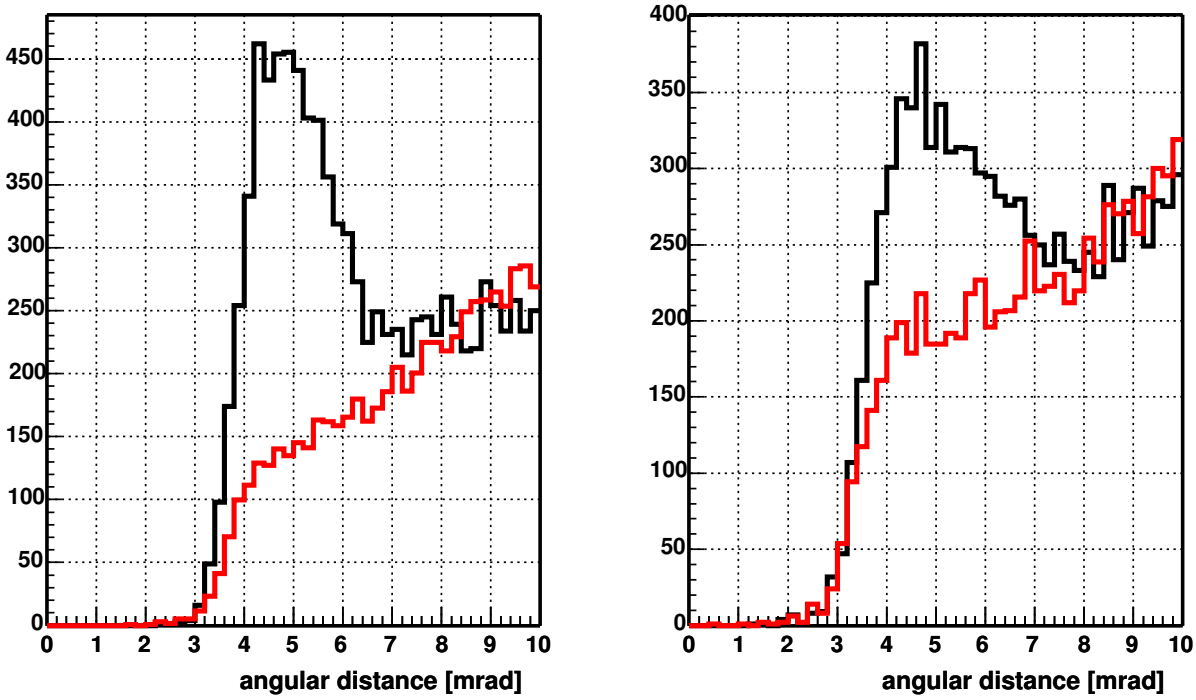

Figure 3.20: Distribution of distance from multi-anode to all single anode hits in SiDC-1 (left) or SiDC-2 (right).

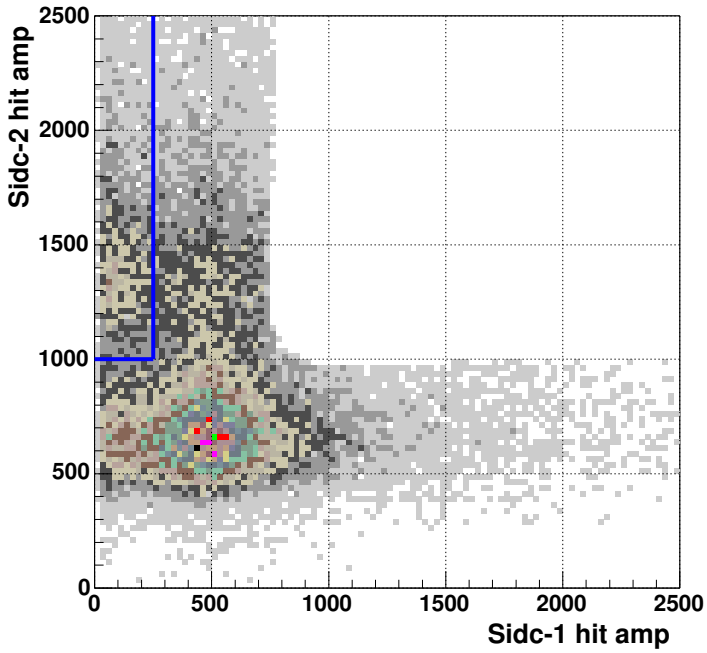

Figure 3.21: SiDC-1 single anode hit amplitude versus SiDC-2 multi-anode hit amplitude. The blue line is the cut applied to reject the SiDC-1 conversions.

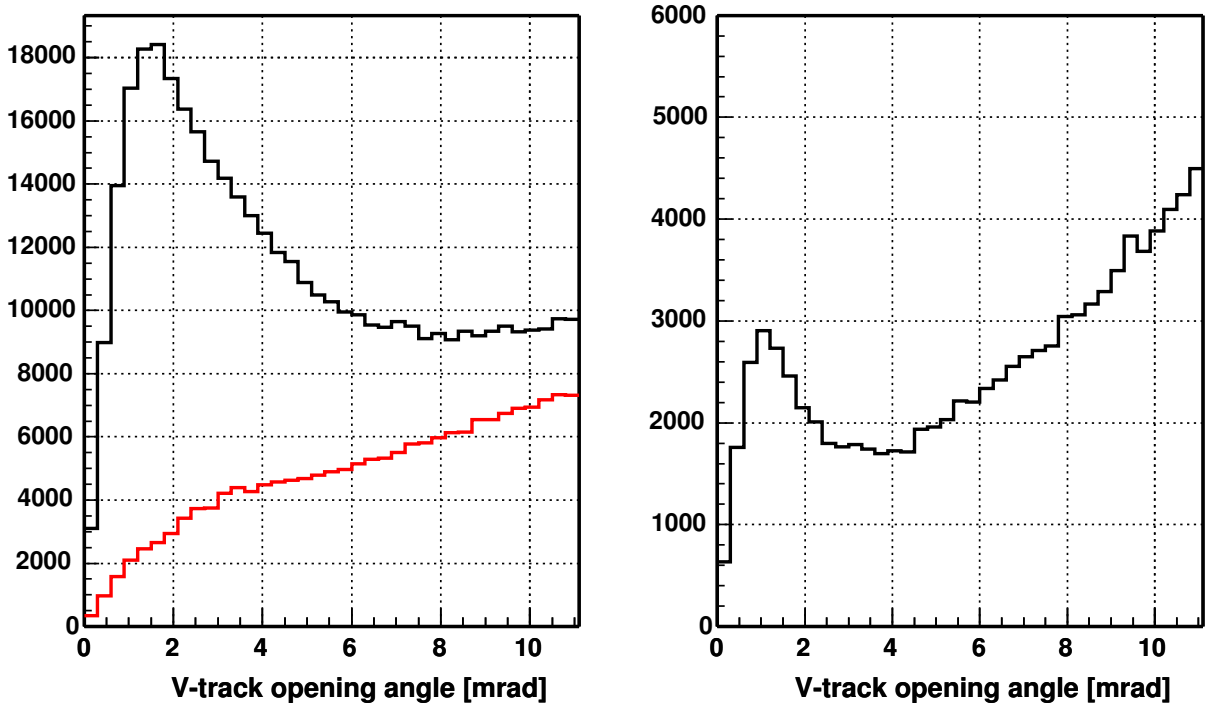

Figure 3.22: Opening angle of the unlike sign V-tracks before (left) and after (right) the V-track rejection. Red line - background obtained by like sign V-tracks.

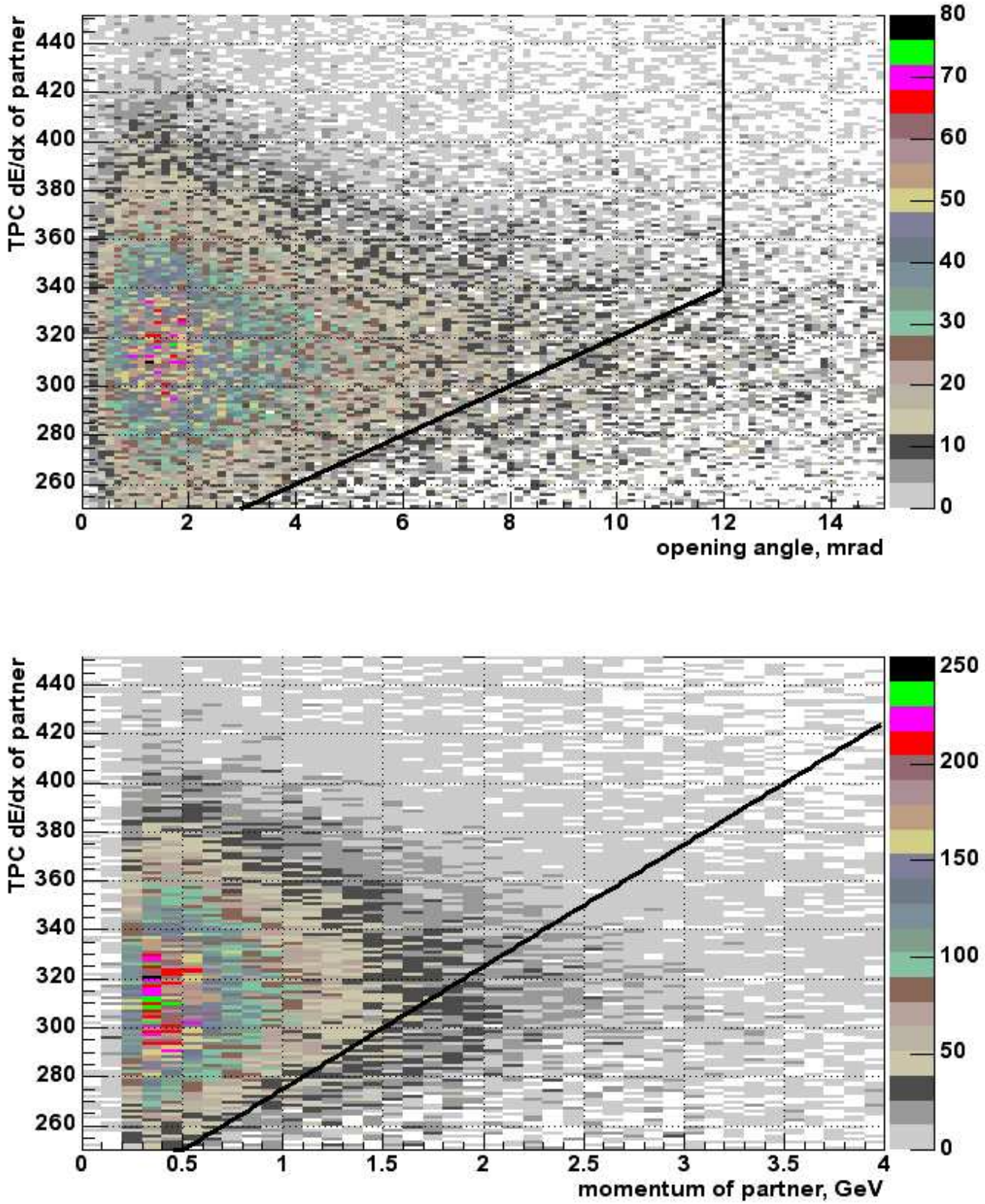

Figure 3.23: V-partner properties

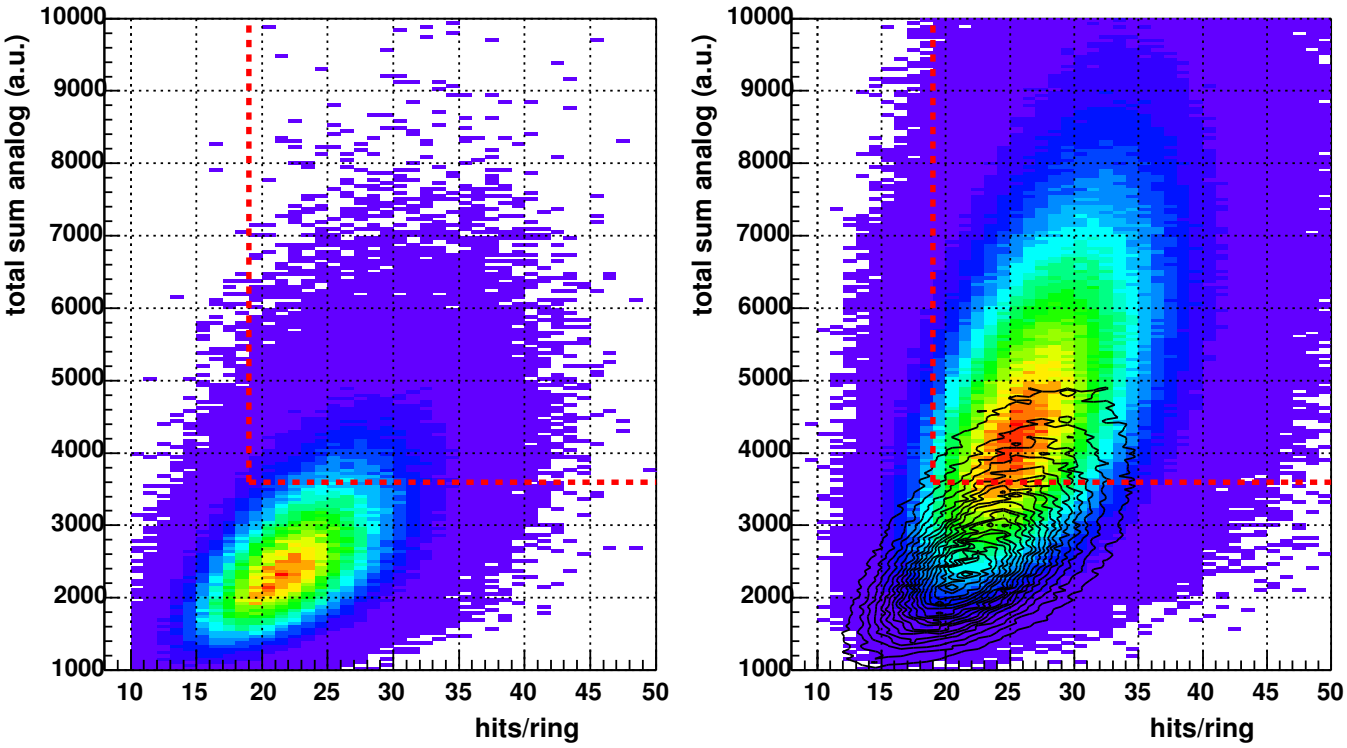

Figure 3.24: Distribution of sum analog versus number of hits per ring. Left panel: distribution for the sample of single rings; right panel: overlay of the distributions for double rings and the contours of the single ring distribution (taken from the left panel).

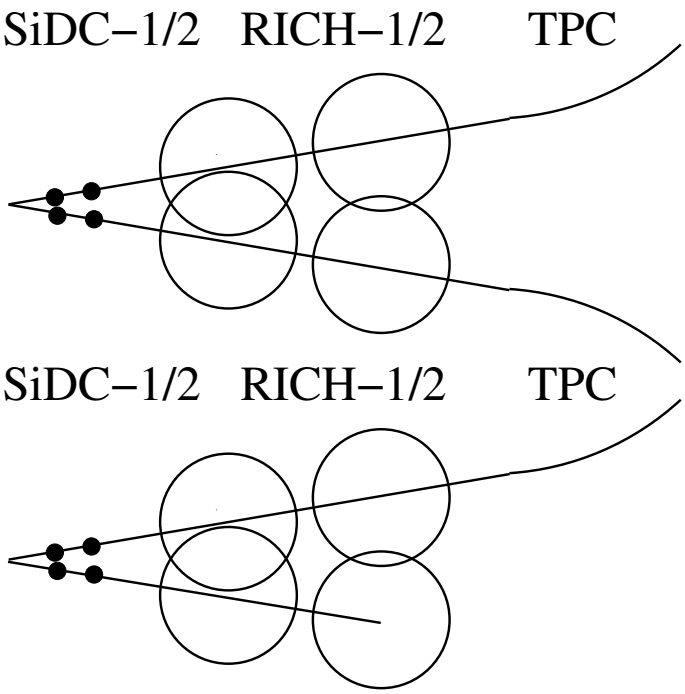

Figure 3.25: Fully and partially reconstructed π^0 Dalitz pairs.

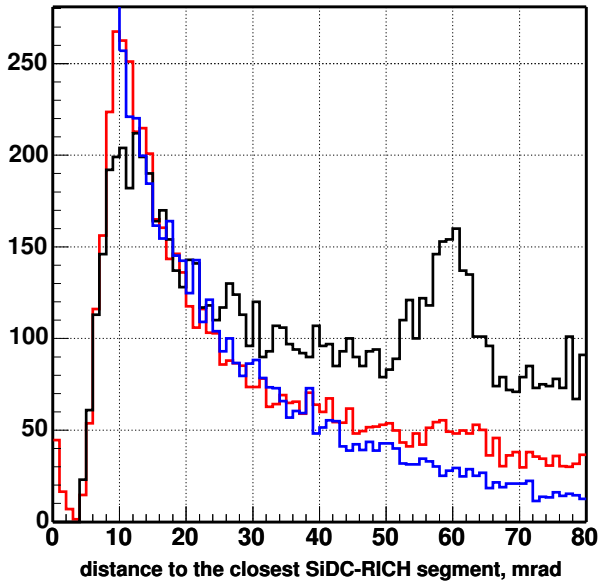

Figure 3.26: Opening angle distribution between electron tracks and the closest SiDC-RICH segments (black line). Red line - Opening angle distribution of fully reconstructed π^0 Dalitz decays. Blue line - opening angle distribution of π^0 Dalitz decays generated by the GENESIS pair generator.

back-to-back ring pattern. This is an artifact of the ring reconstruction algorithm, since the RICH hits are used more than once, and the same hits can belong to two or even more rings. Back-to-back rings don't introduce any bias in the analysis. Their contribution to the physics signal is canceled by the combinatorial background subtraction, and for the π^0 Dalitz rejection only the segments within 40 $mrad$ are used. Fig. 3.26 provides also another justification of the assumption that most of the pairs with $m < 150\ MeV/c^2$ are indeed the π^0 Dalitz decays: their opening angle shape up to 50 $mrad$ follows the opening angle shape of the generated pairs.

3.5 Signal extraction

The rejection cuts were first studied on a fraction of $\sim 40\%$ of the full data set. Once adjusted, they were applied to the whole data set. All tracks with $p_T > 200\ MeV/c$ which survived a given rejection cuts are paired and the physics signal is extracted according to equation (3.1). A minimum opening angle cut of 35 $mrad$ is applied. The p_T cut is the strongest cut in the analysis chain. It is in fact applied after all other cuts in order to allow for the best reconstruction of conversions and π^0 Dalitz pairs. Pairs with $m_{ee} < 200\ MeV/c^2$ are globally defined as fully reconstructed π^0 Dalitz pairs, although they include a contribution of 15% from η Dalitz decays. They are referred as simply Dalitz pairs in the discussion. All other pairs with $m_{ee} > 200\ MeV/c^2$ are referred as

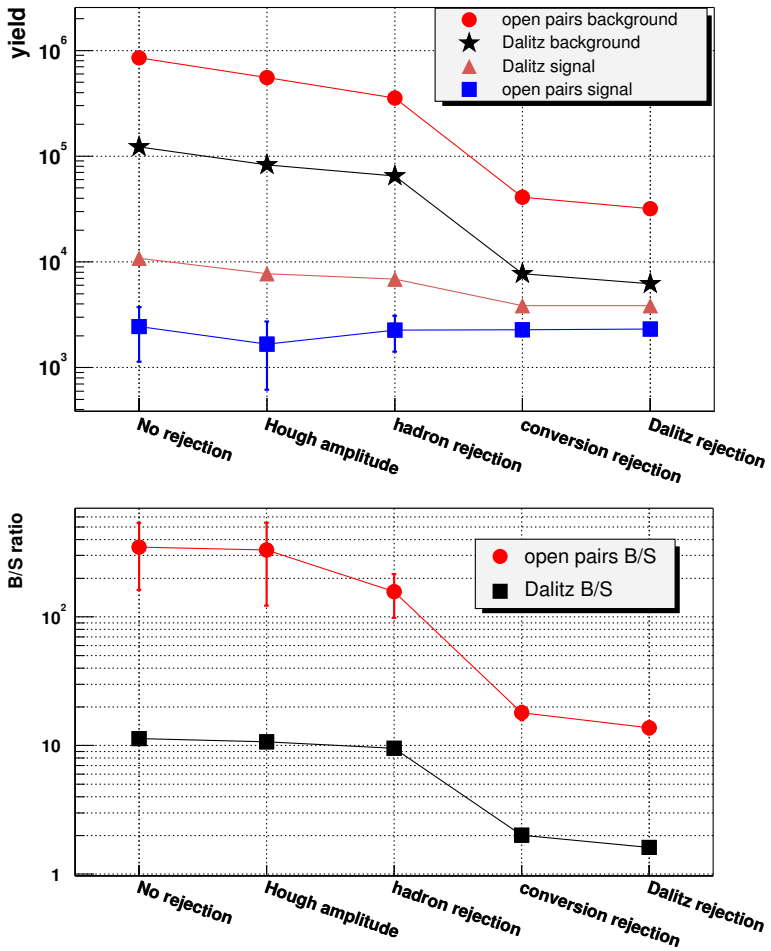

Figure 3.27: Evolution of signal and background for open pairs and π^0 Dalitz decays (top panel) with $p_T > 200\ MeV/c$ as a function of the rejection cut. Bottom panel - the same for the B/S ratio.

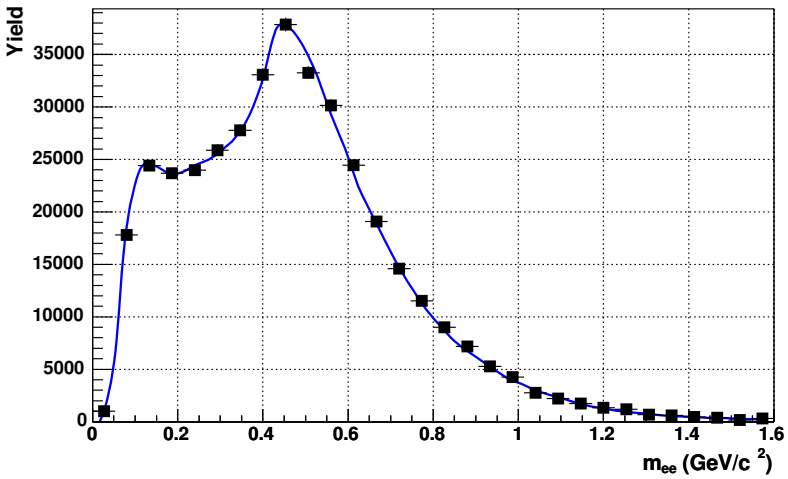

Figure 3.28: Comparison of the measured (full squares) and the generated (solid line) smooth like-sign spectra.

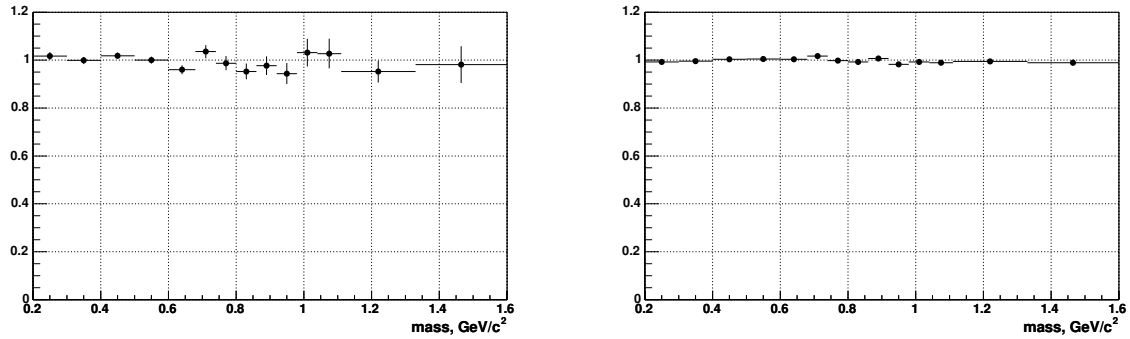

Figure 3.29: Ratio of the normalized generated background to the like-sign background. Left panel - using the sample of tracks taken at the end of the whole analysis chain. Right panel - the same using the tracks at the beginning of the analysis.

open pairs. Fig. 3.27 shows the evolution of the signal, background and B/S ratio as a function of rejection cuts for the samples of Dalitz pairs and open pairs. The various entries along the abscissa are as follows: - "no rejection" refers to the starting point right after the electron track reconstruction, when no additional background rejection is yet applied.

1. "Hough amplitude" - the θ depending Hough amplitude cut of 190 is applied.
2. "Hadron rejection" - all pion rejection cuts are applied (see section 3.4.1).
3. "Conversion rejection" - all conversion cuts are applied (see section 3.4.2).
4. "Dalitz rejection" - π^0 Dalitz rejection cuts are applied (see section 3.4.3).

The total background rejection factor achieved in the analysis is about a factor of 25. Since the number of "plus-plus" pairs $N_{e^+e^+}$ differs from the number of "minus-minus" pairs $N_{e^-e^-}$ only by 0.2% (see Table 5.1 in section 5.3), one can approximate equation (3.1) by

$$S = N_{e^+e^-} - (N_{e^+e^+} + N_{e^-e^-}) \tag{3.6}$$

and then the statistical error of the total signal is defined as

$$\Delta S = \sqrt{N_{e^+e^-} + N_{e^+e^+} + N_{e^-e^-}} \tag{3.7}$$

In the mass spectrum, the bin-to-bin error can be reduced to $\sqrt{N_{e^+e^-}}$, namely by a factor of $\approx \sqrt{2}$, using a smooth like-sign spectrum. In order to do this, pairs are generated by randomly sampling pairs of tracks from the measured single track p_T, φ and θ distributions, taken after all single track cuts of the analysis. The generated spectrum is normalized to the measured like-sign one, so that the yields of measured and smooth backgrounds are equal. Fig. 3.28 shows the comparison of the measured and the generated like-sign spectra. Same pair cuts as in the analysis are applied.

The systematic error due to subtraction of the smooth background instead of the like-sign background can be estimated as the RMS of the bin-to-bin deviations between the two backgrounds times the B/S ratio. In the left panel of Fig. 3.29 one can see

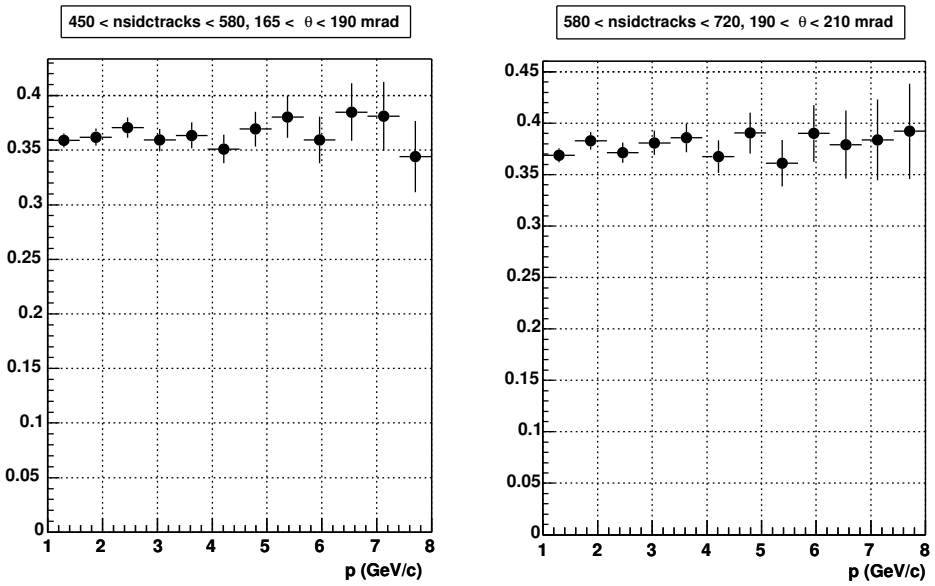

Figure 3.30: Example of the ratio of track reconstruction efficiency in 2 bins of multiplicity (represented by the number of SiDC tracks) and θ to the integral over the whole range of multiplicity and θ.

the ratio of the normalized generated background over the measured like-sign spectrum. The error bars are due to the statistical errors of the like-sign background. The RMS of the bin-to-bin deviations is 3.5%. However, these deviations reflect mainly the limited statistics of the measured like-sign spectrum, and not so much the systematics of the smooth background spectrum generation. To obtain the latter, we use the sample of tracks taken at the beginning of the analysis when the statistical errors are much smaller. The right panel of Fig. 3.29 shows the corresponding ratio of the normalized generated background over the like-sign background. We take the RMS of the deviations (equal to 0.8%) as an estimation of the systematic error in the generation of the combinatorial background, which for a $S/B = 1/19$ corresponds to a systematic error in the signal of $\approx$15%.

3.6 Pair reconstruction efficiency

The pair reconstruction efficiency is needed for the absolute normalization of the measured invariant mass spectrum. The reconstruction efficiency takes into account the inefficiencies in the track reconstruction algorithm and in the rejection cuts applied along the analysis chain. Evaluation of the reconstruction efficiency is performed using a Monte-Carlo simulation technique which requires a good knowledge of the detailed properties and defects of all detectors in the CERES spectrometer. Dilepton pairs generated by the CERES event generator (described in Chapter 4) are passed through the filter of pair opening angle cut $\Theta_{ee} > 35\ mrad$ and single track p_T cut $p_T > 200\ MeV/c$, as well as the geometrical acceptance $\eta = 2.1 - 2.65$. The accepted pairs are passed through the

CERES spectrometer using the GEANT software which generates the appropriate detector response. The resulting detector response is overlaid with real events and these events are passed through the full analysis chain. The pair reconstruction efficiency is defined as the ratio of the number of reconstructed pairs after the whole analysis chain to the initial number of overlaid events. Since the analysis is restricted to open pairs ($\Theta_{ee} > 35\ mrad$), the pair reconstruction efficiency is given by the square of the single track reconstruction efficiency.

The track reconstruction efficiency ϵ is very sensitive to the occupancy in the detectors. Higher occupancy causes a higher number of fake hits and fake matches between detectors and as a result the recognition of real tracks, as well as the background track rejection, is less effective. Detector occupancy and track density increase with the event multiplicity N_{ch} and decrease with the polar angle θ.

The track reconstruction efficiency can also depend on the particle momentum. The tracks with soft momentum ($p \lesssim 0.5-1\ GeV/c$) have a large bending angle in the magnetic field of the TPC and their reconstruction is more difficult, especially at high multiplicities. In addition, the size of the matching window strongly increases for tracks with $p \lesssim 1\ GeV/c$ and the track reconstruction is less effective as well. However these effects are not significant since the analysis is restricted to the $p_T > 200\ MeV/c$, corresponding to a momentum of about 1 GeV/c in the acceptance. This is demonstrated in Fig. 3.30 which shows the ratios of track reconstruction efficiencies as a function of momentum for two bins in multiplicity and polar angle. The ratios are flat, therefore the track reconstruction efficiency is independent of p and can be evaluated as a function of multiplicity and polar angle only.

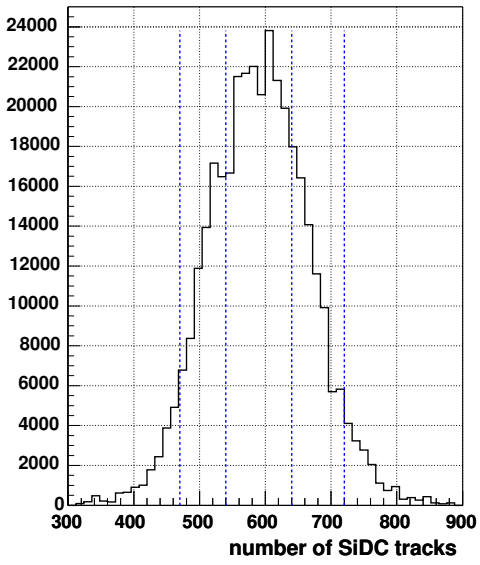

Figure 3.31: Divisions of the multiplicity distribution (represented by the number of SiDC tracks) into 5 bins.

Assuming that the multiplicity and θ dependencies of ϵ can be factorized, one can write:

$$\epsilon_{pair}(N_{ch}, \theta_1, \theta_2) = \Big[\epsilon(\theta_1) \cdot f(N_{ch})\Big] \times \Big[\epsilon(\theta_2) \cdot f(N_{ch})\Big] \tag{3.8}$$

where θ_1 and θ_2 are the polar angles of the two tracks forming a pair. $\epsilon(\theta)$ is the absolute track reconstruction efficiency as a function of θ, and $f(N_{ch})$ reflects the dependence of ϵ on multiplicity. The $\epsilon(\theta)$ and $f(N_{ch})$ are determined as follows:

- The whole range of multiplicity (characterized here by the number of SiDC tracks) is divided into 5 bins, as shown in Fig. 3.31.
- Within each multiplicity bin i, $\epsilon_i(\theta)$ is evaluated.
- Fig. 3.32 shows the ratios $\epsilon_i(\theta)/\epsilon_{(i=3)}(\theta)$. One sees, that all ratios are flat, and this justifies the factorization of $\epsilon_{pair}(N_{ch}, \theta_1, \theta_2)$ into the independent functions $\epsilon(\theta)$ and

$f(N_{ch})$.

- $\epsilon(\theta)$ is defined using the tracks from the third multiplicity bin and it is fitted and parametrized by a polynomial, as shown in the left panel of Fig. 3.33.
- The differential $f(N_{ch})$ is defined by the relative average track reconstruction efficiency in each multiplicity bin with respect to the average reconstruction efficiency in the multiplicity bin number three. $f(N_{ch})$ is plotted in the right panel of Fig. 3.33. $f(N_{ch})$ is also fitted and parametrized by a polynomial.

The average track reconstruction efficiency, integrated over multiplicity and polar angle, is 33.7%. The average pair reconstruction efficiency, given by the squared track reconstruction efficiency, is 11.4%.

There is an additional way to estimate the pair reconstruction efficiency directly from the data using the number N_0^{meas} of measured pairs with $m < 150\ MeV/c^2$. In this mass region, the two main contributions are from π^0 and η Dalitz decays:

$$N_0^{meas} = N_{\pi^0}^{meas} + N_{\eta}^{meas} = F \cdot N_0^{meas} + (1 - F) \cdot N_0^{meas} \tag{3.9}$$

where $F = 0.85$ is the fraction of π^0 Dalitz evaluated using the CERES Monte-Carlo generator (see Chapter 4). Thus, the pair reconstruction efficiency is defined simply as the ratio of measured over expected number of π^0 Dalitz pairs:

$$\epsilon_{\pi^0} = \frac{N_0^{meas} \cdot F}{N_{\pi^0}^{exp}} \tag{3.10}$$

The expected number of π^0 Dalitz pairs $N_{\pi^0}^{exp}$ can be calculated as

$$N_{\pi^0}^{exp} = N_{events} \cdot < N_{ch} > \cdot Y_{\pi^0} \tag{3.11}$$

where $< N_{ch} >= 184$ is the average charged particle multiplicity in the CERES acceptance and $Y_{\pi^0} = 0.44$ is the yield of π^0 Dalitz pairs per charged particle. Plugging this into equation (3.10) we obtain

$$\epsilon_{\pi^0} = \frac{N_0^{meas} \cdot F}{N_{events} \cdot < N_{ch} > \cdot Y_{\pi^0}} \tag{3.12}$$

The π^0 Dalitz pair reconstruction efficiency ϵ_{π^0} is 11%, in good agreement with the Monte-Carlo method estimation.

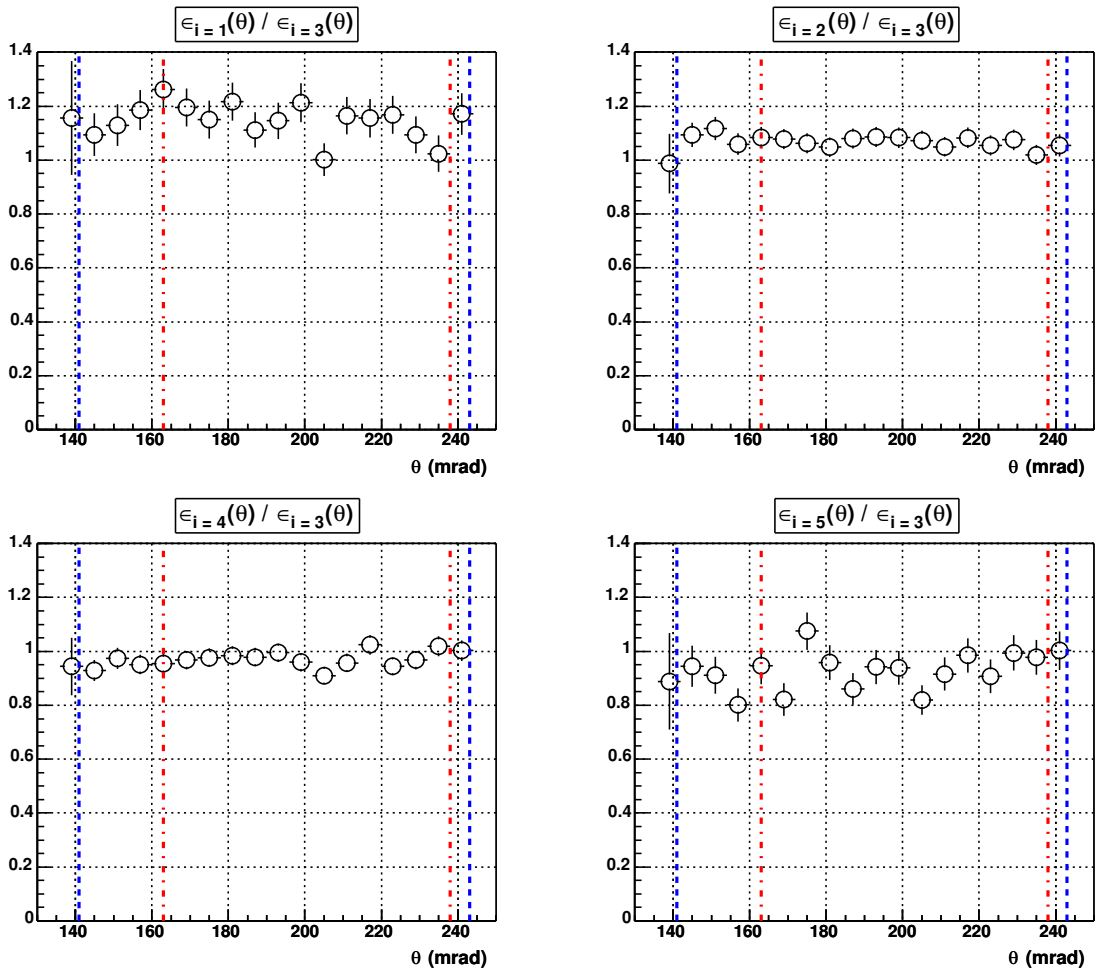

Figure 3.32: The ratios $\epsilon_i(\theta)/\epsilon_{(i=3)}(\theta)$, where i is a multiplicity bin and $\epsilon_i(\theta)$ is the reconstruction efficiency as a function of θ (see equation (3.8)).

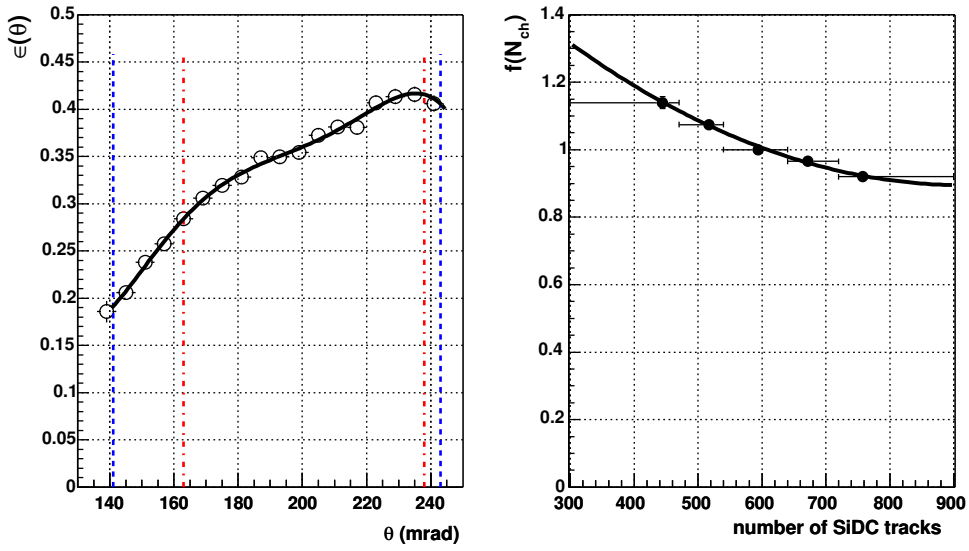

Figure 3.33: Left - track reconstruction efficiency ϵ as a function of θ, solid line is the fit with a polynomial function. Right - distribution of $< \epsilon_i >$ in 5 multiplicity bins, solid line is the corresponding fit with a polynomial.

Chapter 4

Monte-Carlo Event Generator GENESIS

The CERES event generator [48] is used to generate the e^+e^- pairs from all known meson decays in the invariant mass range covered by the CERES spectrometer. The sum of e^+e^- pairs from these decays is called the "hadronic cocktail". The cocktail provides the reference data for comparison with the measured mass spectrum on the basis of conventional sources. Deviation from the cocktail can provide evidence for the presence of a new physics source of e^+e^- pair production.

4.1 Primary particle generation

There are 7 hadronic decays producing e^+e^- pairs in the low-mass region $m_{ee} \lesssim 1GeV/c^2$, the Dalitz decays of the π^0, η, η' and ω

$$\pi^0,\ \eta,\ \eta' \rightarrow e^+e^-\gamma \qquad \omega \rightarrow e^+e^-\pi^0 \tag{4.1}$$

and the resonance decays of ρ, ω, ϕ

$$\rho,\ \omega,\ \phi \rightarrow e^+e^- \tag{4.2}$$

For each process, the number of decays per collision is calculated according to a Poisson distribution with a mean given by

$$\overline{N} = \overline{N_{\pi^0}} \cdot \frac{\sigma}{\sigma_{\pi^0}} \cdot BR \cdot S \tag{4.3}$$

where $\overline{N_{\pi^0}}$ is the mean π^0 multiplicity, used as an input parameter, σ/σ_{π^0} is the relative particle production cross section, BR is the branching ratio of the decay and S is a scale factor introduced in order to obtain enough statistics for each decay mode. Table 4.1 shows the production cross sections of the different mesons relative to π^0 taken from Pb data at the SPS. The cross sections which are not directly measured are taken from the thermal model [52], which very successfully describes particle ratios of all particles species at freeze-out with only 2 parameters (temperature $T = 170\ MeV$ and baryon

particle	σ/σ_{π^0}	**decay process**	**branching ratio**
π^0	1	$e^+e^-\gamma$	$(1.198 \pm 0.032) \times 10^{-2}$
η	0.085 [49]	$e^+e^-\gamma$	$(6.0 \pm 0.8) \times 10^{-3}$
ρ	0.094	e^+e^-	$(4.67 \pm 0.09) \times 10^{-5}$
ω	0.069	$e^+e^-\pi^0$	$(5.9 \pm 1.9) \times 10^{-4}$
ω	0.069	e^+e^-	$(7.14 \pm 0.13) \times 10^{-5}$
ϕ	0.018 [50, 51]	e^+e^-	$(2.98 \pm 0.04) \times 10^{-4}$
η'	0.0078	$e^+e^-\gamma$	$< 9 \times 10^{-4}$

Table 4.1: The relative hadron production cross sections and corresponding branching ratios implemented in the CERES generator.

chemical potential $\mu_B = 68\ MeV$). The branching ratios of the different decay processes are taken from the 2004 Particle Data Group review [53].

The π^0 rapidity distribution is approximated by a Gaussian distribution with parameters derived from a fit to the measured charged pion data of the NA49 experiment [54]. No dependence of the width of the rapidity distribution on particle mass was observed in lead-induced collisions [55], therefore the pion parametrization is also used for all other mesons.

For all mesons, except π^0, the p_T distribution is parametrized by

$$\frac{1}{m_T}\frac{dN}{dm_T} \propto e^{-\frac{m_T - m_{particle}}{T}} \quad , \quad m_T = \sqrt{p_T^2 + m_{particle}^2} \tag{4.4}$$

where the slope parameter T increases linearly with the particle mass according to $T = 0.175 + 0.115 \cdot m\ GeV$ [56]. This functional behavior of T was determined from a fit to the experimental data. The mass dependent coefficient represents the average collective flow velocity at freeze-out $< \beta_T >= 0.115$, assuming a radially expanding system [57]. For pions, the m_T distribution can not be parametrized by a single exponential. Using the measurements by NA49 [58] and WA98 [59], the m_T distribution of π^0 is approximated by two exponentials with $T_1 = 100\ MeV$ and $T_2 = 230\ MeV$. The spectrum is corrected for the soft contribution from the $\eta \to 3\pi^0$ decay by adding a third exponential term with $T_3 = 102\ MeV$ [56].

4.2 e^+e^- mass generation

e^+e^- pairs from Dalitz decays

For a Dalitz decay, $A \to Be^+e^-$, the e^+e^- pair invariant mass (m) distribution is simulated using the Kroll-Wada QED expression [60] multiplied by a form factor [61]:

$$\frac{d\sigma}{dm} = \frac{4\alpha}{3\pi}\Gamma_{\gamma\gamma}\frac{1}{m}\sqrt{1-\frac{4m_e^2}{m^2}}\left(1+\frac{2m_e^2}{m^2}\right)\left[\left(1+\frac{m^2}{m_A^2-m_B^2}\right)^2-\frac{4m_A^2m^2}{(m_A^2-m_B^2)^2}\right]^{\frac{3}{2}}\times\left|F(m^2)\right|^2 \tag{4.5}$$

where A is the parent meson, B is the daughter particle, m is the e^+e^- invariant mass and $\Gamma_{\gamma\gamma}$ is the partial width into $\gamma\gamma$. For the Dalitz decays of π^0, η and η' the daughter particle is a photon and equation (4.5) becomes:

$$\frac{d\sigma}{dm} = \frac{4\alpha}{3\pi}\Gamma_{\gamma\gamma}\frac{1}{m}\sqrt{1-\frac{4m_e^2}{m^2}}\left(1+\frac{2m_e^2}{m^2}\right)\left[1-\frac{m^2}{m_A^2}\right]^3\times\left|F(m^2)\right|^2 \tag{4.6}$$

For π^0 or η decays the form factor is parametrized using the pole approximation, according to the simplest form given by the Vector Dominance Model (VDM) [61]:

$$\left|F(m^2)\right| = \frac{1}{1-b^2m^2} \tag{4.7}$$

For ω and η' Dalitz decays, a Breit-Wigner function is used:

$$\left|F(m^2)\right| = \frac{m_V^4}{(m^2-m_V^2)^2+m_V^2\Gamma^2} \tag{4.8}$$

The functional forms and the parameters of the form factors, derived from fits to the data measured by the LEPTON-G collaboration [62], are shown in Table 4.2.

The angular distribution of the dileptons in π^0, η and η' Dalitz decays is parametrized by a $(1 + cos^2(\theta))$ distribution (θ angle is measured in the CM system of the virtual photon). For the ω Dalitz decay an isotropic θ distribution is used. A detailed discussion of the angular distribution parametrization can be found in [63].

e^+e^- pairs from resonance decays

The spectral shape of ω and ϕ mesons is parametrized by the relativistic Breit-Wigner formula

$$\frac{dR}{dm^2} = \frac{\left[1-\left(\frac{m_{th}}{m}\right)^2\right]^{\frac{3}{2}}}{(m^2-m_V^2)^2+m_V^2\Gamma_0^2} \tag{4.9}$$

where m is the invariant e^+e^- mass, $m_{th} = 3m_\pi$, m_V and Γ_0 are the vector meson mass and width parameters, respectively.

Decay	$\|F(m^2)\|^2$
$\pi^0 \to e^+e^-\gamma$	$\frac{1}{(1-b^2m^2)^2}$, $b = 5.5GeV^{-2}$
$\eta \to e^+e^-\gamma$	$\frac{1}{(1-b^2m^2)^2}$, $b = 1.9 \pm 0.4GeV^{-2}$
$\omega \to e^+e^-\pi^0$	$\frac{m_V^4}{(m^2-m_V^2)^2+m_V^2\Gamma_0^2}$, $m_V = 0.65GeV/c^2, \Gamma_0 = 0.05GeV/c^2$
$\eta' \to e^+e^-\gamma$	$\frac{m_V^4}{(m^2-m_V^2)^2+m_V^2\Gamma_0^2}$, $m_V = 0.76GeV/c^2, \Gamma_0 = 0.1GeV/c^2$

Table 4.2: Dalitz decay form factors used in the CERES generator, fitted to the measured data.

For the ρ decay this formula is not precise due to its broad width $\Gamma \sim 150MeV/c^2$. A new formalism based on the measured cross section [64, 65] of $e^+e^- \to \pi^+\pi^-$ was developed [48]. The final equation is

$$\frac{dR(m)}{dmd^3q} = \frac{\alpha^2 m_\rho^4}{3 \cdot (2\pi)^4} \frac{\left(1 - \frac{4m_\pi^2}{m^2}\right)^{\frac{3}{2}}}{(m^2 - m_\rho^2)^2 + m^2\Gamma_{tot}^2(m)} e^{-\frac{\sqrt{m^2+q^2}}{T}} \frac{m}{\sqrt{m^2+q^2}} \tag{4.10}$$

where m is the invariant e^+e^- mass, q is the 3-momentum vector of the ρ, $T = 110MeV$ is a temperature parameter and Γ_{tot} is the total ρ width.

The angular distribution of the 2 body resonance decays is assumed to be isotropic.

4.3 Hadron cocktail

The final cocktail of the hadron decays is shown in Fig. 4.1. The normalization represents the pair density per charged particle rapidity density within the CERES acceptance, as explained in section 1.4.1, where $< N_{ch} >=< dN_{ch}/d\eta > \cdot\Delta\eta$. The color lines show the individual contributions from different decays and the bold black line shows their sum. All meson yields are normalized via π^0 to the charged particle density assuming $< N_{\pi^0} > / < N_{ch} >= 0.44$ in the CERES acceptance. The mass spectrum is folded with the measured momentum resolution

$$\frac{\sigma_p}{p} = \sqrt{(0.01 \cdot p)^2 + (0.016)^2} \tag{4.11}$$

In addition, the same kinematic cuts are applied as for the data, namely

1. Pseudorapidity acceptance $2.1 < \eta < 2.65$;

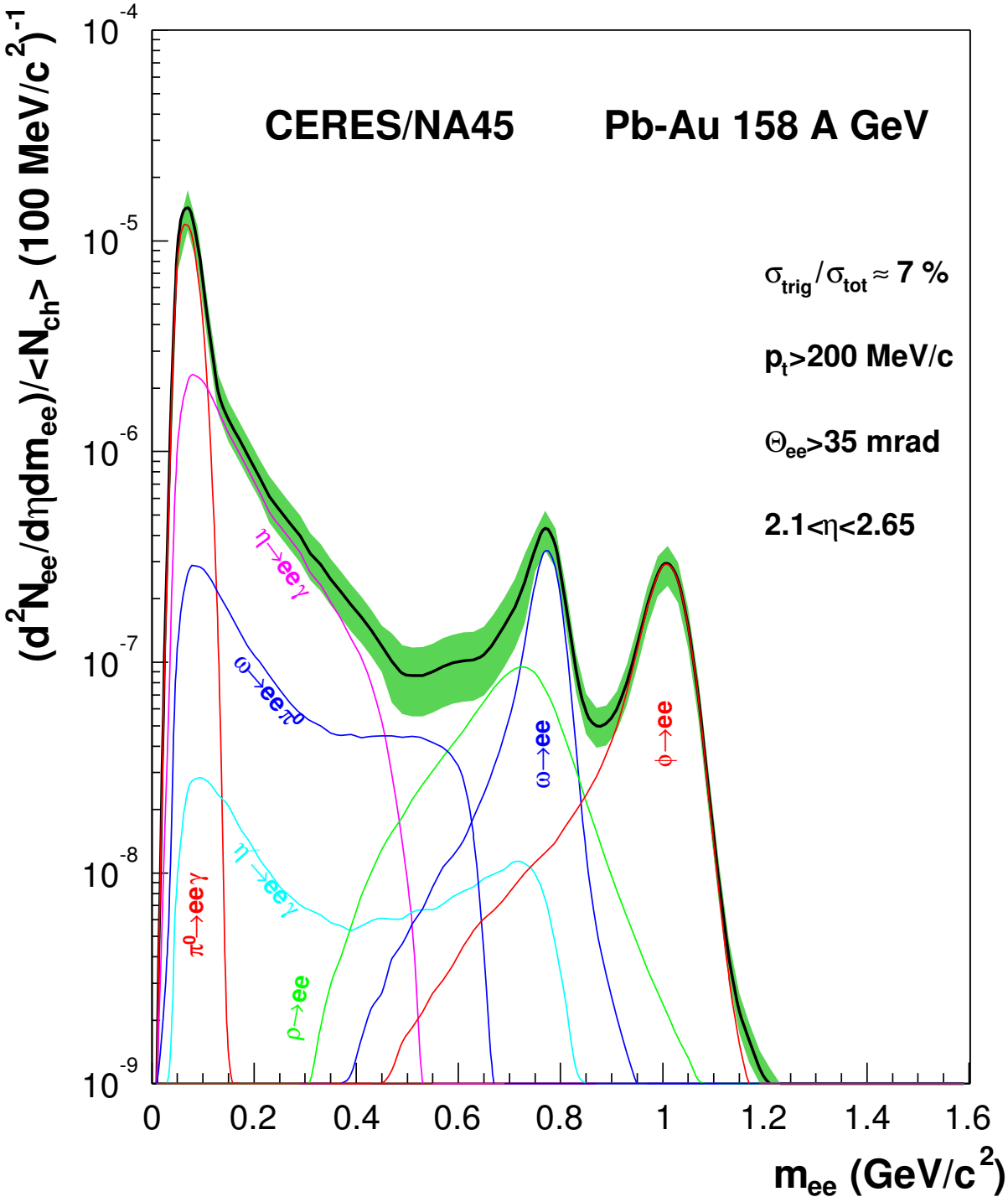

Figure 4.1: The invariant mass spectrum generated by the CERES generator for $Pb - Au$ collisions at 158 $A\ GeV$, with a single track p_T cut of 200 MeV/c. Bold black line is the sum of all contributions. The green area corresponds to the $\pm 1\sigma$ error interval.

2. Minimum pair opening angle cut of 35 $mrad$;
3. Single track p_T cut of 200 MeV/c.

The systematic errors are shown in Fig. 4.1 by the green band. These errors are discussed in detail in [14, 18]. In the low-mass region $m_{ee} < 0.2\ GeV/c^2$ the main contributions to the systematic errors come from the relative production cross section (5%), different assumptions on the p_T spectrum (5%) and rapidity distribution (3%), resulting in a total systematic error of 8%. In the high-mass region $m_{ee} > 0.2\ GeV/c^2$ the errors are dominated by uncertainties in the relative production cross section, branching ratios and form factors. The errors in the relative production cross sections are estimated either by the measured particle ratios, or by the uncertainties in the statistical model predictions. The overall error is 20%. The errors originating in the branching ratios and form factors depend on the mass region. Their contributions are as following:

- for $m < 0.45\ GeV/c^2$ the error is dominated by the branching ratio of the η Dalitz decay (13%).
- for $0.45 < m < 0.75\ GeV/c^2$ the error in ω Dalitz branching ratio is dominant (30%).
- for $m > 0.75\ GeV/c^2$ the error is dominated by the branching ratios of vector mesons (6%).

The total systematic error in the high-mass region is on the average 30%.

The integral yield of electron pairs per charged particle in the CERES acceptance given by the generator and after applying all kinematic cuts is:

$$\frac{1}{< N_{ch} >} \cdot \frac{d^2N_{ee}}{dmd\eta} = \begin{cases} (8.34 \pm 0.67) \times 10^{-6} & for\ m < 0.2\ GeV/c^2, \\ (2.0 \pm 0.6) \quad \times 10^{-6} & for\ m \geqslant 0.2\ GeV/c^2. \end{cases} \tag{4.12}$$

Chapter 5

Physics results

5.1 Absolute normalization of the data

The CERES data is normalized to represent the pair density per charged particle within the CERES acceptance of $2.1 < \eta < 2.65$:

$$\frac{d^2N_{ee}}{d\eta dm_{ee}} \cdot \frac{1}{< N_{ch} >} = \frac{1}{N_{events}} \cdot \frac{1}{< dN_{ch}/d\eta >} \cdot \frac{1}{\Delta\eta} \cdot \sum \frac{1}{\epsilon_1^i \cdot \epsilon_2^i} \tag{5.1}$$

where

- N_{events} is total number of events, which is 17,394,927;
- $< dN_{ch}/d\eta >= 334 \pm 34.7$ is the average charged particle rapidity density for the 7% most central events;
- $\Delta\eta = 0.55$ is the CERES fiducial acceptance;
- $< N_{ch} >=< dN_{ch}/d\eta > \cdot\Delta\eta$ is the average charged particle multiplicity in the CERES acceptance;
- ϵ_1^i and ϵ_2^i are track reconstruction efficiencies.

5.2 Stability of results

The values of the cuts described in Chapter 3 can not be determined with a good precision. For each cut there is a range of reasonable values. To check the stability of the physics results as a function of the cut values, each cut was randomly varied within a band of a typical width of 5-10%. A total of 500 random sets of cuts were applied to the data set. Fig. 5.1 shows the results of the procedure in terms of the signal S of open pairs and Dalitz pairs, pair reconstruction efficiency ϵ and ratio S/ϵ^2. As expected, the results cluster around a line passing through the origin (solid line in the top panels). The spread of the points around this line is taken as a measure of the systematic uncertainties in the analysis procedure. More precisely, the distribution of S/ϵ^2 is fitted with a gaussian, and its width is taken as the 1σ systematic error of the analysis procedure. For open pairs, the error is 9% and for the Dalitz pairs ($m < 200\ MeV/c^2$) the error is 4.3%. Naturally, for

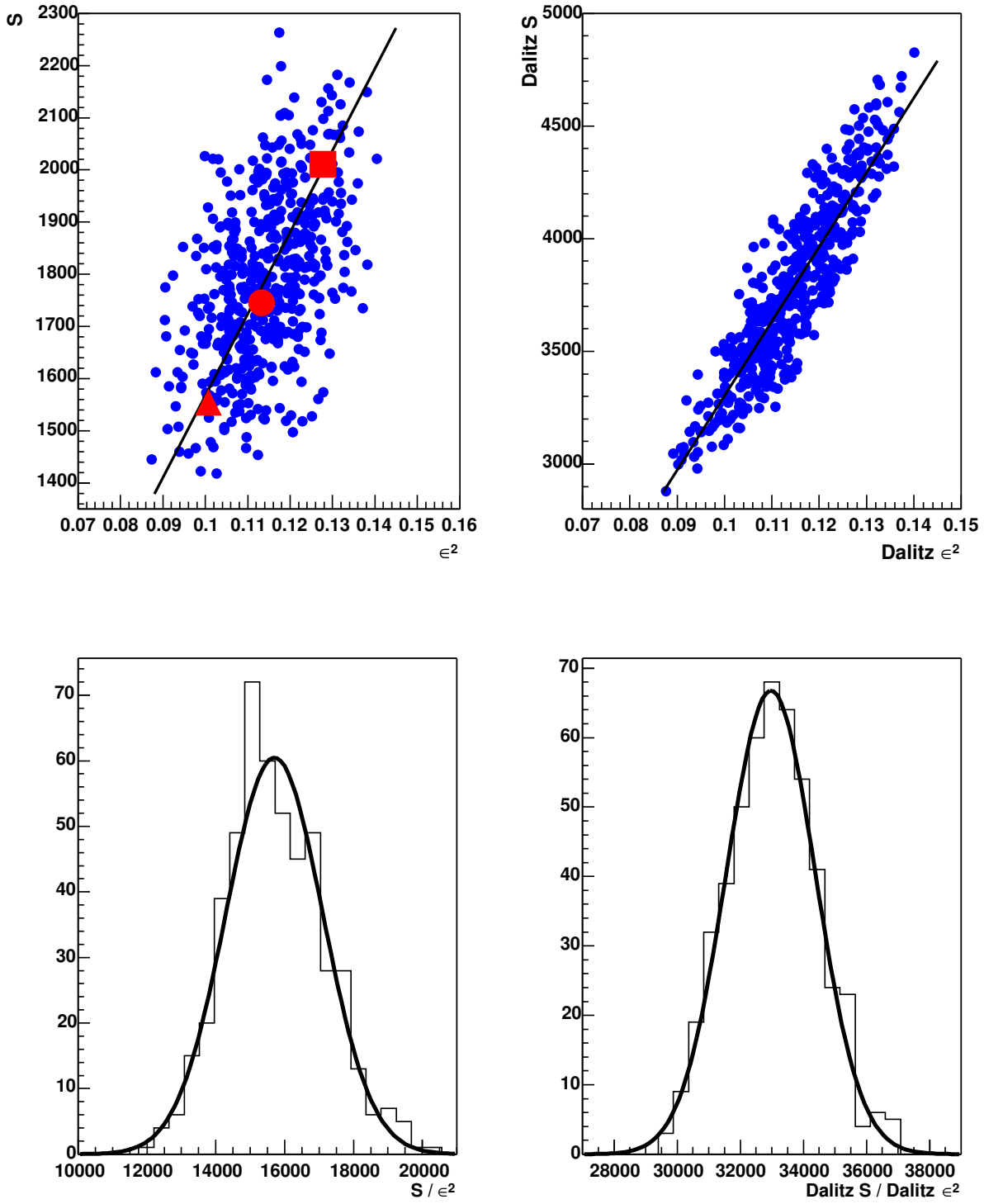

Figure 5.1: Random variation of all cuts within defined limits. The signal S versus pair reconstruction efficiency ϵ^2 is shown in the top left (open pairs) and top right (Dalitz, or $m < 0.2\ GeV/c^2$ pairs) panels. Distributions of S/ϵ^2 ratios for open pairs (bottom left) and Dalitz pairs (bottom right) are fitted with a gaussian in order to define the systematic error of the analysis procedure. The red dots shows the position corresponding to the set of cuts chosen for the final results. The red triangle and red square are the positions of two additional sets of cuts used for the discussion on the stability of the shape of mass spectrum.

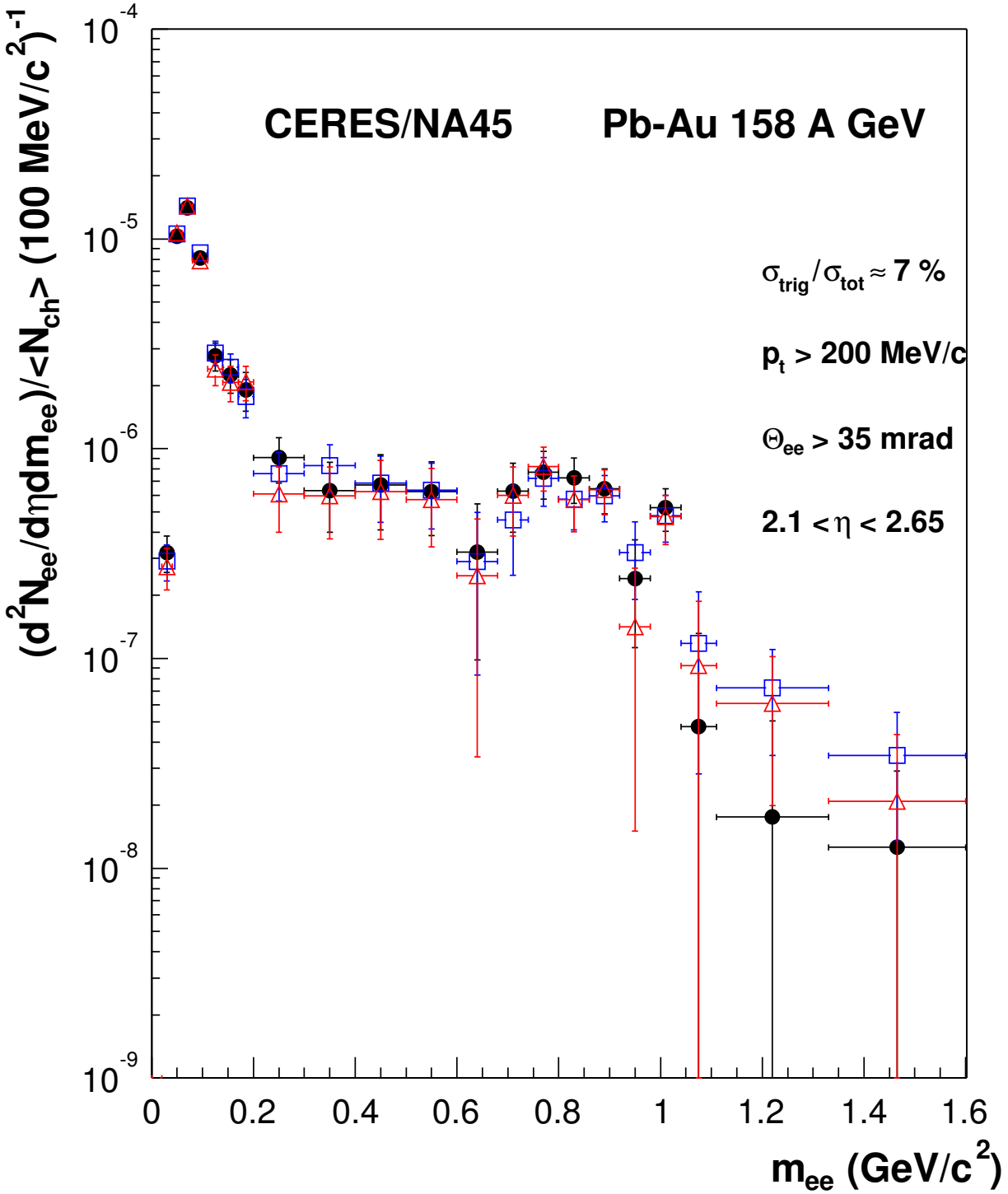

Figure 5.2: Comparison of the final invariant mass spectrum of e^+e^- pairs with two other spectra having very low and very high track reconstruction efficiency with respect to the final one. Black dots correspond to the final spectrum; blue squares corresponds to the spectrum with high efficiency (red square on the top left panel in Fig. 5.1); red triangle corresponds to the spectrum with low efficiency (red triangle on the top left panel in Fig. 5.1).

Mass range, GeV/c^2	$N_{+\,-}$	$N_{+\,+}$	$N_{-\,-}$	S	S/B ratio	S_{eff}
$m_{ee} < 0.2$	9696	3103	3122	3471 ± 126	1/1.79	758
$m_{ee} > 0.2$	34225	16258	16220	1747 ± 258	1/18.6	46

Table 5.1: Yield of e^+e^- pairs, S/B ratio and effective signal in different mass regions, with a single track $p_T > 200\ MeV/c$.

the final results the set of cuts corresponding to the center of the S versus ϵ^2 distribution is chosen. Its position is shown in the top left panel of Fig. 5.1 by the red dot.

To check the stability of the shape of mass spectrum, the final invariant mass spectrum is overlaid with two other spectra, corresponding to the extreme cases of very high and very low reconstruction efficiency. These two choices are indicated by the red square and red triangle in Fig. 5.1 (top left panel). The spectra are chosen so, that their S/ϵ^2 ratios and the one of the final mass spectrum are approximately the same. In other words, the three choices lay on the straight line passing through the origin. Fig. 5.2 shows the overlay of the three spectra. One sees that the spectra are in a very good agreement, although the difference in reconstruction efficiency between the two extreme cases is about 30%.

5.3 Mass spectrum

The total number of e^+e^- pairs in different mass ranges is given in Table 5.1. The error of the signal S is calculated using equation (3.7), since the charge asymmetry is on the level of a few promils only. The last column of the table shows the effective signal

$$S_{eff} = \frac{S^2}{S + 2 \cdot B} \approx \frac{S^2}{2 \cdot B} \tag{5.2}$$

which is the background-free equivalent of S. The resulting invariant mass spectrum is displayed in Fig. 5.3. Smooth like-sign background for the background subtraction is used. The expected contributions from the known hadron decays obtained by the GENESIS Monte-Carlo event generator are shown by solid lines in different colors. The statistical errors are given by the vertical bars. The 1σ systematic errors are shown by the square brackets in the data points and the green band in the generator cocktail.

The comparison of the data to the hadronic cocktail, shows that at low masses $m < 200\ MeV/c^2$ the measured spectrum is in good agreement with the predictions from known hadron sources, as it was observed in all CERES measurements. For masses above $200\ MeV/c^2$ an enhancement of the measured yield over the expectation from the known hadron sources is observed. The enhancement extends all the way into the higher masses. The shape of the enhancement is almost structureless in the mass range $m = 0.2 - 0.6\ GeV/c^2$. The ϕ meson peak is seen, and there is a very broad structure around the ρ/ω region. Most of the enhancement is observed around the mass interval of $0.3 - 0.6\ GeV/c^2$. The explanation of these results require an additional source of

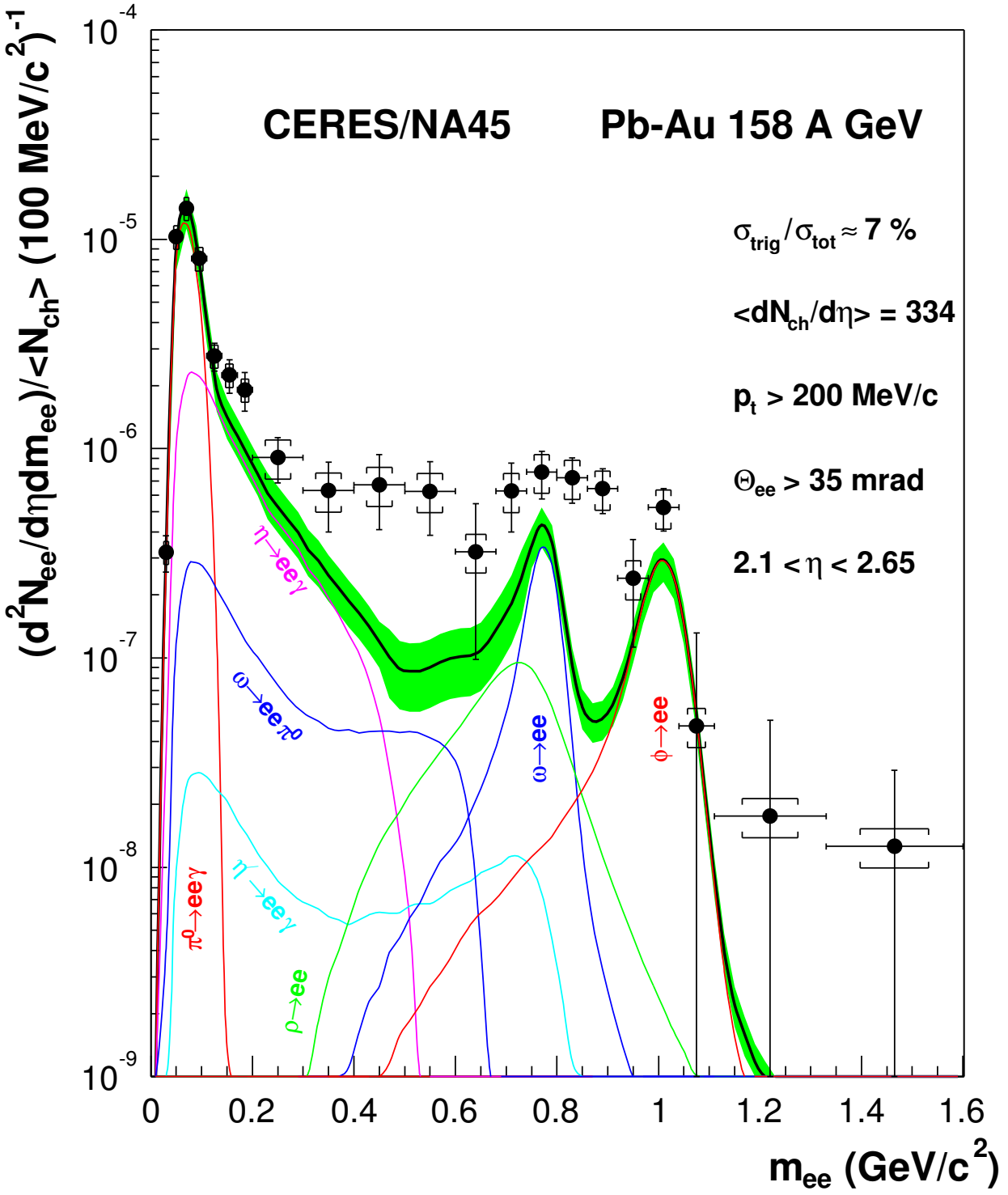

Figure 5.3: Inclusive mass spectrum of e^+e^- pairs produced in $Pb-Au$ collisions at 158 $A\,GeV$ with a single track p_T cut of 200 MeV/c. The black solid line represents the sum of the contributions from known hadron sources. Statistical errors are shown by vertical bars. 1σ systematic errors are shown by square brackets. The green band corresponds to the $\pm 1\sigma$ cocktail error interval.

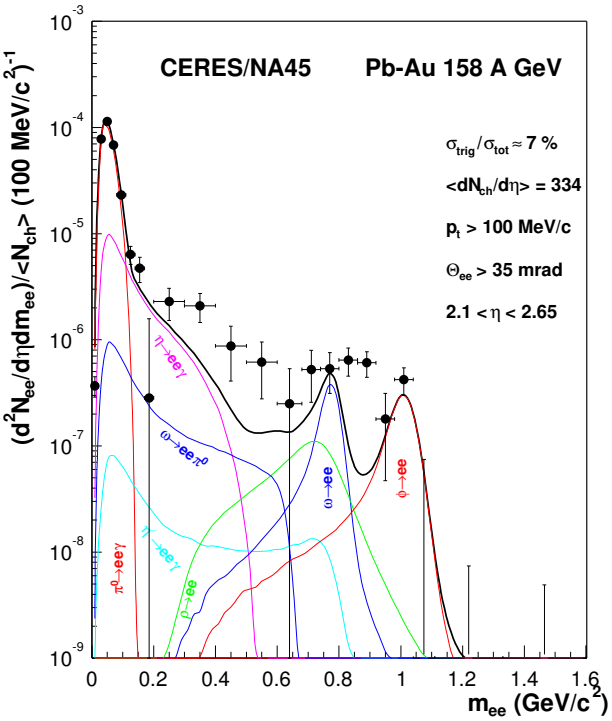

Figure 5.4: Inclusive mass spectrum of e^+e^- pairs produced in $Pb-Au$ collisions at 158 $A\,GeV$ with a single track p_T cut of 100 MeV/c. The black solid line represents the sum of the contributions from known hadron sources. Statistical errors are shown by vertical bars.

dilepton pair emission, not included in the hadronic cocktail. Possible theoretical models for explanation of the enhancement will be discussed in section 5.7.

To quantify the excess of the data, the enhancement factor F is defined as the ratio of the measured over the calculated yield from the hadronic cocktail. For masses above 200 MeV/c^2, $F = 2.9 \pm 0.32(stat.) \pm 0.44(syst.) \pm 0.87(decays)$, which is in good agreement with the results obtained in the combined analysis of the 1995/1996 data which was triggered on a lower centrality of 30% of the geometrical cross-section [18]. The dependence of F on centrality will be discussed in section 5.5.

The upgrade with the TPC made possible the reconstruction of tracks with p_T below 200 MeV/c which was the minimum limit of CERES in the previous runs. Monte-Carlo simulations show that tracks with $p_T > 100$ MeV/c can be reconstructed in the TPC. This offers the possibility of examining the invariant mass spectrum with a single track p_T cut of 100 MeV/c. However, the p_T cut is a very strong tool for the rejection of the combinatorial background. By decreasing the p_T cut to 100 MeV/c we unavoidably get a higher B/S ratio. The invariant mass spectrum with $p_T > 100$ MeV/c is shown in the Fig. 5.4, and the corresponding numbers of e^+e^- pairs in different mass intervals are given in the Table 5.2. As expected, the B/S is much higher than in the case with

Mass range, GeV/c^2	$N_{+\,-}$	$N_{+\,+}$	$N_{-\,-}$	S	S/B ratio	S_{eff}
$m_{ee} < 0.2$	98219	37242	38407	22578 ± 416	1/3.35	2932
$m_{ee} > 0.2$	151035	74063	74541	2431 ± 547	1/61.1	20

Table 5.2: Yield of e^+e^- pairs, S/B ratio and effective signal in different mass regions, with a single track $p_T > 100\ MeV/c$.

$p_T > 200\ MeV/c$. For the open pairs it reaches the value of 61.1, (the background is 4.5 times larger, while the signal is larger by only 40%). The enhancement factor for $m > 0.2\ GeV/c^2$ is $2.35 \pm 0.37(stat.)$, which is within the errors consistent with the analysis with $p_T > 200\ MeV/c$. The shape of the enhancement also follows the same behavior of the one obtained with $p_T > 200\ MeV/c$, *i.e.* the enhancement starts around the mass of 200 MeV/c^2 and it extends into the whole range of higher masses.

5.4 Systematic errors

The systematic error on the data points has three main contributions:

1. The error of the analysis method. It was discussed in detail in section 5.2. This error is 4.3% for $m < 200\ MeV/c^2$ and 9% for $m > 200\ MeV/c^2$.
2. The error of $< dN_{ch}/d\eta >$, which is used for the normalization of the data. It is estimated to be 12%.
3. The error following from the deviations between the measured and the smooth background. It was discussed in detail in section 3.5 and evaluated as 15%.

All these errors are uncorrelated, therefore they are added quadratically and the final error is 13% for $m < 200\ MeV/c^2$ and 20% for $m > 200\ MeV/c^2$.

For the systematic error of the enhancement factor only the first two contributions are relevant, since the smooth background is normalized so that its integral is equal to the yield of the like-sign pairs. This results in the final error of 15% for the mass interval $m > 200\ MeV/c^2$. For masses $m > 200\ MeV/c^2$ there is an additional systematic error of ∼30% that comes from the uncertainties in the hadronic cocktail (see section 4.3).

5.5 Multiplicity dependence of the enhancement factor

The dependence of the yield of e^+e^- pair production on the event multiplicity can give us certain clues on the origin of dilepton production. The multiplicity distribution measured

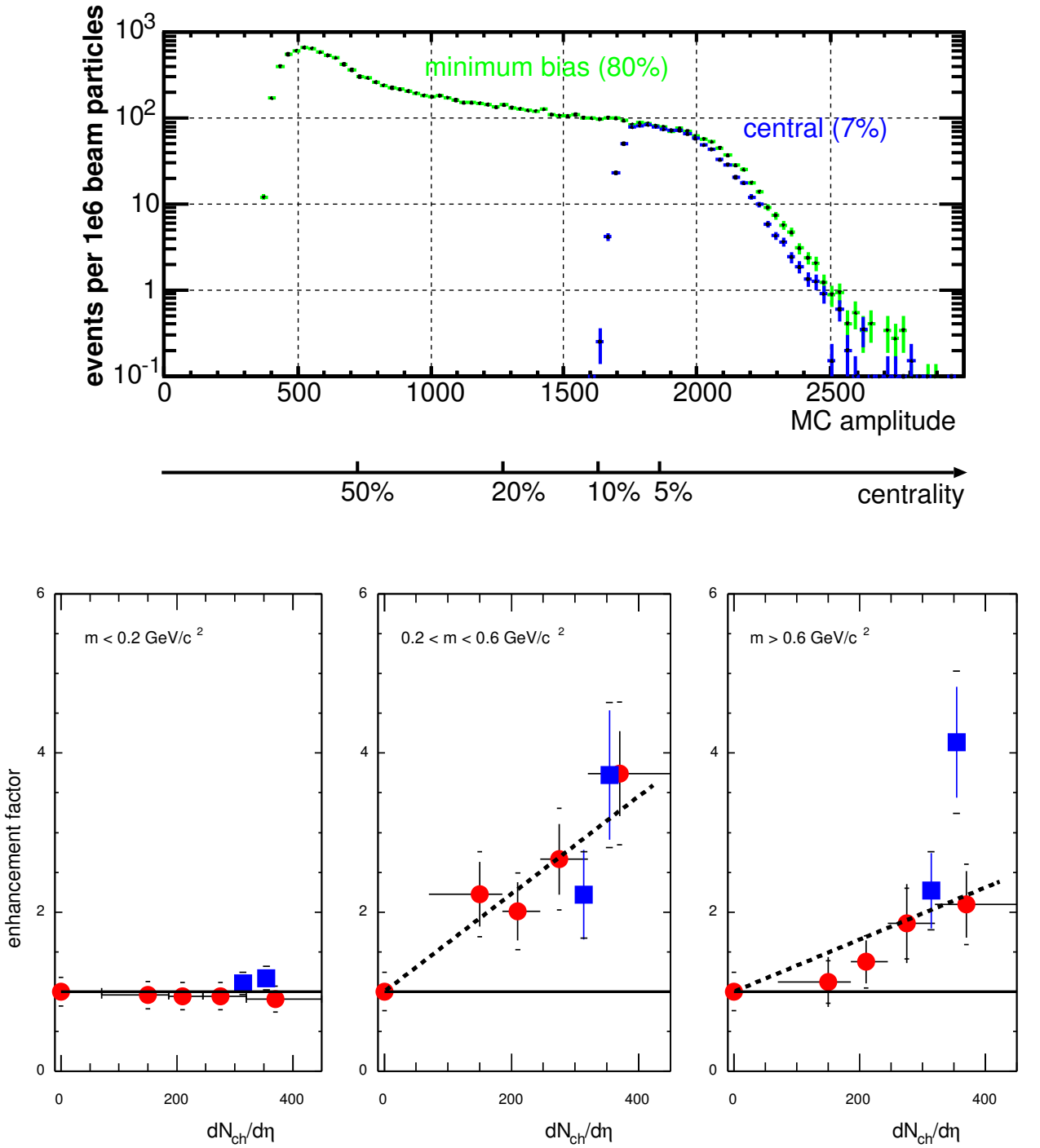

Figure 5.5: Top panel: multiplicity distribution of the event sample used in the present analysis. Centrality is represented as a percentile of the total geometrical cross section and also as a function of the multiplicity counter (MC) amplitude. Bottom panel: enhancement factor as a function of the event multiplicity. Red dots - data from the combined analysis of the 1995/96 data. Blue squares - data from the present analysis. The present data set is divided in two centrality bins: 0-3% and 3-7%. Statistical errors are shown by vertical bars. 1σ systematic errors are shown by the horizontal bars. Dotted lines show the fit of all experimental points assuming quadratic scaling of the electron yield (linear scaling of enhancement factor) with event multiplicity.

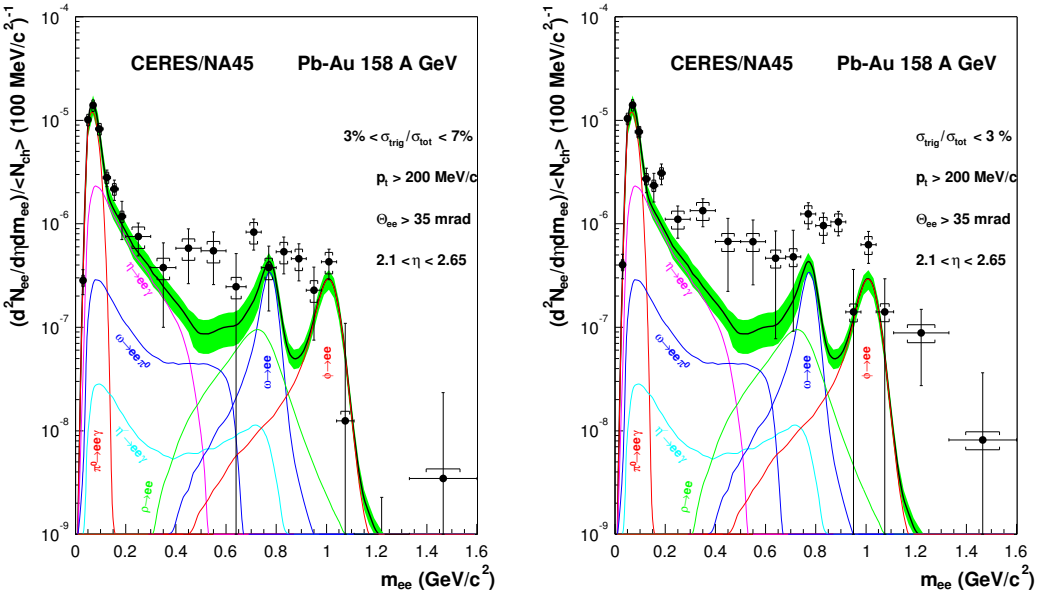

Figure 5.6: Inclusive e^+e^- invariant mass spectra in two centrality bins.

in the interval $2 < \eta < 3$ and corrected for pile-up and reconstruction efficiency is shown in the top panel of Fig. 5.5. Due to the high centrality selected by the trigger it is possible to divide the multiplicity range only into two bins: 0-3% and 3-7%. The bottom panel of Fig. 5.5 shows the enhancement factor F as a function of $dN_{ch}/d\eta$ integrated over three mass ranges: $m < 0.2\ GeV/c^2$, $0.2 < m < 0.6\ GeV/c^2$ and $m > 0.6\ GeV/c^2$. The present data is overlaid with the results of the combined analysis of 1995/96.

If the dilepton pair production is dominated by hadron decays, then the enhancement factor should follow the horizontal line at 1. Such a behavior is observed only in the lowest mass range $m < 0.2\ GeV/c^2$, dominated by π^0 Dalitz decays. For higher masses, a stronger than linear increase of F with the event multiplicity is clearly visible. In the intermediate mass region $200 < m < 600\ MeV/c^2$, F reaches the highest value of 3.7 for the most central events. For the high mass range $m > 600\ MeV/c^2$, the maximum value of F is 4.1. The rate of thermal radiation from $q\bar{q}$ or $\pi^+\pi^-$ annihilation is expected to have a quadratic dependence on $dN_{ch}/d\eta$, since it is proportional to the product of particle and anti-particle densities. In the bottom panel of Fig. 5.5 we also show the fit of the experimental points from this analysis together with the combined analysis of 1995/96 assuming a quadratic dependence of the electron pair yield (*i.e.* a linear dependence of F) on $dN_{ch}/d\eta$. Both statistical and systematic errors are relatively large, and the maximum deviation between the present data and the quadratic dependence fit or the combined 1995/96 data are within 1σ only. The confidence level of the fit is 68% for masses $0.2 < m < 0.6\ GeV/c^2$ and 8.6% for masses $m > 0.6\ GeV/c^2$. For the case of linear scaling of the yield (on F constant) the confidence level of the fit in both mass intervals is almost 0. Thus, the assumption that the enhancement factor scales stronger

than linearly with $dN_{ch}/d\eta$ is also supported by the fit results.

The change in the spectral shape in the two centrality bins is illustrated in Fig. 5.6. The enhancement factor in the lower centrality bin is $F = 2.2 \pm 0.38(stat.) \pm 0.39(syst.) \pm 0.66(decays)$ and in the higher centrality bin is $F = 3.9 \pm 0.55(stat.) \pm 0.50(syst.) \pm 1.17(decays)$. The enhancement is more pronounced in the whole mass region $m > 0.2\ GeV/c^2$, although the strongest increase in the enhancement seems to be in the mass range $300 - 400\ MeV/c^2$, *i.e.* between π^0/η Dalitz decays and the ρ peak.

5.6 Transverse momentum dependence

Fig. 5.7 shows the pair transverse momentum distribution in 2 mass ranges: the low-mass $m < 0.2\ GeV/c^2$ pairs (top panel) and the high-mass $0.2\ GeV/c^2 < m < 1.5\ GeV/c^2$ pairs (bottom panel). The low-mass distribution, dominated by the π^0 and η Dalitz decays agrees with the prediction. For the high masses the enhancement is observed over the whole p_T range but it is more pronounced at low pair p_T.

The invariant mass spectra in two pair-pt intervals are shown in Fig. 5.8: the mass spectrum with $p_T^{ee} < 500\ MeV/c$ is on the left panel and the mass spectrum with $p_T^{ee} > 500\ MeV/c$ is on the right panel. The most pronounced difference between the two cases is in the mass range $200\ MeV/c^2 < m < 600\ MeV/c^2$. The corresponding enhancement factors are $4.05 \pm 1.60(stat.) \pm 0.61(syst.)$ and $2.42 \pm 0.38(stat.) \pm 0.36(syst.)$, *i.e.* the enhancement for dilepton pairs with $p_T^{ee} < 500\ MeV/c$ is higher by 67%. The strong decrease of the measured yield of dileptons with $p_T^{ee} < 500\ MeV/c$ below masses of $400\ MeV/c^2$ is due to the single track p_T cut ($p_T > 200\ MeV/c$) on the pair acceptance. The conclusion from these results is that the enhancement of dilepton production is more pronounced in the soft pair p_T region.

5.7 Comparison to theoretical models

Fig. 5.9 compares the results of this analysis to a few theoretical models. All of them include the $\pi^+\pi^-$ annihilation channel (thermal radiation from a hot and dense hadronic system) proceeding through an intermediate ρ meson:

$$\pi^+\pi^- \rightarrow \rho \rightarrow \gamma^* \rightarrow e^+e^- \tag{5.3}$$

The models treat the ρ spectral function in a different manner. The first model (shown by the dotted line) uses the unmodified, or vacuum ρ spectral function. This increases the dilepton yield around the ρ mass, but it is not able to explain the enhancement of dileptons at lower masses. Two other models assume in-medium modification of the ρ spectral function: the dashed line represents a calculation based on the collision broadening of the spectral function [34, 35] and the dashed-dotted line line is the result of a calculation by R. Rapp with a dropping ρ mass following the Brown-Rho scaling [29, 66, 67]. The current implementation of these models gives quite different predictions in the region

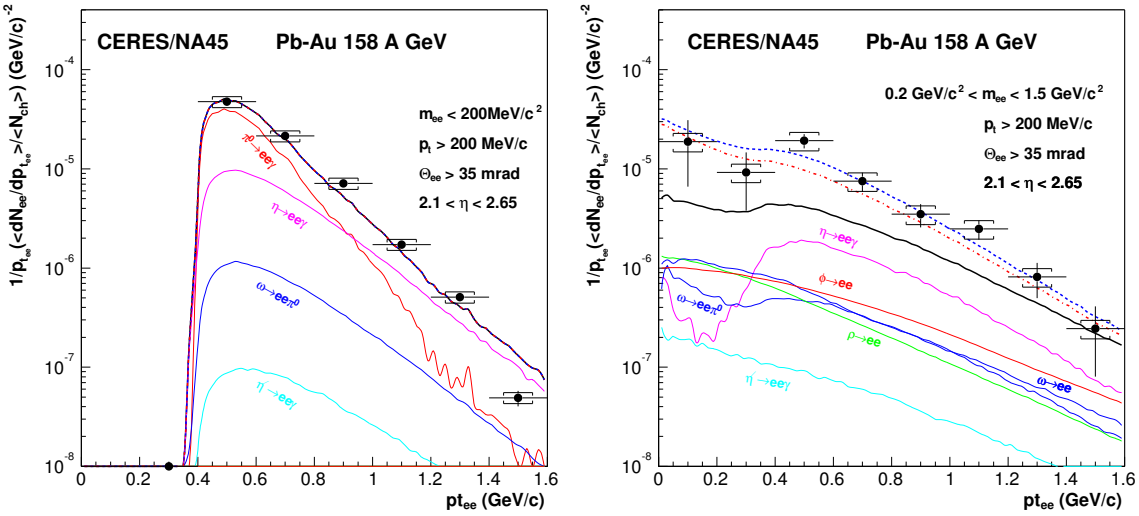

Figure 5.7: Pair transverse momentum spectra with single track $p_T > 200\ MeV/c$ and with contributions from known hadron sources. Left: low-mass pairs with $m < 0.2\ GeV/c^2$. Right: high-mass pairs with $0.2\ GeV/c^2 < m < 1.5\ GeV/c^2$. Full black line shows the total spectrum from the cocktail of known hadron sources. Cyan and pink lines above the cocktail contribution are theoretical calculations using the Brown-Rho scaling and the broadening of the ρ-meson spectral shape, respectively. Statistical errors are shown by vertical bars. 1σ systematic errors are shown by square brackets.

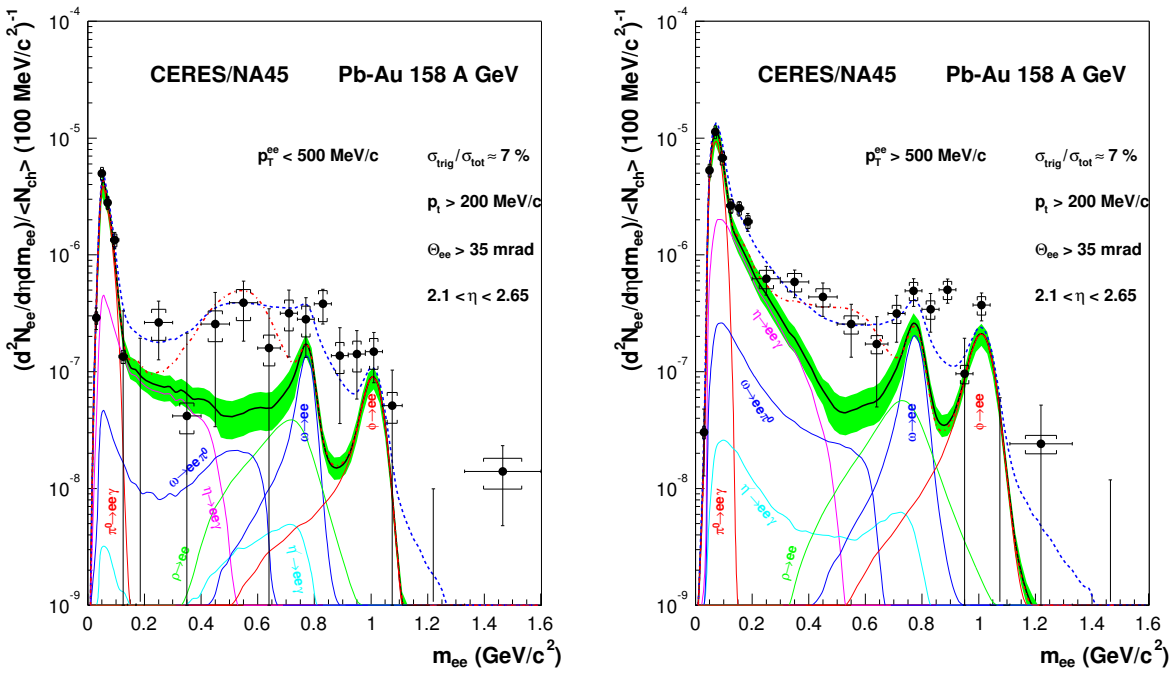

Figure 5.8: Inclusive e^+e^- invariant mass spectra with pair-pt cut: $p_T^{ee} < 500\ MeV/c$ (left) and $p_T^{ee} > 500\ MeV/c$ (right). Full black line shows the sum of the contributions from known hadron sources. Red dashed-dotted line is the theoretical calculation using the Brown-Rho scaling; blue dashed line is the theoretical calculation using the broadening of the ρ-meson spectral shape.

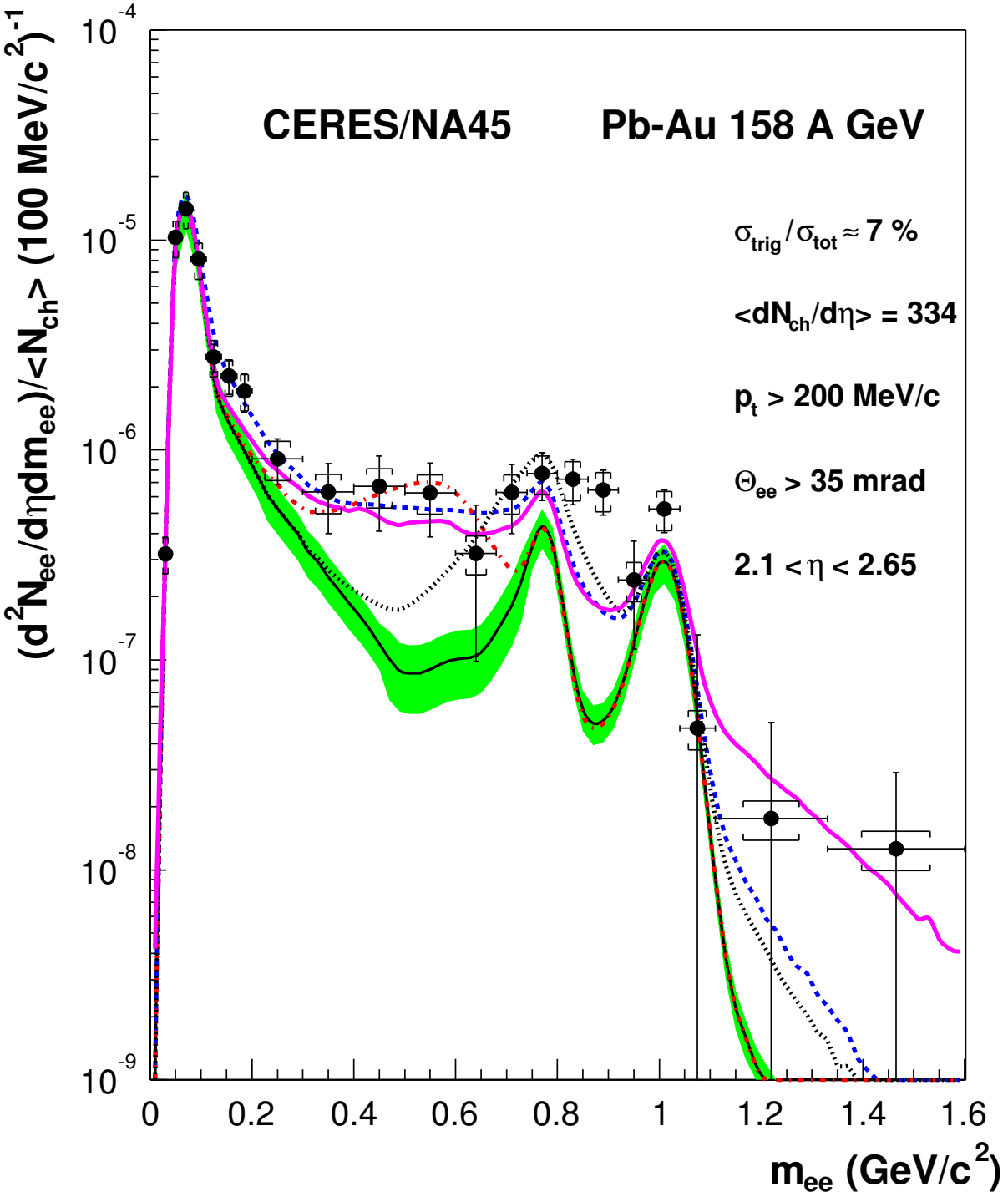

Figure 5.9: Comparison of the CERES results to different theoretical models invoking modification of ρ spectral function: black dotted line - vacuum ρ, blue dashed line - in-medium modifications of ρ, red dashed-dotted line - dropping ρ mass using Brown-Rho scaling. Purple solid line - the yield from thermal model by Kämpfer.

between the ω and the ϕ meson peaks. In the collision broadening scenario, the strength is distributed both above and below the ρ meson, whereas in the dropping mass scenario the strength is shifted to lower masses only. This creates a large difference in the expected yield of dileptons in the $\omega - \phi$ region between the two models. A pronounced minimum at $m \approx 0.85\ GeV/c^2$ is predicted in the dropping ρ mass case with a factor of almost 4 difference with the collision broadening curve. Such a minimum is not seen in the data. Thus, in the mass region between the ω and ϕ, the data favor the collision broadening scenario. The differences in the predictions of the models outside the $\omega - \phi$ region are small and the precision of the data does not allow discrimination between them. A similar situation is observed in Fig. 5.8, showing the invariant mass spectra with two pair-pt cuts. In the pair-pt spectra, shown in Fig. 5.7, both models generate very close predictions, and the data do not provide further the discrimination between them.

Another theoretical model was developed by Kämpfer *et al.* [68, 69]. This model proposes a unique parametrization of thermal dilepton and photon yields. For a system with a temperature close to the critical temperature for the deconfinement phase transition, the dilepton emission rates from either hadronic ($\pi^+\pi^-$ annihilation) or deconfined matter ($q\bar{q}$ annihilation) are similar [70, 71]. This similitude is interpreted as a manifestation of quark-hadron duality. The modified ρ spectral function in $\pi^+\pi^-$ annihilation leads to a strong broadening of the ρ peak, so that the total dilepton spectrum is similar to the one produced by the lowest-order $q\bar{q}$ annihilation [72], which was originally parametrized by a Boltzmann approximation [68]:

$$\frac{dN}{d^4Q} \propto N_{eff} \cdot e^{-\frac{Q \cdot u}{T_{eff}}} \tag{5.4}$$

where Q is the dilepton 4-momentum, u is 4-velocity of the medium, T_{eff} is the effective temperature averaged over the full space-time and N_{eff} is the normalization factor reflecting the effects of the chemical potential μ. Kämpfer uses therefore the $q\bar{q}$ annihilation rate irrespectively of whether the system is or not in a deconfined state. The result of the calculation of the dilepton yield using this model with $T_{eff} = 170\ MeV$ on top of the hadron decays (CERES cocktail) is shown in Fig. 5.9 by the purple solid line. This model yields results which are very similar to the predictions of the in-medium broadening of the ρ meson.

5.8 Summary and Outlook

The final CERES measurements, described in this thesis, were performed using the spectrometer upgraded with the new detector, the radial TPC. The analysis was based on a completely new tracking strategy. The momentum of the charged particles was measured using the radial magnetic field of the TPC, and not by deflection in the magnetic field between the two RICH counters. The results presented in this thesis confirm the results obtained in the combined analysis of 1995/96 data [18]. The shape of the invariant mass spectrum and the magnitude of the enhancement of dilepton pair production are similar.

The enhancement factor demonstrates a stronger than linear dependence on the multiplicity. The pair p_T spectra show that the dilepton yield is enhanced over the entire range for masses $m > 0.2\ GeV/c^2$, but it is more pronounced at low pair p_T ($p_T^{ee} < 500\ MeV/c$). Possible theoretical explanations of the results have been considered. The enhancement is interpreted as evidence for thermal radiation ($\pi^+\pi^-$ annihilation) from a hot and dense hadronic system. With the improved mass resolution of the upgraded spectrometer, the data favor the scenario of in-medium broadening of the ρ meson and could hint that the approach to chiral symmetry restoration proceeds by the broadening and subsequent melting of the resonances rather than by dropping masses.

To provide a more convincing evidence, more experimental results are needed. The preliminary results of the NA60 experiment [73] with significantly improved conditions (much higher statistics and better mass resolution) seem to point out into the same direction, ruling out the Brown-Rho scenario, although a strong debate is ongoing [74] on the interpretation of the NA60 results. More measurements of low-mass e^+e^- pairs are expected from the PHENIX experiment at RHIC. With its excellent mass resolution of about 1% around the ϕ mass, and the upcoming upgrade with a Hadron-Blind detector [75, 76], PHENIX is expected to perform high quality measurement of low-mass pairs.

Bibliography

[1] A. Cherlin and S. Yourevich (CERES collaboration) J. Phys. G 30 (2004) S1007.

[2] F. Karsch Lect. Notes Phys. **583** (2002) 209., hep-lat/0106019.

[3] C. R. Allton *et al.* Nucl.Phys. Proc. Suppl. **141** (2005) 186.

[4] C. Adami and G. E. Brown Phys. Rep. **224** (1993) 1.

[5] K. Rajagopal and F. Wilczek, hep-ph/0011333.

[6] R. Rapp, T. Shafer, E. Shuryak and M. Velkovsky Phys. Rev. Lett. **81** (1998) 53.

[7] S. D. Katz Nucl. Phys. Proc. Suppl. **129** (2004) 60., hep-lat/0310051.

[8] E. V. Shuryak Phys. Lett. **B78** (1978) 150.; Sov. J. Nucl. Phys. **28** (1978) 408.

[9] K. Kajantie, J. Kapusta, L. McLerran and A. Mekjian Phys. Rev. **D34** (1986) 2746.

[10] P. V. Ruuskanen Nucl. Phys. **A544** (1992) 169c.

[11] R. D. Pisarski Phys. Lett. **B 110** (1982) 155.;

[12] A. Masera *et al.* (HELIOS-3 collaboration) Nucl. Phys. **A590** (1995) 93.

[13] D. Jouan *et al.* (NA50 collaboration) Nucl. Phys. **A638** (1998) 483c, A.de Falco *et al.* (NA50 collaboration) Nucl. Phys. **A638** (1998) 487c.

[14] G. Agakichiev *et al.* (CERES collaboration) Eur. Phys. J C4 (1998) 231.

[15] G. Agakichiev *et al.* (CERES collaboration) Phys. Rev. Lett. **75** (1995) 1272.

[16] G. Agakichiev *et al.* (CERES collaboration) Phys. Lett. **B422** (1998) 405.

[17] B. Lenkeit *et al.* (CERES collaboration) Nucl. Phys. **A661** (1999) 23c.

[18] G. Agakichiev *et al.* (CERES collaboration) J. Phys. G (in press), nucl-ex/0506002.

[19] D. Adamova *et al.* (CERES collaboration) Phys. Rev. Lett. **91** (2003) 042301, nucl-ex/0209024.

[20] V. Koch *et al.*, nucl-th/0002044.

[21] J. J. Sakurai Ann. Phys. NY (1960) 11:1-48.

[22] D. R. Yennie *et al.* Rev. Mod. Phys. (1978) 50(2).

[23] R. Rapp, G. Chanfray and J. Wambach Nucl. Phys. **A617** (1997) 472.

[24] W. Cassing, W. Ehehalt and C.M. Ko, Phys. Lett. **B363** (1995) 35.

[25] W. Cassing, W. Ehehalt and I. Králik, Phys. Lett. B377 (1996) 5.

[26] V. Koch and C. Song, Phys. Rev. **C54** (1996), 1903.

[27] R. Baier, M. Dirks and K. Redlich, GSI-Preprint-96-43.

[28] D. K. Srivastava, B. Sinha and C. Gale, Phys. Rev. **C53** (1996), R567.

[29] G. E. Brown, M. Rho Phys. Rev. Lett. **66** (1991) 2720.

[30] G. Q. Li, C.M. Ko and G.E. Brown, Phys.Rev.Lett.**75** (1995) 4007, Nucl.Phys. **A606**, (1996) 568 and G.Q. Li, C.M. Ko, G.E. Brown and H. Sorge, Nucl. Phys. **A611**, (1996) 539.

[31] E. Laermann Nucl. Phys. **A610**, (1996) 1c.

[32] G. E. Brown and M. Rho Phys. Rep. **363** (2002) 85.

[33] F. Karsch Nucl. Phys. **A590**, (1995) 367c, hep-lat/9503010

[34] J. Wambach Proc. of Quark Matter '97, Tsukuba, Japan, December 1-5, 1997, 171c.

[35] R. Rapp and J. Wambach *Eur. Phys. J* **A6** (1999) 415.

[36] A. Marin (CERES collaboration) J. Phys. G 30 (2004) S709, nucl-ex/0406007.

[37] W. Schmitz (CERES collaboration) J. Phys. G28 (2002) 1861.

[38] G. Agakichiev *et al.* (CERES collaboration) Nucl. Instr. and Meth. **A377** (1996) 362.

[39] Addendum to proposal SPSLC/P280: CERN/SPSLC 96-35/P280 Add.1.

[40] H. Appelshauser *et al.* (CERES collaboration) Proceedings Meson 98, Cracow, Poland, Acta Phys. Polonica B29 (1998) 3153.

[41] W. Chen *et al.* IEEE Trans. Nucl. Sci. **39** (1992) 619.

[42] A. Marin Proc. of Quark Matter '99, Torino, 1999 Nucl. Phys. A661 (1999) 673c.

[43] B. Yu, G.C. Smith. V. Radeka and E. Mathieson IEEE Trans. Nucl. Sci. **38** (1991) 454.

[44] W. Schmitz CERES-Note 01-98 (1998).

[45] J. Slivova. PhD thesis, Charles University in Prague, Czeck Republic, 2003.

[46] G. Agakichiev *et al.* (CERES collaboration) Nuc. Inst. and Meth. **A394** (1997) 225.

[47] P.V.C. Hough. Methods and means for recognizing complex patterns. U.S. Patent 3069654, 1962.

[48] H. Sako Development of New GENESIS, GSI, Darmstadt, Germany, 2000.

[49] T. Peitzmann *et al.* (WA98 collaboration) Proc. 29th Conference on High Energy Physics (ICHEP98), Vancouver, Canada (1998).

[50] V. Friese *et al.* Nucl. Phys. **A698** (2002) 487c.

[51] B. Alessandro *et al.* Phys. Lett. **B555** (2002) 147.

[52] P. Braun-Munzinger, I. Heppe and J. Stachel Phys. Lett. **B465** (1999) 15.

[53] S. Eidelman *et al.* Phys. Lett. **B592** (2004) 1.

[54] S. V. Afanasiev *et al.* Nucl. Phys. **A610** (1996) 188c.

[55] C. Höhne *et al.* Nucl. Phys. **A661** (1999) 485c.

[56] B. Lenkeit PhD thesis, Heidelberg University, Heidelberg, Germany, 1998.

[57] R. Scheibl and U. W. Heinz Phys. Rev. **C59** (1999) 1585, nucl-th/9809092.

[58] H. Appelshäuser *et al.* (NA49 collaboration) Nucl. Phys. **A638** (1998) 91.

[59] M. M. Aggarwal *et al.* (WA98 collaboration) Phys.Rev.Lett. **81** (1998) 4087.

[60] R. H. Dalitz Proc. Roy. Soc. **A64** (1951) 667.

[61] L. G. Landsberg Phys. Rep. 128(6) (1985) 301.

[62] R. I. Dzhelyadin *et al.* Phys. Lett. **B94** (1980) 548.

[63] G. Tel-Zur PhD thesis, Weizmann Institute, Rehovot, Israel, 1996.

[64] Z. Y. Fang *et al.* Nuovo Cimento **100A** (1998) 155.

[65] M. Benayoun *et al.* Eur. Phys. J. **C2** (1998) 269.

[66] G. Brown and M. Rho Phys. Rept. **396** (2004) 1.

[67] G. Brown and M. Rho Phys. Rept. **398** (2004) 301.

[68] K. Gallimeister *et al.* Nucl. Phys. **A688** (2001) 939.

[69] B. Kämpfer, K. Gallimeister, O.P. Pavlenko and C. Gale Nucl. Phys. **A698** (2002) 424., hep-ph/0102192.

[70] G.Q. Li, C. Gale Phys. Rev. Lett. **81** (1998) 1572.

[71] R. Rapp Nucl. Phys. **A661** (1999) 33., hep-ph/9907342.

[72] R. Rapp, J. Wambach Adv.Nucl.Phys. **25** (2000) 1., hep-ph/9909229.

[73] S. Damjanovic *et al.* (NA60 collaboration), to be published in Proceedings of Quark Matter 2005, Budapest, Hungary.

[74] G. Brown and M. Rho, nucl-th/0509001, nucl-th/0509002.

[75] A. Kozlov *et al.* Nucl. Instr. and Meth. **A523** (2004) 345.

[76] Z. Fraenkel *et al.* Nucl. Instr. and Meth. **A546** (2005) 466.